SOLIDIFICATION AND CRYSTALLIZATION BEHAVIOUR OF BULK GLASS FORMING ALLOYS

A THESIS SUBMITTED TO
THE GRADUATE SCHOOL OF NATURAL AND APPLIED SCIENCES
OF
MIDDLE EAST TECHNICAL UNIVERSITY

BY

SULTAN AYBAR

IN PARTIAL FULFILLMENT OF THE REQUIREMENTS
FOR
THE DEGREE OF MASTER OF SCIENCE
IN
METALLURGICAL AND MATERIALS ENGINEERING

SEPTEMBER 2007

Approval of the thesis:

SOLIDIFICATION AND CRYSTALLIZATION BEHAVIOUR OF BULK GLASS FORMING ALLOYS

submitted by **Sultan AYBAR** in partial fulfillment of the requirements for the degree of **Master of Science in Metallurgical and Materials Engineering Department, Middle East Technical University** by,

Prof. Dr. Canan Özgen _____
Dean, Graduate School of **Natural and Applied Sciences**

Prof. Dr. Tayfur Öztürk _____
Head of Department, **Metallurgical and Materials Engineering**

Prof. Dr. M. Vedat Akdeniz _____
Supervisor, **Metallurgical and Materials Eng. Dept., METU**

Prof. Dr. Amdulla O. Mekhrabov _____
Co-supervisor, **Metallurgical and Materials Eng. Dept., METU**

Examining Committee Members:

Prof. Dr. Tayfur Öztürk _____
Metallurgical and Materials Eng. Dept., METU

Prof. Dr. M. Vedat Akdeniz _____
Metallurgical and Materials Eng. Dept., METU

Prof. Dr. Amdulla O. Mekhrabov _____
Metallurgical and Materials Eng. Dept., METU

Prof. Dr. İshak Karakaya _____
Metallurgical and Materials Eng. Dept., METU

Asst. Prof.Dr. Kâzım TUR _____
Materials Eng. Dept., Atılım University

Date: _____

I hereby declare that all information in this document has been obtained and presented in accordance with academic rules and ethical conduct. I also declare that, as required by these rules and conduct, I have fully cited and referenced all material and results that are not original to this work.

Name, Last name: Sultan Aybar

Signature :

ABSTRACT

SOLIDIFICATION AND CRYSTALLIZATION BEHAVIOUR OF BULK GLASS FORMING ALLOYS

Aybar, Sultan

M.S., Department of Metallurgical and Materials Engineering
Supervisor: Prof. Dr. M. Vedat Akdeniz
Co-Supervisor: Prof. Dr. Amdulla O. Mekhrabov
September 2007, 121 pages

The aim of the study was to investigate the crystallization kinetics and solidification behaviour of $Fe_{60}Co_8Mo_5Zr_{10}W_2B_{15}$ bulk glass forming alloy. The solidification behaviour in near-equilibrium and non-equilibrium cooling conditions was studied. The eutectic and peritectic reactions were found to exist in the solidification sequence of the alloy. The bulk metallic glass formation was achieved by using two methods: quenching from the liquid state and quenching from the semi-state. Scanning electron microscopy, x-ray diffraction and thermal analysis techniques were utilized in the characterization of the samples produced throughout the study. The choice of the starting material and the alloy preparation method was found to be effective in the amorphous phase formation.

The critical cooling rate was calculated as 5.35 K/s by using the so-called Barandiaran and Colmenero method which was found to be comparable to the best glass former known to date.

The isothermal crystallization kinetics of the alloy was studied at temperatures chosen in the supercooled liquid region and above the first crystallization temperature. The activation energies for glass transition and crystallization events were determined by using different analytical methods such as Kissinger and Ozawa methods.

The magnetic properties of the alloy in the annealed, amorphous and as-cast states were characterized by using a vibrating sample magnetometer. The alloy was found to have soft magnetic properties in all states, however the annealed specimen was found to have less magnetic energy loss as compared to the others.

Keywords: Bulk Glass Forming Alloy, Thermal Analysis, Supercooled Liquid Region, Activation Energy, Critical Cooling Rate.

ÖZ

KALIN KESİTLİ, İRİ VE HACİMLİ METALİK CAMLARIN KATILAŞMA VE KRİSTALLEŞME DAVRANIŞLARI

Aybar, Sultan

Yüksek Lisans, Metalurji ve Malzeme Mühendisliği Bölümü
Tez Yöneticisi: Prof. Dr. M. Vedat Akdeniz
Ortak Tez Yöneticisi: Prof. Dr. Amdulla O. Mekhrabov
Eylül 2007, 121 sayfa

Bu çalışmanın amacı, iri hacimli $Fe_{60}Co_8Mo_5Zr_{10}W_2B_{15}$ alaşımının katılaşma davranışı ve kristalleşme kinetiğinin incelenmesidir. Katılaşma davranışı, dengeye yakın ve denge olmayan soğutma koşullarında çalışılmıştır. Alaşımın katılaşma sürecinde ötektik ve peritektik reaksiyonların olduğu tespit edilmiştir. İri hacimli metalik cam oluşumu iki yöntemle elde edilmiştir: alaşıma sıvı halden su verme ve yarı katı halden su verme. Taramalı elektron mikroskobu, x ışınları kırınımı ve termal analiz teknikleri, çalışma boyunca üretilen numunelerin tanımlanmasında kullanılmıştır. Hammadde türü seçiminin ve alaşım hazırlama metodunun amorf fazın görüldüğü kritik kalınlığı etkilediği ortaya çıkmıştır.

Alaşımın, Barandiaran-Colmenero metodu uygulanarak 5.35 K/s olarak tayin edilen kritik soğuma hızının bilinen en iyi cam oluşturma yeteneğine sahip alaşımınkiyle kıyaslanabilir olduğu görülmüştür.

Alaşımın izotermal kristalleşme kinetiği; fazla soğutulmuş sıvı bölgesinde ve kristalleşme sıcaklığının üstünde seçilen sıcaklıklarda çalışılmıştır. Cam dönüşümü ve kristalleşme aktivasyon enerjileri, Kissinger, Ozawa metotları gibi farklı analitik metotlar kullanılarak belirlenmiştir.

Alaşımın manyetik özellikleri, tavlanmış, amorf ve ilk döküldüğü haliyle titreşimli numune magnetometresi kullanarak tanımlanmıştır. Alaşımın bütün hallerde soft manyetik özelliklere sahip olduğu ancak tavlanan numunenin diğerlerine göre daha az manyetik enerji kaybının olduğu tespit edilmiştir.

Anahtar Kelimeler: İri Hacimli Metalik Camlar, Termal Analiz, Fazla Soğutulmuş Sıvı Bölgesi, Aktivasyon enerjisi, Kritik Soğuma Hızı.

To my beloved parents;

Elif-Celal Aybar

and brothers;

Hakan Aybar, Adnan Yazar

ACKNOWLEDGEMENTS

I express my deepest gratitude to my supervisor Prof. Dr. M. Vedat Akdeniz and co-supervisor Prof. Dr. Amdulla O. Mekhrabov for their insights, courage, and optimism. They guided me through a rich research experience. I am very grateful for their generosity that made possible for me to freely conduct my experiments. I have learned so much from them.

I am indebted my family for their understanding, love and unfettered belief in me. They always supported me by cheering me up and make me think positively. It would not have been possible without their guidance and support.

I would like to send my thanks and love to Burak Beşler for enlightening my days by being supportive, adoring and keeping me in track even in the bad days.

Since the beginning of my graduate study, I have own a lot to my dear friend Sibel Mete. I would like to express my thanks for her conversations, ideas, and encouragement. She has been an informal mentor for me.

I gratefully thank to my dear friends, Gül Fidan Sarıbay and Eda Şeyma Kepenek for their love and sacrifice for me. Their company made my life easier and colorful.

Special thanks to Cem Topbaşı for his accompany in never-ending laboratory hours, discussions, kind assistance in the experiments, stimulating critics and original ideas. I want to thank all my friends from the Novel Alloys Design and Development Laboratory; Sıla Süer, Muratahan Aykol, Mehmet Yıldırım and Nagehan Duman for

their support, friendship, and being much more than labmates. I must also thank to Başak Karagücük for her good company and motivation.

All my colleagues from the Undersecretariat of the Prime Ministry for Foreign Trade and Environmental Protection Agency for Special Areas are also gratefully acknowledged for their support.

TABLE OF CONTENTS

LIST OF TABLES

LIST OF FIGURES

CHAPTER 1

INTRODUCTION

Bulk metallic glasses have an unusual combination of physical, mechanical, magnetic, and chemical properties because of their random, non-crystalline atomic arrangements making them superior to their crystalline counterparts [1]. They are produced by using different techniques all of which involve the rapid solidification. They display high strength, low Young's modulus and excellent corrosion resistance [2].

The atoms are frozen in their liquid configuration as a result of rapid solidification [3]. Metallic glasses are non-equilibrium structures with respect to the crystalline state. For this reason, they go through structural changes from the as cast state to the metastable structurally relaxed state and finally to the crystalline state when moderately heated. Physical, chemical, and mechanical properties of the metallic glasses are significantly affected by the structural changes that occur during heating at temperature low enough to avoid crystallization [4, 5]. Therefore, the study of crystallization behaviour of metallic glasses is very important in the sense that the crystallization parameters of an amorphous phase reflect how stable it is against the thermal treatments that may present in the practical applications.

The aim of this study in general was to investigate the solidification and crystallization behaviour of $Fe_{60}Co_8Mo_5Zr_{10}W_2B_{15}$ bulk glass forming alloy system. This alloy was chosen since it was confirmed to have a high glass forming ability by the previous studies [6, 7]. The ternary Fe-Zr-B alloys were studied by Pehlivanoğlu [7] by adding minor alloying elements systematically and the Mo and W elements were found to increase the glass forming ability. The theoretical studies using the

simulation models also showed that the alloy was a good glass former. However, the crystallization kinetics of the alloy has not been studied in detail so far. Therefore, this study aims at investigating the crystallization kinetics by means of the experimental and analytical methods.

In addition, for the first time in this study, amorphous phase formation was attempted to be obtained by quenching the alloy from the semi-solid state. The existence of the semi-solid region between the eutectic and peritectic temperatures in $Fe_{60}Co_8Zr_{10}Mo_5W_2B_{15}$ was considered to be utilized for obtaining amorphous phase without complete melting of the alloy. The ability to process the bulk amorphous alloys in the semi-solid region is expected to open new perspectives to the study of bulk metallic glass formation.

The literature review on the subject and some basic concepts of the glass formation is given in Chapter Two. The analytical methods employed in the experimental studies are explained in this chapter. In the next chapter, the experimental methods used and the experiments carried out are presented. In Chapter Four, the results of the experiments are given together with the simultaneous discussion. The conclusions drawn are given in the Fifth Chapter.

CHAPTER 2

THEORY

2.1HISTORY OF METALLIC GLASSES

The first amorphous metallic alloys were claimed to have been made by Kramer [8] using vapor deposition. Then, it was proposed by Brenner et al. [9] that amorphous nickel-phosphorus alloys had been produced via electrodepositing.

Metallic amorphous alloys are comparatively new in the amorphous materials group. The first metallic glass was $Au_{75}Si_{25}$ reported by Duwez [10] at Caltech, USA, in 1960. They showed that the nucleation and growth of crystalline phase could be kinetically bypassed in some liquefied alloys to produce a frozen liquid configuration called the metallic glass. The cooling rate used to obtain this structure was on the order of 10^6 K/s which put a restriction in the specimen geometry. Only thin ribbons, foils and powders were produced with at least one dimension is small enough, on the order of microns, to allow such a high cooling rate [11].

The fundamental scientific significance and potential engineering applications of bulk metallic glasses have increased the attention to studies on their formation, structure and properties [12]. The work of Turnbull group found similarities between metallic glasses and other non-metallic glasses such as silicates, ceramic glasses and polymers. They pointed out that glass transition seen in conventional glass-forming melts could also be observed in metallic glasses produced by rapid quenching [13-15].

Turnbull predicted that a ratio, called *reduced glass transition temperature* $T_{rg}=T_g/T_m$, of the glass transition temperature T_g to the melting point or liquidus temperature T_m of alloy could be used as a criterion for determining the glass forming ability of (GFA) of an alloy [16]. Accordingly, a liquid with $T_{rg}=2/3$ becomes very sluggish in crystallization and its crystallization temperature range is very narrow. This criterion for the suppression of crystallization in undercooled melts is used as a rule of thumb for predicting the GFA of any liquid [17].

If the millimeter scale is termed as "bulk", the first bulk metallic glass was the ternary Pd-Cu-Si alloy prepared by Chen in 1974 by using simple suction casting method to form millimeter-diameter rods of Pd-Cu-Si metallic glass at a significantly lower cooling rate of 10^3 K/s [18].

In the beginning of the 1980's, the Turnbull group were able to reduce the amount of heterogeneous nucleation sites and thus able to make glassy ingots of $Pd_{40}Ni_{40}P_{20}$ with a diameter of 5 mm by subjecting the specimens to surface etching followed by a succession of heating and cooling cycles. Then in 1984, they could obtain a critical casting thickness of 1 cm by processing the Pd-Ni-P melt in a boron oxide flux [19]. The Inoue group in Japan studied on rare-earth materials with Al and ferrous metals during the late 1980s. They produced fully glassy cylindrical samples with diameters of up to 5 mm or sheets by casting $La_{55}Al_{25}Ni_{20}$ (or later $La_{55}Al_{25}Ni_{10}Cu_{10}$ up to 9 mm) into Cu moulds [20]. Mg-Cu-Y and Mg-Ni-Y alloys with the largest glass forming ability obtained in $Mg_{65}Cu_{25}Y_{10}$ were developed by the same group in 1991 [21].

The Inoue group also produced a family of Zr-based Zr-Al-Ni-Cu alloys having a high glass forming ability and thermal stability [22]. The critical casting thickness up to 15 mm was obtained in these alloys and the supercooled liquid region was extended to 127 K for the alloy $Zr_{65}Al_{7.5}Ni_{10}Cu_{17.5}$. The production of these alloys showed that the bulk metallic glass compositions were not a laboratory curiosity and could be studied for engineering applications [23].

After the significant effects of Inoue's works were realized, Johnson and others from Caltech started to work on bulk metallic glass compositions in the early 1990s. In 1993, $Zr_{41.2}Ti_{13.8}Cu_{12.5}Ni_{10}Be_{22.5}$ [=$(Zr_3Ti)_{55}(Be_9Cu_5Ni_4)_{45}$], commonly referred to as Vitreloy 1 (Vit1), with a critical thickness of several centimetres was produced by Peker and Johnson [24]. This and the Inoue's work [25] can be considered as the starting point for the use of bulk glassy materials in structural applications. The Vit1 alloy has been investigated extensively in the next ten years [23]. The Inoue group in 1997 restudied $Pd_{40}Ni_{40}P_{20}$ alloy and replaced 30% Ni by Cu to produce an alloy with a critical casting thickness of 72 mm [25]. Figure 2.1 shows the critical casting thickness for glass formation versus the year of discovery of the corresponding alloy.

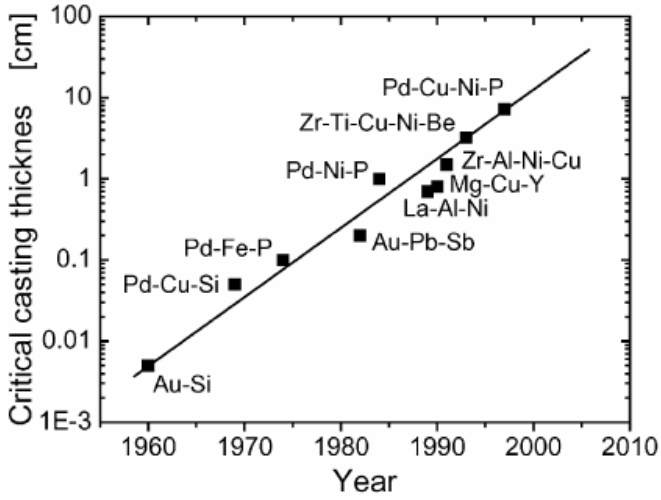

Figure 2.1 The critical casting thickness for the glass formation as a function of the year the corresponding alloy has been discovered [23].

The critical casting thickness increased by more than three orders of magnitude in the last 40 years [23]. The future applications of the bulk metallic glasses can be

predicted using this increasing trend. The bulk glass forming alloy systems which are produced until year 2002 are given in Table 2.1 which classifies the alloy systems as non-ferrous and ferrous [25] .

Recently, the researches on the bulk metallic glasses are growing significantly. Many researchers are studying on the new alloy compositions and investigating the mechanical, structural, thermophysical, and magnetic properties of these alloys. Based on the recent developments, new applications of the bulk metallic glasses can be expected in the near future [3].

Table 2.1 The bulk glass forming alloy systems produced between the years 1988-2002 (reproduced after Ref. [25]).

	Alloy System	Year
Non-ferrous alloy systems	Mg-Ln-M (Ln: lanthanide metal: M:Ni, Cu, Zn)	1988
	Ln-Al-TM (TM: transition metal:Fe, Co, Ni, Cu)	1989
	Ln-Ga-TM	1989
	Zr-Al-TM	1990
	Ti-Zr-TM	1993
	Zr-Ti-TM-Be	1993
	Zr-(Ti, Nb, Pd)-Al-TM	1995
	Pd-Cu-Ni-P	1996
	Pd-Ni-Fe-P	1996
	Pd-Cu-B-Si	1997
	Ti-Ni-Cu-Sn	1998
	Cu-(Zr,Hf)-Ti	2001
	Cu-(Zr,Hf)-Ti-(Y,Be)	2001
	Cu-(Zr, Hf)-Ti-(Fe, Co, Ni)	2002
Ferrous alloy systems	Fe-(Al, Ga)-(P, C, B, Si, Ge)	1995
	Fe-(Nb, Mo)-(Al, Ga)-(P, B, Si)	1995
	Co–(Al, Ga)–(P, B, Si)	1996
	Fe–(Zr, Hf, Nb)–B	1996
	Co–(Zr, Hf, Nb)–B	1996
	Ni–(Zr, Hf, Nb)–B	1996
	Fe–Co–Ln–B	1998
	Fe–Ga–(Cr, Mo)–(P, C, B)	1998
	Fe–(Nb, Cr, Mo)–(C, B)	1999
	Ni–(Nb, Cr, Mo)–(P, B)	1999
	Co–Ta–B	1999
	Fe–Ga–(P, B)	2000
	Ni–Zr–Ti–Sn–Si	2001
	Ni–(Nb, Ta)–Zr–Ti	2002
	Fe–Si–B–Nb	2002
	Co–Fe–Si–B–Nb	2002
	Ni–Si–B–Ta	2002

2.2 BASIC CONCEPTS OF METALLIC GLASSES

2.2.1 Conventional Glasses and Glass Transition

A glass is formed when a liquid is continuously cooled while detectable crystallization is avoided. A typical time temperature transformation diagram (TTT) for crystal growth in an undercooled melt is given in Figure 2.2 which displays the time taken for a small amount of crystallinity to form in the undercooled melt as a function of temperature.

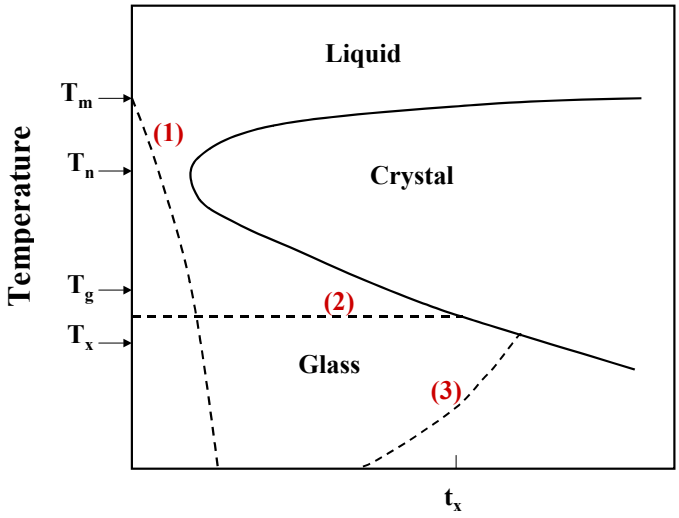

Figure 2.2 Schematic TTT diagram for crystal growth in an undercooled melt, showing (1) rapid cooling to form a glass, (2) isothermal heat treatment of the glass leading to crystallization at time t_x, (3) slow heating of the glass giving crystallization at T_x [reproduced after Ref. [3]).

There is only a short range order, i.e. a few molecular dimensions seen in molecular structure of glasses. They lack long range order at any molecular distances [4]. Glassy or non-crystalline materials differ from their crystalline counterparts in the way they solidify as shown in Figure 2.3. There is no definite temperature for glassy

materials at which the liquid transforms into a solid, instead their viscosity becomes greater as the temperature decreases in a continuous manner. The transition from a liquid to glassy state is termed as *glass transition* which is characteristic of all glass formers such as molecular liquids, organic polymers, molten salts, and metallic alloys [27]. The temperature at which this slope change occurs is called *the glass transition temperature.* Glass transition starts at a temperature and ends when the structure is changed completely to glass. Glass state is practically identified when the structure lacks long range order at a 1-2 nm distance. Figure 2.3 shows how properties such as, volume, enthalpy, and entropy, of crystalline and non-crystalline materials change with temperature revealing some facts about the transitions form liquid to solid state. When a non-crystalline material is continuously cooled from liquid state, its properties go through a continuous decrease but the slope of this change is not constant throughout the cooling process.

The fact that the atomic motion almost stops at the glass transition-except for thermal vibrations explains some observations. The atomic structure, for example, is observed not to change at T_g and volume, enthalpy, and entropy are continuous across the glass transition. Furthermore, expansion coefficient of the glass and specific heat are lower than those of liquid since molecular rearrangements and motions cease to contribute to these quantities below T_g [28].

The glass transition in metallic glasses has been studied since their first discovery. Louzguine-Luzgin and Inoue [29] studied the glass transition of metallic glasses on cooling and heating in correlation with the devitrification behaviour. They gave the variation of enthalpy with temperature by a scheme shown in Fig. 2.4 (a). The glass transition on cooling occurs in the temperature range between the conditional beginning of glass transition (T_{bg}^{C}) and the finish of glass transition (T_{fg}^{C}) temperatures which can be called as a glass transition region.

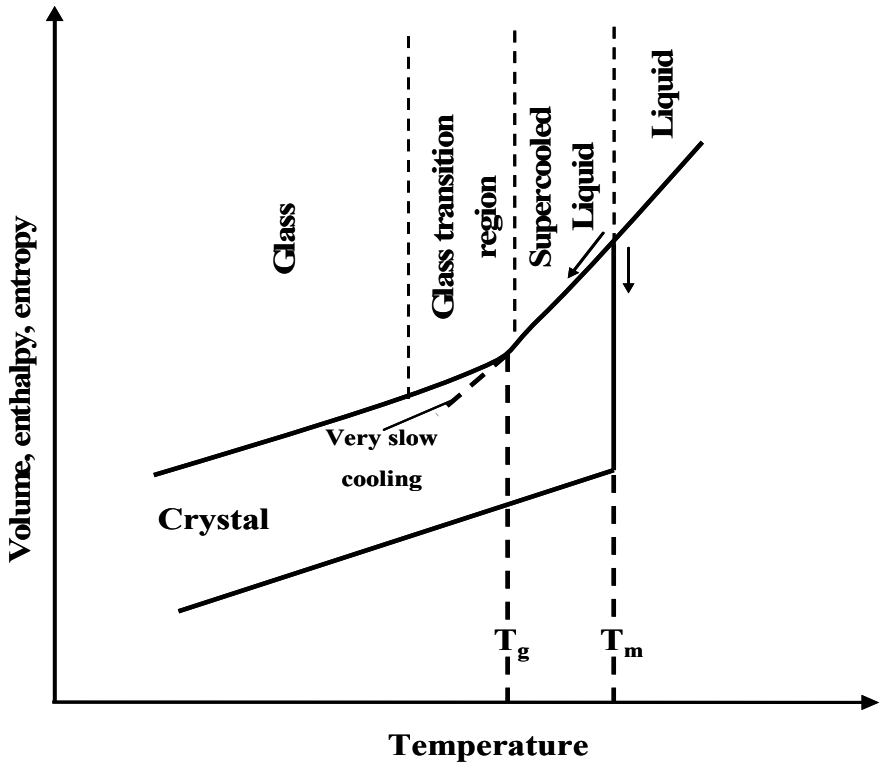

Figure 2.3 Variation of properties of crystalline and non-crystalline materials with temperature (reproduced after Ref. [27]).

The intersection of the two slopes gives an intermediate temperature which in turn is called the glass transition temperature T_g^C at a certain cooling rate. They showed in Fig. 2.4 (b) that glass transition on heating (shown by a symbol H) on the other hand occurs in the temperature interval in between temperatures of the conditional beginning of glass to supercooled liquid transition (T_{bg}^H), which is often treated as the glass-transition temperature in literature,. and of the finish of glass transition (T_{fg}^H). They observed that the supercooled liquid state existed between T_{fg}^H and devitrification or crystallization temperature known as T_x.

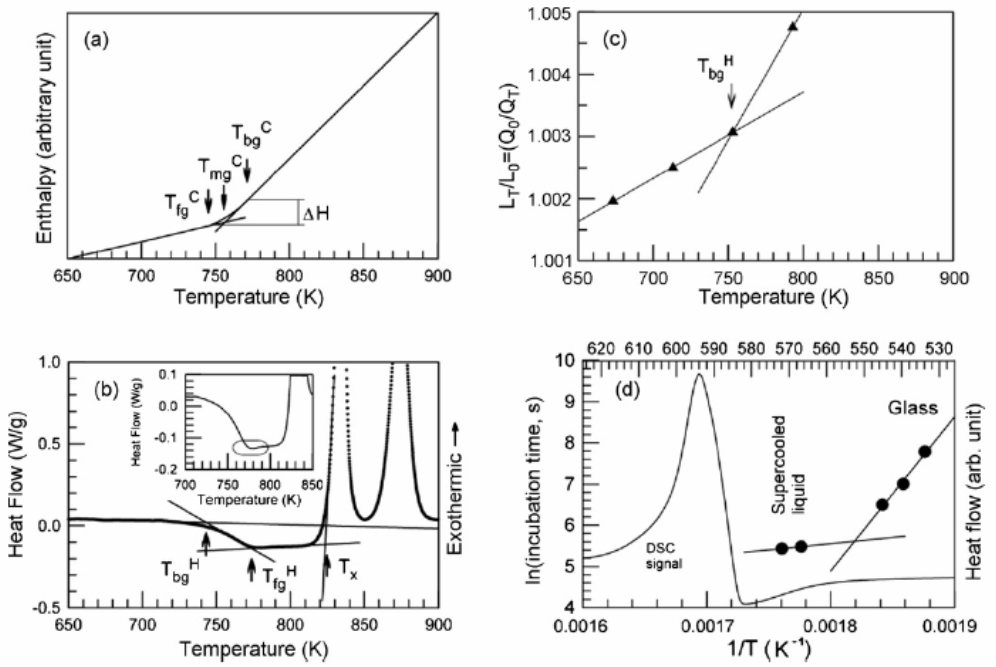

Figure 2.4 (a) Specific heat as a function of temperature, (b) DSC curve for $Cu_{55}Hf_{25}Ti_{15}Pd_5$ alloy, (c) the ration of X-ray diffraction peak positions Q_0/Q_T related to L_T/L_0 vs. temperature, and (d) DSC curve and Arrhenius plot created using incubation time for phase transformation in $Al_{85}Ni_5Y_4Nd_4Co_2$ alloy. (After Ref. [29])

They also discussed the possible origins of glass transition phenomenon with respect to the atomic structure of an alloy in the glass transition region which is schematically shown in Fig. 2.5 [30]. The transformed glassy areas with higher packing density marked with dashed lines in Fig. 2.5(a) showing that the atomic movements are smaller than the average interatomic distance. This leads to the diffusionless formation of the glassy structure with a higher density as shown in Fig. 2.5 (b) and (c) [27].

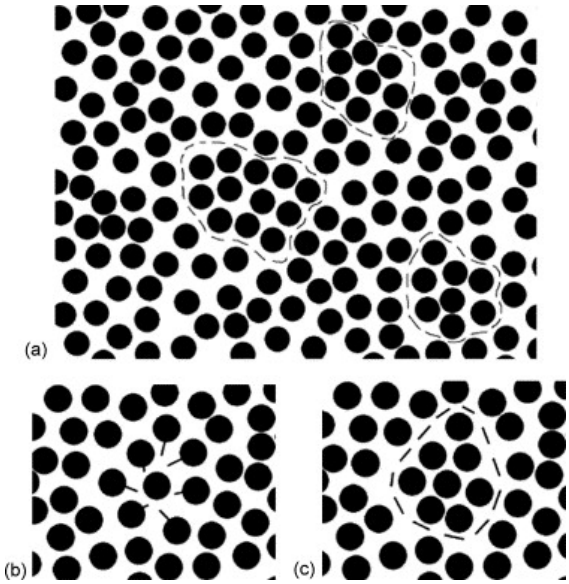

Figure 2.5 (a) Schematic representation of the atomic location in a liquid within the glass transition region, the glassy areas shown with dashed lines, (b) and (c) indications of a process of solidification [30].

The metallic glasses can achieve a liquidus temperature on heating at higher heating rates without crystallization [31], while at slower heating not a diffusionless but a diffusive transformation takes place [32].

2.2.2 Glass Formation

Glass formation in bulk metallic glasses is the consequential process of avoiding the possible crystallization when the liquid alloy is cooled below its melting temperature. It can be interpreted by considering thermodynamic, kinetic, and microstructural aspects.

2.2.2.1 Thermodynamics of glass formation

The driving force for glass formation is the difference in the Gibbs free energy of supercooled liquid and the solid phases which may be shown as $\Delta G_{l\text{-}s}$ and calculated using the following equation:

$$\Delta G_{l-s}(T) = \Delta H_f - \Delta S_f T_0 - \int_T^{T_0} \Delta C_p^{l-s}(T)dT + \int_T^{T_0} \frac{\Delta C_p^{l-s}(T)}{T} dT \qquad (2.1)$$

where ΔH_f and ΔS_f are the enthalpy and entropy of fusion, respectively at the temperature T_0, the temperature at which the solid and liquid phases are in equilibrium and $\Delta C_p^{l\text{-}s}$ is the specific heat capacity difference between the respective phases [34]. To obtain lower $\Delta G_{l\text{-}s}$, ΔH_f must be small and ΔS_f must be large. Since ΔS_f is proportional to the number of microscopic states [35], large values are expected for the multicomponent alloys which in turn lead to a larger driving force for glass formation. Also, when ΔH_f is low and the reduced glass transition temperature is high, the chemical potential is low leading to a low $\Delta G_{l\text{-}s}$ [36].

Fecht et al. [37] studied the thermodynamic functions of bulk metallic glasses. They stated that the difference in specific heat, $\Delta C_p^{l\text{-}s}(T)$, between the undercooled liquid and the corresponding crystalline phase can be used in studying the crystallization processes and glass formation. They presented the specific heat difference as a function of undercooling for several metallic elements and bulk glass forming alloys indicating that $\Delta C_p^{l\text{-}s}$ of bulk metallic glass forming alloys increases much more than that of the pure metals. Another thermodynamic function, the entropy difference ΔS between the liquid and crystal, was also computed from the specific heat data. Figure 2.6 shows the entropy difference for a typical metallic element (Indium) and the Pd-and Zr-based BMG forming alloys [37].

According to Kauzmann [38], the supercooled liquid has significantly larger entropy than the crystal just below the melting temperature. The liquid entropy continues to decrease until a certain temperature, called the Kauzmann temperature, T_K, is reached. Below this temperature, the liquid entropy becomes lower than the crystal entropy if the extrapolation is performed on the curves**.**

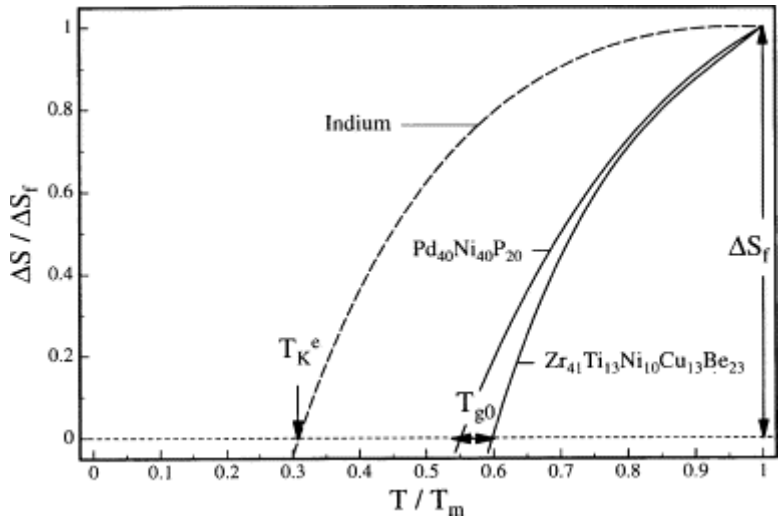

Figure 2.6 The entropy difference between the crystal and liquid states for pure metals and bulk metallic glass forming alloys after Ref. [37].

The entropy values presented in Fig. 2.6 are extrapolated below the experimentally identified range of 0.6-1.0 of T/T_m The temperatures at about $0.6T_m$ and 0.3 T_m are found as isentropic temperatures for the bulk metallic glass forming alloys (T_{g0}) and for the metallic element (T_K^e) respectively [37].

2.2.2.2 Kinetics of glass formation

The positive free energy arises from the interface between the undercooled liquid and the crystal creates a barrier for the nucleation process. The atoms in the liquid phase need to rearrange themselves to overcome this barrier. Once it is overcome, nucleation takes place and the rate of nucleation is calculated by taking the product of a kinetic term and a thermodynamic term given as [34]:

$$I = \frac{A_v}{\eta_T} \exp\left(-\frac{\Delta G^*}{kT}\right) \tag{2.2}$$

where A_v (Pa s/m^{3}s) is a constant parameter on the order of 10^{32} and k_B is the Boltzmann constant. ΔG^*, which constitutes the thermodynamic term of Equation (2.2), is defined as the nucleation barrier to form a spherical nucleus and is expressed as:

$$\Delta G^* = \frac{(16/3)\pi \sigma^3}{\left[\Delta G_{l-s}(T)\right]^2} \tag{2.3}$$

where $\Delta G_{l\text{-}s}$ is the difference in Gibbs free energy difference per unit volume, and σ is the interfacial energy between the liquid and the crystal nuclei. The kinetic term appearing in Equation (2.2) is the viscosity, η, which is related to diffusivity by the well-known Stokes-Einstein relation $D=k_BT/3\pi\eta l$, where l is the average atomic diameter. A relation known as the Vogel-Fulcher-Tamman (VFT) [39],

$$\eta(T) = \eta_0 \exp\left(\frac{D T_0}{T - T_0}\right) \tag{2.4}$$

describes the viscosity of liquids. T_0 in above equation is the Vogel-Fulcher temperature defined as the temperature at which the barriers against flow would

approach to infinity. *D* in Equation (2.4) is named as *fragility parameter* which is a fluid property describing the degree of deviation of that fluid from an Arrhenius behaviour and takes values between 1 and 100 [40]. The liquids with a fragility parameter smaller than 10 are classified as "fragile" According to the available viscosity data, BMG forming liquids are categorized as "strong" glasses since their fragility parameters are approximately 20. A comparison between the viscosities of some typical BMGs and a selection of typical non-metallic liquids is given in Figure 2.7 [34].

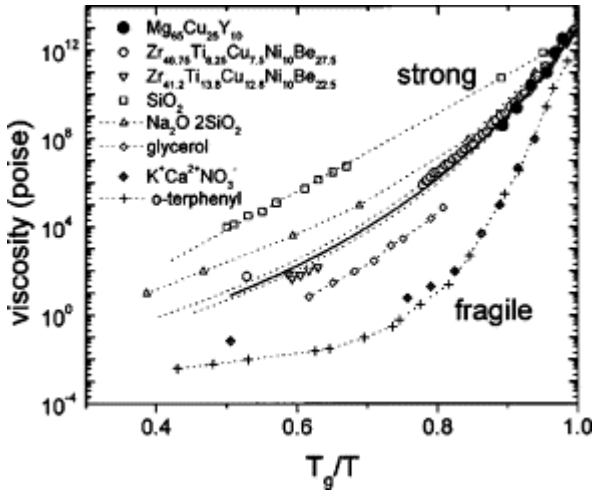

Figure 2.7 A comparison of viscosity of various glass-forming liquids. The plot shows that the BMG forming liquid can be classified as strong liquid [34].

2.3 GLASS-FORMING ABILITY CRITERIA FOR BULK METALLIC GLASSES

It is known that the any material can be formed into glass if cooled form the molten state to the glass transition temperature, T_g, at a rate fast enough to prevent crystallization. *Glass-forming ability (GFA)* is the property which describes the easiness of vitrification on cooling down to T_g. A maximum allowed fraction of

crystalline phase, x_c, generally taken between 0.1 % and 0.0001% is conventionally assumed to categorize a material as glassy [41]. Therefore, critical cooling rate (CCR), which is defined as the minimum cooling rate to avoid crystallization, can be used to evaluate the GFA of alloys. Lower the critical cooling rate of a material better its glass forming ability. But it is a long process to measure the CCR experimentally therefore some other parameters were developed in order to describe the GFA of a certain system.

It is crucial to have a better understanding of glass forming ability and how it is expressed in terms of the properties of the material in order to design new alloys which can be produced by applying lower cooling rates close enough to that of natural glass forming systems. Since the first discovery of bulk metallic glasses there are plenty of studies on the development of a universal criterion in assessing the glass forming ability. However, these studies still remain at the empirical level such as the work of Inoue [25] resulting in three empirical rules for obtaining glass formation in metallic alloy systems, i.e., (1) being multicomponent consisting of more than three elements; (2) having a significant atomic size mismatches above 12% among the main three constituent elements, and (3) having a suitable negative heats of mixing among the main elements.

In order to make the following discussion more clear, some basic questions may be asked: Why some systems can be vitrified more easily than the others? What are the factors deciding the composition range over which glasses can be made? There are several approaches has been developed in literature to answer these questions and consequently a number of glass forming criteria has been utilized. Before beginning to discuss these criteria further, it is important to mention that most of the criteria were originated from one single alloy system reported by a single research group by using limited experimental data [42] and are open to misleading results when applying to other systems.

2.3.1 Topological Criterion

The empirical Hume-Rothery rules summarize the importance of the atomic size factor and the critical concentration of a solute in phase transformations. Egami [43] et al. identified the origins of these rules which in turn lead to the establishment of topological criterion for metallic glass formation [43-45]. These criteria emphasize that amorphous structure starts to develop when local atomic strains generated by size differences between solute and solvent elements reach a critical level resulting in a topological instability of the crystalline lattice by changing local atomic coordination number. Egami [43] et al. relates the minimum solute concentration required for glass formation and the amount of the atomic size mismatch in binary alloys by the following equation:

$$C_{\min} = \frac{0.1}{\left|\left(R_B / R_A\right)^3 - 1\right|} \qquad (2.5)$$

where R_A and R_B are radii of the solvent atom A and solute atom B respectively. According to above equation, critical solute concentration for glass formation decreases as the ratio of the atomic sizes of the solute and solvent atoms increase. A method relating the two important topological parameters; atomic size of the constituent elements and the relative numbers of atoms was proposed by Senkov et al. [46] in which each element is represented by a data point on the plot of atomic size versus elemental concentration. All the data points from all of the elements in a particular alloy constitute a single curve called the atomic size distribution plot (ASDP). ASDPs of ordinary amorphous alloys with a CCR greater than 10^3 K/s and bulk amorphous alloys with a CCR less than 10^3 K/s have different shapes. Senkov et al. [47] further stated that the critical concentration of a solute element required for amorphization decreases, reaches a minimum, and then increases as the solute atom becomes increasingly small relative to the solvent atom.

2.3.2 Parameters Involving Characteristic Temperatures

There are many studies devoted to evaluate the GFA of bulk glass forming alloy systems in terms of the characteristic temperatures. The most of the characteristic temperatures are usually obtained using differential scanning calorimetry (DSC) or differential thermal analysis (DTA). A typical DSC curve for an amorphous alloy is presented in Figure 2.8 [48]. A decrease in heat flow (ΔH_{max}) occurs when the supercooled liquid transforms into glass at T_g, but it is also distinguishable that this is not an abrupt decrease occurring exactly at T_g rather it takes place gradually around T_g [48].

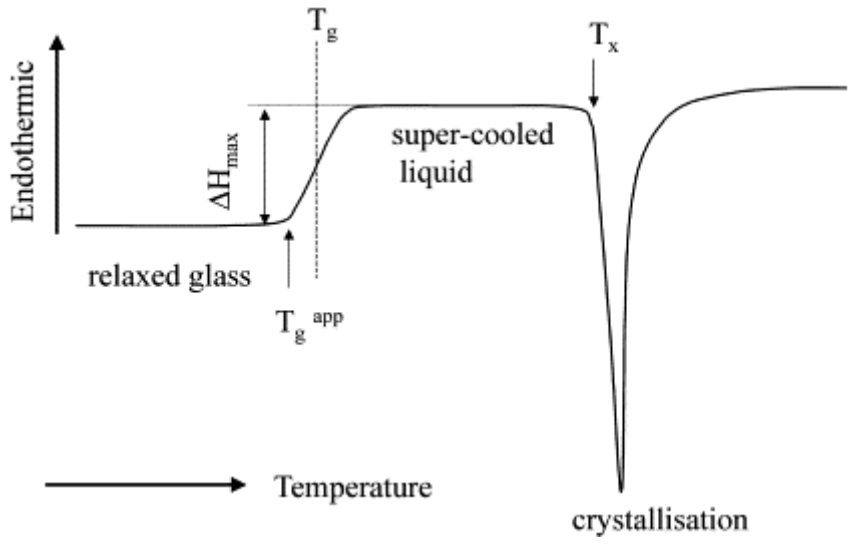

Figure 2.8 A typical DSC curve for an amorphous alloy on heating [48].

Here, T_g can be taken as intersection of two linear portions joining the transition elbow at glass transition and T_x as the onset crystallization temperature. Turnbull et al. [16, 30] suggested a criterion using the two characteristic temperatures T_g, and the melting temperature T_m or the liquidus temperature T_l. As mentioned earlier this criterion is called *the reduced glass transition temperature, T_{rg}*, which is expressed

as the ratio of T_g to T_m or T_l ($T_{rg}=T_g/T_m$ or T_g/T_l). Later, the extent of supercooled liquid region ΔT_x ($\Delta T_x=T_x-T_g$) defined as the region between the glass transition and the crystallization temperatures have been started to be used as the GFA criterion for bulk metallic glasses [49].

According the nucleation theory [16], a liquid with a high viscosity between T_g and T_m typically has a high GFA with a low R_c. The viscosity of liquid is known to be constant ($=10^{12}$ Pa.s) at T_g, thus a high value of the reduced glass-transition temperature would lead to higher viscosity in the supercooled state, giving rise to a low R_c [50]. As also indicated in the Section 2.2, Turnbull [30], based on nucleation theory, showed that alloys having a T_{rg} larger than 2/3 can be good glass formers since the suppression of crystal nucleation due to the sluggishness of the crystallization kinetics renders the glass formation.

The supercooled liquid region, ΔT_x, is regarded as a measure of GFA since it represents how stable is a liquid against crystallization upon heating above T_g. It has been accepted that the bulk metallic glasses with high GFA have $\Delta T_x \geq 50$ K.

Donald and Davies [51], on the other hand, suggested that the GFA of alloys could be related to the simple parameter:

$$\Delta T^* = \frac{T_m^{mix} - T_m}{T_m^{mix}} \tag{2.6}$$

which represents the fractional departure of T_m from the simple rule of mixtures melting temperature T_m^{mix}, where

$$T_m^{mix} = \sum_i^n n_i T_m^i \tag{2.7}$$

and n_i and T_m^i are the mole fraction and melting point respectively, of the *i*th component of an alloy with *n* component. They found that the most of glass forming alloys such as iron and nickel based multicomponent alloys had values of $\Delta T^* \geq 0.2$.

Another parameter, involving the characteristic temperatures, is the K_{gl} parameter proposed by Hruby [52] defined by:

$$K_{gl} = \frac{T_x - T_g}{T_m - T_x} \qquad (2.8).$$

This criterion expresses the thermal stability of a glass on subsequent reheating as directly proportional to the ease of its formation.

The stability parameter *S* developed by Saad and Poulain [53] expressed by

$$S = \frac{(T_p - T_x)(T_x - T_g)}{T_g} \qquad (2.9)$$

where T_p is the crystallization peak temperature. It describes the effect of temperature difference between crystallization peak temperature and the onset crystallization temperature together with the position of glass transition and crystallization exotherm.

Although the GFA criteria based on the characteristic temperatures have been widely used in studies aiming to design new BMGs, there are many cases in which they had failed to predict GFA. Therefore, efforts to avoid the limitations of existing criteria have been made.

2.3.2.1 ϕ criterion

Fan et al. [50] developed a new glass forming ability criteria using the fragility concept and the nucleation theory. They stated that the overestimation of GFA due to the usage of T_{rg} parameter could be corrected by introducing ΔT_x $(=T_x-T_g)$, in a new dimensionless ϕ criterion, expressed by

$$\phi = T_{rg}\left(\frac{\Delta T_x}{T_g}\right)^a \tag{2.10}$$

where ΔT_x is normalized by T_g, and a is a constant. They made the validation of the ϕ criterion in evaluating the real glass-forming systems including oxide, fluoride, semi-conductor, metallic and molecular glasses by plotting the relationship between R_c and ϕ separately for each of them. They stated that compared with the T_{rg} criterion, the proposed correlation between ϕ showed a good correlation with R_c.

2.3.2.2 γ criterion

γ criterion was developed based on the crystallization point of view during both reheating and cooling of the undercooled liquid. Lu et al. [54] considered that the GFA of metallic glasses was associated with two factors, T_x/T_g and T_x/T_l. They used the average of these two factors [(1/2) $((T_g+T_l)/T_x)$] to normalize T_x and this normalized T_x, denoted as γ, is expressed as:

$$\gamma = \frac{T_x}{T_g + T_l} \tag{2.11}$$

and they validated this new parameter by analyzing readily available experimental data in literature. Liu et al. [55] studied the relation between the γ values and the critical cooling rate for glass formation for some typical metallic glasses as shown in Figure 2.9.

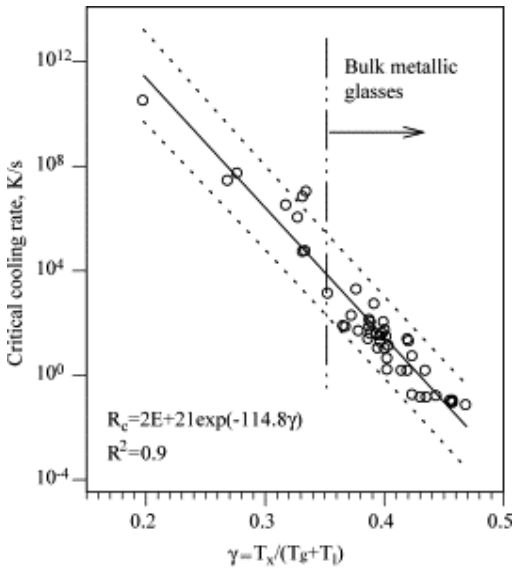

Figure 2.9 Correlation between the critical cooling rate and the γ parameter for typical metallic glasses [55].

A linear interrelationship expressed by

$$R_c = R_0 \exp[(-\ln R_0 / \gamma_0)\gamma \qquad (2.12)$$

was found as demonstrated as a solid line in Figure 2.9. R_0 and γ_0 in Equation (2.12) are constants, R_c in K/s and γ is dimensionless. They further pointed out that metallic glass with the least dimension of 1 mm, the alloy should have a γ value of 0.362 or higher [55].

Lu et al. [55] also demonstrated that γ parameter correlated better with R_c and Z_{max} than T_{rg} and ΔT_x alone could not be effectively used to evaluate the relative GFA of metallic glasses.

2.3.2.3 δ criterion

Chen et al. [56] proposed another criterion by using classical theory of nucleation and growth and the perspective of phase transformation kinetics. The nucleation and growth rates of a crystalline phase at a given temperature are inversely proportional to the three parameters: viscosity (η), the change in entropy per mole of alloy due to melting, ΔS_f, and $T/(T_l-T)$ where T is the temperature of the melt. Considering that the GFA of an alloy is inversely proportional to the nucleation and growth rate of the crystalline phases, which form during cooling, GFA of the alloys can be found to be proportional to above three parameters. Chen et al. [56] assumed ΔS_f to be constant for simplicity based on the fact that the ΔS_f of alloys consisting of mainly metallic elements does not change much from one alloy to another. Evaluating the effects of two other parameters and considering the glass formation takes place at T_g, they determined that GFA was proportional to T_g/T_l-T_g. The effect of viscosity of the supercooled liquid was found to be related with the magnitude of (T_x-T_g). To apply the (T_x-T_g) to a wide range of BMG alloys with different glass transition temperatures and viscosities, they proposed to normalize this parameter with respect to T_g, resulting in (T_x-T_g)/T_g= T_x/T_g-1. Then the GFA was considered to be proportional to T_x/T_g. These two relations were then combined and a new dimensionless criterion, named δ, was defined by:

$$\delta = \frac{T_x}{T_l - T_g} \tag{2.13}$$

Using the available experimental data of the characteristic temperatures of many BMGs, a comparison between the T_{rg}, γ, and δ parameters was performed based on the statistical analysis. Having the highest linear correlation coefficient corresponding to Z_{max} versus GFA criteria, δ was found to have the strongest ability to reflect the GFA.

2.3.2.4 *α and β* criteria

Mondal et al. [57] developed two criteria, namely α and β, to asses the GFA of BMGs. According to the fact that the low T_l could be an indicator of the high stability of the liquid and that high T_x was of a high thermal stability, they combined these two effects into one parameter, called α expressed as:

$$\alpha = \frac{\Delta T_x}{T_l} + \frac{T_g}{T_l} = \frac{T_x}{T_l} \qquad (2.14)$$

This parameter does not include T_g, which is not usually available for a number of binary glassy alloys and for the amorphous phases obtained by vapour condensation or solid-state amorphization [57].

β-parameter, on the other hand, was developed by combining two basic factors related to glass formation, namely glass forming tendency during cooling of the melt expressed by T_g/T_l, and the thermal stability of glass expressed by T_x/T_g. Then the β-parameter was defined by:

$$\beta = \left(\frac{T_x}{T_g} + \frac{T_g}{T_l} \right) \qquad (2.14)$$

When T_g was approximated by T_x for the glasses which do not exhibit T_g on heating, they obtained β-parameter as:

$$\beta = 1 + \frac{T_x}{T_l} \tag{2.15}$$

Mondal et al. [57] further compared the efficiencies of α and β with T_{rg}, γ, and ΔT_x by plotting them against the R_c and Z_c (critical section thickness) for a number of metallic glasses found in the literature. They observed a linear relation with all GFA parameters and gave the relation between R_c and Z_c:

In this study, also from the regression analysis of the plots between various GFA criteria and R_c and Z_c, the statistical correlation factor, R^2, was evaluated which indicated the effectiveness of various GFA parameters with higher the R^2 value, the better is the correlation. It is stated that the newly proposed β parameter gave the highest R^2 value of 0.93 among all the GFA criteria and α parameter gave 0.90 close to the correlation coefficient of γ, which was 0.91 [54].

2.3.3 The Use of Phase Diagrams in Evaluating the GFA

When designing new bulk metallic glasses, it is a usual practice to use the binary and ternary phase diagrams of the constituent elements to comment on whether the system will be a good glass former. It has been shown that the systems having eutectic reaction exhibit high glass-forming ability [30, 58, 59]. When picking up the elements in constituting the alloy systems, the ones forming stable eutectics are usually chosen at start. Once the main elements are chosen, the next step may be adding more elements to the system. Even the GFA of systems having deep eutectics can reduce when some elements are added which make compounds stable at very high temperatures. Instead, elements capable of making more than one eutectic reaction with the as present elements should be chosen.

Ma et al. [59] in a recent study showed that the bulk metallic glass-forming compositions coincide with the eutectic compositions taking Zr-Ti-Cu-Ni as a model system. They concluded that the thermodynamically calculated phase diagrams provide a powerful tool to predict eutectic compositions in multicomponent systems which are potentially bulk metallic glass-formers.

The main disadvantage in using phase diagrams when developing bulk glass forming alloys is that they are equilibrium phase diagrams and do not give information about the metastable phases which may form during rapid solidification. Especially, when the number of components gets larger, the situation becomes more complex involving many binary, ternary, even quaternary phases. There exists no such diagrams showing all the interactions among all the constituent elements in multi-component systems and this makes the studies based on the phase diagrams is somewhat hypothetical.

2.3.4 Bulk Glass Forming Ability

Recently, Akdeniz et al. [6] studied the phase transformations taking place during rapid and equilibrium solidifications of $Fe_{60}Co_8Zr_{10}Mo_5W_2B_{15}$ and $Zr_{65}Al_{10}Ni_{10}Cu_{15}$ alloys by establishing a relationship between bulk glass forming ability and type/nature of invariant reactions. They identified that the solidifications of these alloy systems occurs through two consecutive invariant reactions; a high temperature peritectic followed by a eutectic reaction and presented a phase diagram of hypothetical binary alloy system going through same kind of reactions. A solidification behaviour involving a sequence of peritectic and eutectic reactions as well as high magnitude of the ratio of the reaction enthalpies of these reactions were considered to be strong indicators of high bulk glass forming ability.

2.3.5 Theoretical Studies Concerning GFA

The development of theoretical models for simulation of the glass forming ability of bulk amorphous alloys is very useful in the studies on finding the alloy with the enhanced glass forming ability. The theoretical modelling based on the electronic theory of alloys in pseudo-potential approximation and statistical thermodynamics gives the alloy systems which are candidates for the best glass formers.

2.4 PRODUCTION METHODS OF BULK METALLIC GLASSES

Bulk metallic glasses require rapid solidification techniques to attain high cooling rates and to suppress the crystallization reaction. There are two kinds of processing techniques used for producing bulk metallic glasses: solidification and consolidation. Water-quenching, copper mold casting, high-pressure die casting, arc melting, unidirectional melting, suction casting and squeeze casting can be listed as a solidification technique whereas hot pressing and warm extrusion of atomized amorphous powders in the supercooled liquid region are the consolidation processes [59].

The oldest of all the techniques used to produce bulk metallic glasses is the *water quenching method* in which the alloy is melted in a vacuum-sealed quartz tube and then is water quenched. Cooling rates in the range 10-100 K/s are achieved by using this method [61]. Inoue et al. [62] produced $Zr_{65}Al_{7.5}Ni_{10}Cu_{17.5}$ bulk amorphous alloy in rod shape using water quenching technique.

In the most commercially available BMG products, *high-pressure die casting* is used [12]. Bulk amorphous alloys with a thickness up to 10 mm in cylindrical and sheet shapes were produced in Mg-Ln-TM [63] and Ln-Al-TM [64] ternary alloy systems by using high-pressure die-casting method.

Another frequently used method to synthesize BMGs is the copper mould casting method. The apparatus used consists of an injection system and a copper mould which can have in different shaped cavities such as wedge-shaped or ring shaped. The injection of highly viscous molten alloy into these small cavities requires high ejection temperatures and pressures. Ikarashi et al. [65] used ring-shaped copper molds to produce Fe–Al–Ga–P–C–B–Si glassy alloy in a ringed form with the outer diameter of 10 mm, the inner diameter of 6mm and the thickness of 1mm with a copper mould casting set-up as shown in Figure 2.10 (a). Majumdar et al. [66] investigated the bulk glass formation in multicomponent Fe-Co-Ni-Zr-B and Fe-Co-Ni-Zr-Nb-B alloy systems by means of casting in a wedge shaped copper mould as shown in Figure 2.10 (b). Their experimental observations showed that the minimum thickness of the casting is proportional to the slit width of the quartz tube containing the molten alloy and inversely proportional to the ejection pressure. Using wedge-shaped copper moulds has the advantage of attaining different cooling rates at different regions along the wedge hence gives the opportunity to observe different fractions of amorphous phase in one experiment.

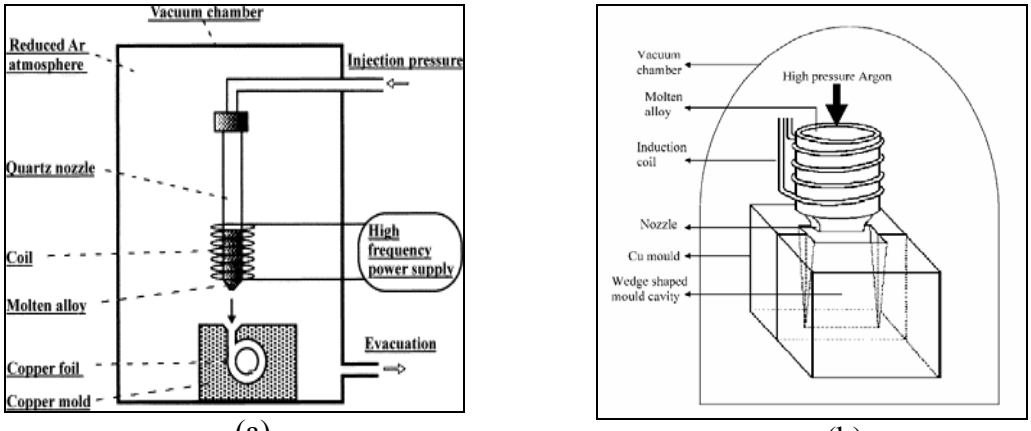

Figure 2.10 Schematic illustration of a copper mould casting equipment, (a) in a ring shape form [65], (b) in a wedge shape form [66].

Arc melting process involves the melting of the elements constituting the alloy in a water-cooled copper crucible. The necessary heat used for melting is provided by a high energy arc which can rise the temperature of the constituents up to approximately 2000 ˚C. The melting event takes place in a high vacuum argon atmosphere. However, in this method it is difficult to completely suppress the precipitation of crystalline phase due to ease of the heterogeneous nucleation by incomplete melting at the bottom side contacted with the water-cooled copper hearth [36].

Another commonly used process used in the production of BMGs is known as melt spinning, which involves the formation of a free jet of molten liquid and direction of this liquid at a rapidly moving substrate. The final product is usually in the form of a ribbon [67]. Melt spinning can be carried out in two ways: (1) by extruding a liquid stream into a cooling medium (free jet melt spinning) or (2) by allowing a liquid jet to impinge on a chill-block and to be formed into a tape (chill-block melt spinning) [11].

In suction casting method, however, amorphous samples are prepared by ejecting the molten alloy into a copper mould by means of a suction force resulting from the difference in gas pressure between the melting and casting chambers. Inoue [36] reported that $Zr_{55}Al_{10}Ni_5Cu_{30}$ alloys were produced by suction casting method in cylindrical shape with a diameter of 16 mm and a length of about 60 mm.

2.5 CRYSTALLIZATION OF BULK METALLIC GLASSES

When a glass is heated below T_n as shown in Figure 2.2 and held at that temperature for sufficient period of time it begins to crystallize. The study of crystallization kinetics is very important since the change in properties of the novel bulk metallic alloys during crystallization determine their long term stability, which is essential

for their practical applications. In addition, some microstructural features which have high potential application areas can be obtained via the devitrification of bulk metallic glasses.

Bulk glass forming alloys crystallize through the nucleation and growth processes. According to the classical nucleation and growth theory, the homogenous nucleation rate I, and the growth rate U of a crystalline phase formed from an undercooled melt can be defined by [54]:

$$I = \frac{10^{30}}{\eta} \exp\left[\frac{-16\pi}{3} \cdot \frac{\Delta S_f \alpha_m^3 T^2}{N_A k_B \left(T_l - T\right)^2} \right] \tag{2.16}$$

$$U = \frac{k_B T}{3\pi a_0^2 \eta} \left[1 - \exp\left(- \frac{\left(T_l - T\right)\Delta S_f}{RT} \right) \right] \tag{2.17}$$

where η is the viscosity, f the fraction of nucleation sites at the growth interface, α a factor depending on the atomic arrangement at the interface and has a value close to unity, ΔS_f the change in entropy per mole of alloy due to melting, T the temperature of the melt, R the universal gas constant, k_B the Boltzmann's constant, a_0 is the mean atomic diameter, and N_A Avagadro's number.

Crystallization reactions are grouped into three mechanisms; namely polymorphous, primary and eutectic crystallization. A crystal with a different composition from that of the matrix is formed by primary crystallization, whereas in polymorphous crystallization involves the precipitation of the crystal phase having the same composition as that of the matrix. Due to the eutectic reaction involved, the glassy matrix separates into two crystalline phases in eutectic type crystallization. Bulk metallic glasses crystallize by one of the above mechanisms. The activation barrier to crystallization and the thermodynamic driving force decide which of the mechanisms occurs [68].

2.5.1 Phase Separation

At certain compositions the initial glassy phase separates into two glassy phases to lower its free energy. This is called *phase separation* and can take place by one of two possible microstructural mechanisms: (1) mechanism in which the phase separation occur by nucleation and growth processes due to the activation energy barrier in front of the phase separation, (2) mechanism in which spinodal decomposition occurs with no activation energy barrier [68].

The phase separation becomes a rate-limiting step in crystal nucleation for most of the glass forming alloys. Should phase separation not take place, crystal nucleation would require longer times scales and glass formation would be improved. In fact, it is a general property seen in deeply undercooled metallic liquids with optimum glass forming ability [23].

2.5.2 Structural Relaxation

Glasses are thermodynamically unstable systems relative to an internal equilibrium liquid state and relax structurally to the latter state if held at a temperature in the glass transition region at a rate depending on the previous history and temperature. At lower temperatures, the glasses produced by rapid solidification having a frozen-in disorder and thus higher diffusivity relax structurally. The physical properties change during the structural relaxation. During the isothermal relaxation, the enthalpy, entropy, and volume of the glassy state decrease [69].

The main types of experiments used to study relaxation behaviour are stress relaxation, volume relaxation, enthalpy relaxation, dielectric loss, creep, and inelastic behavior [70]. The relaxation state of amorphous materials can be monitored by peak height of the heat flow at the glass transition during heating at a constant rate. Relaxed samples exhibit an endothermic overshooting of the heat flow

in the glass transition signal, which represents the recovery of the enthalpy released during the isothermal heat treatment [69].

Gallino et al. [69] developed a novel experimental method which allows the direct detection of the enthalpy relaxation during isothermal annealing in a differential scanning calorimeter (DSC). They presented a schematic illustration of the isothermal enthalpy relaxation signal as shown in Figure 2.11. The relaxation continues with an exothermic heat release and the amount of released enthalpy decreases with time during the relaxation process. They concluded that the glass state relaxes completely into the supercooled liquid far below the glass transition for the $Zr_{58.5}Cu_{15.6}Ni_{12.8}Al_{10.3}Nb_{2.8}$ alloy.

Surana et al. [71] studied the effect of experimental conditions on the measurement of enthalpic relaxation by using DSC and showed that the heating rate used in DSC has a significant effect on the calculation of enthalpic relaxation in a way that the change in enthalpy increases with the a decrease in the heating and cooling rate.

2.5.3 Crystallization Kinetics

Since the overall crystallization of amorphous alloys occurs by means of nucleation and growth processes the rate of overall transformation reflects the time and temperature dependence of both [68]. Johnson-Mehl-Avrami- Kolmogorov (JMAK) model [72] are generally used to describe the isothermal transformation kinetics of amorphous alloys and Kissenger [75] or Ozawa [76] analysis is usually used for the determination of activation energy of crystallization using non-isothermal DSC scans.

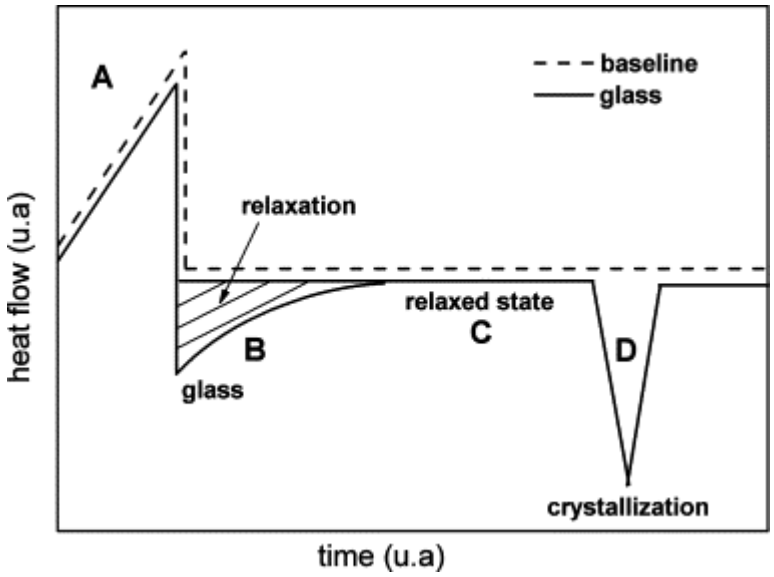

Figure 2.11 Schematic representation of the enthalpy relaxation signal. The continuous line is the signal for glassy state, whereas the dashed line is the schematic baseline of the crystalline sample subjected to the same anneal. The glass first relaxed into the supercooled liquid (relaxed) state and crystallized with further isothermal annealing. The regions marked as A-D indicate: (A) the heating of the sample with constant heating rate up to a selected temperature; (B) the exothermic heat release due to the relaxation at the beginning of the isothermal annealing at this temperature; (C) the supercooled liquid or relaxed state, (D) the crystallization event. (Adapted from [69]).

2.5.3.1 Isothermal crystallization kinetics-JMAK analysis

Avrami [74] stated that the general S-shape of transformation-time curve is characteristic of phase transformations at lower supercooling temperature. He assumed that the new phase is nucleated by germ nuclei, number of which can be altered by previous treatment and the density of germ nuclei gradually diminishes by becoming critical nuclei or by ingestion of them by other rowing nuclei. The other studies [72-74] and together with Avrami's work lead to a well known JMAK equation expressed as:

$$X(t) = 1 - \exp(-kt^n) \qquad (2.18)$$

where X(t) is the fraction of transformed material during crystallization, k is a nucleation and growth rate dependent constant, t is the time when the crystallized fraction reaches X(t), and n is an exponent characteristic of the experimental conditions. Constant k involves all the temperature dependent terms since thermal activation has a strong effect on the growth through boundary/interface mobility. n is associated with the geometry of the transformation. Two well defined limits have been reported in the literature: When all the nuclei are present and begin to grow at the beginning of the transformation, exponent n is equal to 2 (in two dimensions) and the nucleation is termed *site saturation.* On the other hand, when new nuclei appear at every step of the transformation, n=3 and the process is named as *continuous nucleation* [77].

The most commonly used way to analyze the kinetics of crystallization is to plot (–ln(1-X)) against time on a double logarithmic plot. This kind of plot is named as JMAK plot and is a straight line with a slope n. An example of a JMAK plot is given in Figure 2.12.

The methods to obtain the transformed fraction include measurement of grains from micrographs; measurement of properties like hardness, electrical resistivity, and optical properties; and calorimetry. There have been a lot of studies [1, 78-85] on the crystallization kinetics of bulk metallic glasses using JMAK analysis using calorimetry to determine the transformed fraction from the area under the exothermic crystallization peaks at the time of concern.

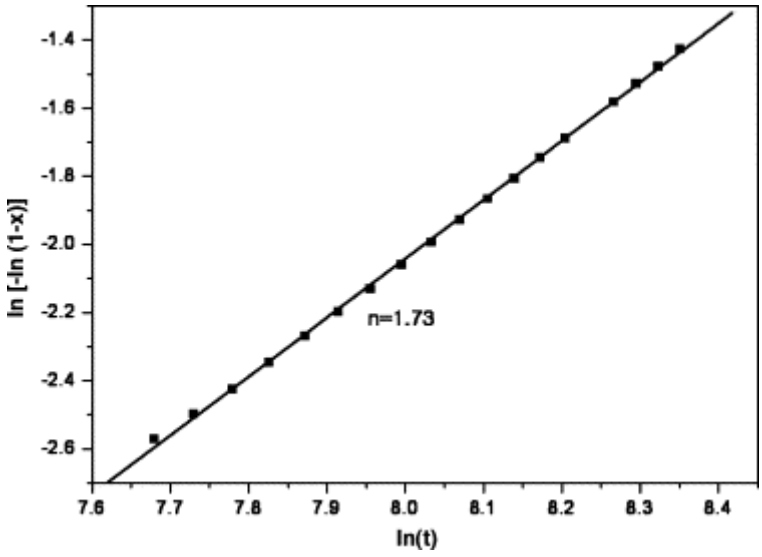

Figure 2.12 JMAK plot of ln[−ln(1 − *x*)] against ln(*t*) for $Cu_{43}Zr_{43}Al_7Ag_7$ alloy showing a characteristic straight line with a slope *n*. Adapted from [78].

Constant *k* in Equation (2.18) is related to annealing temperature by the expression:

$$k = k_0 \exp\left(-\frac{E_a}{RT_a}\right) \tag{2.19}$$

where k_0 is a constant and E_a is the activation energy for crystallization. The value of *k* and *n* are obtained from JMAK plots for different annealing temperatures. The slope of the straight line obtained by plotting of ln k versus $1/T_a$ gives the activation energy. Therefore, the activation energies for different temperature intervals can be obtained.

2.5.3.2 Non-isothermal crystallization kinetics: Kissenger and Ozawa Methods

The change in heat content and in thermal properties of a sample due to a reaction occurring is reflected by a peak in differential thermal analysis (DTA) or DSC curve. Provided that all the other experimental conditions are held constant, if the

reaction proceeds at a rate varying with temperature, i.e., possesses activation energy, the position of the peak temperature changes with the heating rate [75]. In his well known study, Kissinger [75] proposed a method for determining the activation energy of a simple decomposition reaction regardless of reaction order by making differential analysis patterns at different heating rates. He related the heating rate of a reaction to the peak temperature recorded by thermal analysis by an expression:

$$\ln\left(\frac{\phi}{T_p^2}\right) = -\frac{E_a}{R\,T_p} + A \qquad (2.20)$$

where ϕ is the heating rate in Kelvin per second (K/s), T_p is the peak temperature, R is the gas constant, E_a is the activation energy for the corresponding transition, and A is a constant. Plotting $\ln(\phi / T_p^2)$ versus $1/T$ yields a straight line whose slope gives the activation energy for crystallization. A series of DSC scans at different heating rates are conducted and peak temperatures for the transformations under investigation are recorded. Using the temperatures obtained form the non-isothermal scans are then used to construct the Kissenger plots. Figure 2.13 shows curves for non-isothermal DSC scans and resulting Kissenger plots showing the activation energies for both glass transitions and crystallization.

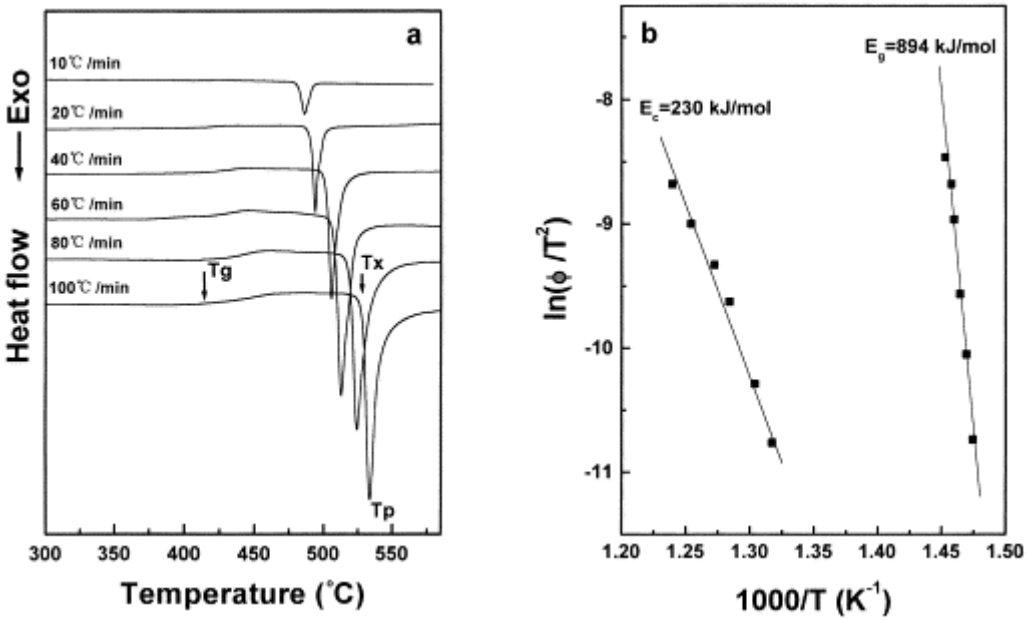

Figure 2.13 (a) Continuous heating DSC curves of $Zr_{55}Cu_{30}Al_{10}Ni_5$ bulk amorphous alloys at different heating rates, (b) Kissenger plots of the glass transition and crystallization from which the activation energies for glass transition and crystallization are obtained [84].

Another widely used non-isothermal method is the Ozawa method [76] which utilizes the expression:

$$\ln \phi = -1.0516 \frac{E_c}{R T_p} + \text{constant} \qquad (2.21)$$

where ϕ is the heating rate and E_c the activation energy. As in Kissenger analysis, a plot of $\ln \phi$ versus $1/T_p$ gives a straight line with a slope of $-1.0516\ E_c/R$. Yuan et al. [1] used both Kissenger and Ozawa analysis in their kinetic study on $Co_{43}Fe_{20}Ta_{5.5}B_{31.5}$ alloy and observed that the activation energy obtained by the Ozawa method is slightly lower. They further stated that the activation energy value obtained by Kissenger analysis at low heating rates is very close to the one obtained by isothermal analysis.

2.5.4 Methods Used in Critical Cooling Rate Calculations

Determination of the critical cooling rate is very important in studying crystallization kinetics since is the minimum rate to avoid crystallization. Besides being a decisive factor in evaluating GFA, critical cooling rate should be estimated when a certain BMG is to be used in a process, which requires certain critical cooling rate. Several experimental and theoretical methods are available to determine the critical cooling rate.

2.5.4.1 Quantitative evaluation of critical cooling rate

Inoue et al. [86] proposed a method for the quantitative evaluation of critical cooling rate for metallic glasses starting from a fundamental equation defined by:

$$R_c = Z\frac{T_m}{\tau} = Zf T_m \tag{2.22}$$

where R_c is the critical cooling rate, Z the constant of 2×10^{6}, f the rate constant in jumps/s related to diffusion or viscosity, and T_m the melting temperature. Eyring's equation relates the rate constant f to k, by the equation:

$$f = \frac{k_B T}{a^3 \eta} \tag{2.23}$$

where a is the interatomic distance and η is the viscosity. When Equation 2.23 is substituted into 2.22, one can get the critical cooling rate expressed by:

$$R_C = Z\frac{k_B T_m}{a^3 \eta_{T=T_m}} \tag{2.24}$$

They further modified the Equation 2.26 for metallic glasses by taking into account the effect of decrease in R_c on alloying and developed a new relation:

$$R_C = Z\frac{kT_m}{a^3 \eta_{T=T_m}} \exp\left(\frac{\Delta G}{RT}\right) \tag{2.25}$$

indicating that a large negative value of ΔG has a large tendency to decrease R_c. ΔG of pure elements is zero and therefore, the modification is only adopted for the systems with two or more elements. Since ΔG is composed of two terms, regular solution model term and misfit excess entropy terms, fitting parameters related these two terms at 300 K were put as f_1 and f_2 and final form of critical cooling rate equation is in the form:

$$R_C = Z \frac{kT_m}{a^3 \eta_{T=T_m}} \exp f_1 \frac{\Delta H \quad T_m \Delta S^{ideal}}{300R} \quad f_2 \frac{T_m S_\sigma}{300R} \qquad (2.26)$$

where ΔS^{ideal} is the ideal configurational entropy and S_σ mismatch term of entropy resulting from atomic size. Further, f_1 and f_2 were determined to be 0.75 and 1.2 respectively by the method of least-squares [86].

2.5.4.2 Measuring the critical cooling rate by analyzing crystallization peaks from continuously cooled melts

In a recent study of Ray et al. [87], three commonly used methods for estimating R_c involving the analysis of crystallization peaks from continuously cooled melts were listed as given below.

Method I: Continuous-cooling- temperature (CCT) diagram

Plotting the onset temperature for crystallization T_c against time needed to crystallize the melt when cooled from the melting temperature T_m at a rate R produces a curve, known as continuous-cooling-temperature (CCT) diagram as shown in Figure 2.14. The inset in the figure indicates that temperatures lower than those represented by the solid curve in the CCT diagram cannot be achieved by continuous cooling without crystallizing the melt, only the upper half can be experimentally determined for a CCT diagram. The dashed line is actually a mirror image of the experimental curve [87]. T_n is called the nose temperature at which the transformation is the fastest and t_n is defined as the corresponding time known as

nose time. Uhlmann [88] used these parameters to determine the critical cooling rate and developed a relation expressed by:

$$R_c = \frac{T_m - T_n}{t_n} \tag{2.27}$$

The method of calculating R_c by using nose temperature and time is called the *nose method*. However, this method overestimates R_c, since it assumes that the crystallization rate corresponds to the nose of the CCT curve throughout the whole temperature range T_m to T_n [89].

Method II: Identifying the cooling rate curve for which no crystallization peak is observed

An exothermic crystallization peak is observed at T_c when a melt is cooled at a sufficiently cooled from the melting temperature. T_c occurs at progressively lower temperatures and the height of the crystallization peak, h, decreases as the cooling rate, R, is increased as shown in Figure 2.14. R_c is taken as the cooling rate at which the crystallization peak just disappears [87].

Method III: An empirical equation for evaluation of cooling curves

It is quite time consuming to experimentally establish CCT curves, and it is not yet possible to theoretically calculate curves due the lack of an accurate expression for the nucleation rates [90].

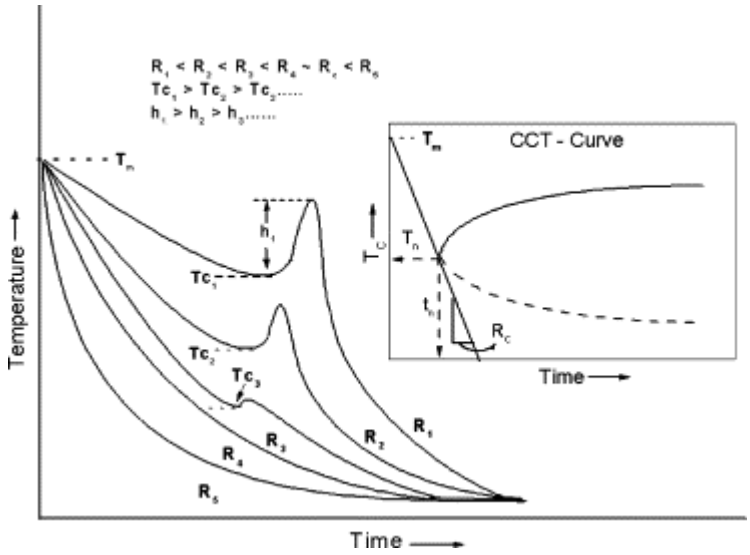

Figure 2.14 Schematic of a typical temperature-time cooling curves for a hypothetical melt when cooled at different rates, *R*. The melt crystallizes when cooled from T_m at rate less than the R_c crystallization is indicated by an exothermic peak. The onset temperature for crystallization, T_c, and the height of the peak, *h*, decrease with increasing *R*, and the *R* for which the crystallization peak just disappears is the R_c. The inset shows a continuous-cooling-temperature diagram based on the temperature-time-cooling curves [87].

Barandiaran and Colmenero [89] solved this problem by developing an experimental method to estimate the R_c which involves determining crystallization temperatures when a liquid is cooled in a DTA or DSC equipment at different rates, *R*. They proposed that on cooling a liquid, R is related to $\Delta T_c = T_m - T_c$ by the expression:

$$\ln R = \ln R_c - \frac{B}{\Delta T_c^2} \qquad (2.28)$$

where *B* is constant and has unit in K^2. The intercept of the plot of *lnR* versus $1/\Delta T_c^2$ gives the lnR_c.

2.5.5 Nanocrystallization of Bulk Metallic Glasses

Materials with microstructural features of nanometric dimensions are referred to in the literature as nanocrystalline materials (a very generic term), nanocrystals, nanostructured materials or nanophase materials. Nanostructured solids is perhaps the most accurate description, even though nanocrystalline materials will be the appropriate term if one is dealing with solids with grains made up of crystals [91]. They have a significant fraction of their atoms in defect environments such as grain or interface boundaries due to their extremely small dimensions [92]. A nanocrystalline material, for instance, with an average size of 5 nm has about 50% of its atoms in the first two nearest-neighbour planes of a grain boundary, in which there exist atomic displacements from the normal lattice sites [93].

Nanocrystalline materials can be produced by various methods and starting from different phases, such as vapour (inert gas condensation, sputtering, plasma processing, vapour deposition), liquid (electrodeposition, rapid solidification) or solid (mechanical alloying, severe plastic deformation, spark erosion) [91,94,95]. Most of the methods offer two possibilities for creation of nanocrystalline structure: (1) directly in one process, or indirectly through an amorphous precursor. Nanocrystallization of metallic glasses is an example of the second procedure [96]. The amorphous solids are in thermodynamically metastable states and they will transform into more stable states under appropriate conditions. Crystallization is such a transformation involving an amorphous phase crystallizing into one or more metastable or stable polycrystalline phases. The crystallization of amorphous solids into nanometre-sized polycrystalline phases (say, less than a few hundred nanometres) is termed as “nanocrystallization”. It can be achieved by either isothermal or non-isothermal annealing in various amorphous solids of metallic alloys and semiconductors. Due to the contamination and grain growth, nanostructured materials produced in the standard way, through the compaction of nanocrystal powders, have not realized the expected superior properties. Whereas, considerably greater tensile strengths are obtained in nanocrystalline structures

obtained by the crystallization of metallic glasses [97]. Nanocrystal formation in metallic glasses takes place in two steps: (1) formation of amorphous state by quenching of liquid alloy and (2) partial or complete crystallization of the amorphous alloy by annealing. Metallic glasses can be considered as materials which are kinetically metastable and thermodynamically unstable. Most of them are stable at temperatures close to the room temperature and can be transformed to crystalline state at temperatures close to the room temperature [96]. Inoue [98] stated the four criteria to have a mixed structure consisting of nanoscale crystalline particles embedded in an amorphous phase as:

1. multistage crystallization process;
2. existence of homogeneous nucleation sites in an amorphous phase;
3. suppression of growth reaction caused by segregation of a solute element with low atomic diffusivity at the nanocrystal/amorphous interface; and
4. high thermal stability of the remaining amorphous phase by the enrichment of solute elements from the primary crystalline phase.

The basic principle of the crystallization of amorphous solids is to control the crystallization kinetics by optimizing the heat treatment conditions, such as annealing temperature and time, heating rate, etc.). As a result, the amorphous phase crystallizes completely into a polycrystalline material with ultra-fine crystallites. The complete crystallization of amorphous solids is being established as a promising method for synthesis of nanocrystalline materials because it possesses some unique advantages such as;

- it is very simple and convenient to control the preparation procedures. Modifying the heat treatment conditions gives variable grain sizes with a wide size range (from a few nanometres to submicrometers) in the as-crystallized nanocrystalline specimens [99];
- the complete crystallization method is an efficient way to obtain porosity-free nanocrystalline materials [100]. Since artificial consolidation process is not involved and the nanometre crystallites and their boundaries are produced by

means of a solid state phase transformation, the nanocrystalline sample is dense and clean in the interfaces;

- different kinds of interfacial structure (coherent, semicoherent, and completely incoherent) can be obtained by this method providing more opportunities for investigation of the nature of these nanocrystalline interfaces;
- by means of the crystallization method, some nanocrystalline intermetallics, supersaturated metallic solid solutions, and composites can be easily synthesized.

The main focus of the crystallization method is on the control of crystallization kinetics by optimizing the heat treatment conditions, such as annealing temperature and time, heating rate, etc. to obtain the amorphous phase partially or completely transformed into nanocrystalline material. It is expected that the amorphous phase separation has a strong potential for increasing the nucleation rate, and to decreasing the growth rate of crystals. Nucleation can start only after amorphous phase separation, thus leading to significant incubation times for crystallization. Due to the compositional changes induced by the phase separation and/or interference between the growing crystals and the amorphous regions, phase separation is expected to reduce the crystal growth rates [101].

2.6 PROPERTIES AND APPLICATIONS OF BULK METALLIC GLASSES

Their lack of crystallinity and lack of microstructural features such as grain boundaries are the defining characteristic of metallic glasses compared to conventional metallic materials [102]. Since their first discovery, bulk metallic glasses have been known as superior properties. The following sections focus on mechanical, magnetic, and chemical properties by giving examples from representative systems.

2.6.1 Mechanical Properties

The mechanical behaviour of bulk metallic glasses can be studied in the as-cast condition, in the supercooled liquid region, after partial or full devitrification into bulk nanocrystals and quasicrystals. Fracture occurs along the maximum shear plane at 45˚ to tensile axis and exhibits a well developed vein pattern when the alloy is in the fully amorphous state. A mixed structure of nano-sized particles embedded in the amorphous matrix of the annealed $Zr_{65}Al_{7.5}Ni_{10}Cu_{7.5}Pd_{10}$ alloy showed higher compressive fracture strength of 1820 MPa together with a much improved plastic elongation of 0.5 % as compared with those (1630 MPa and nearly 0 %) for the corresponding amorphous single phase alloy with the same alloy composition [103]. In tensile loading, the elastic strain limit of metallic glasses is much higher than that of common crystalline metallic alloys. Thus, the yield strength of amorphous alloys is relatively high in tension and compression. Metallic glasses, upon yielding, often exhibit plastic flow in absence of work hardening and a tendency towards work softening leads to shear localization. Under tensile condition, the localization of plastic flow into shear bands limits dramatically the overall plasticity; therefore the failure of metallic glass specimens usually occurs catastrophically on one dominant shear band [23].

There is enough data available on metallic glasses, mostly BMGs, to allow for the quantitative comparison of their properties with conventional engineering materials. Figure 2.15 shows elastic limit σ_y and Young's Modulus E for over 1500 metals, alloys and metal-matrix composites. The ellipses enclose the range of values associated with given materials and material groups on materials-selection charts of this kind. The metallic glasses lie on the upper edge of the populated region [102].

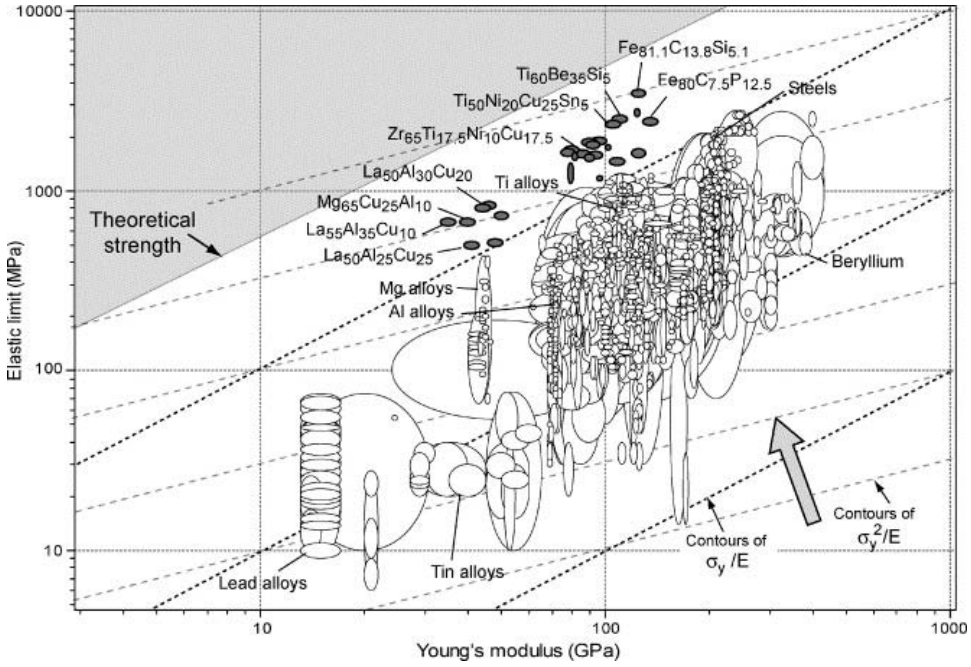

Figure 2.15 Elastic limit σ_y and Young's Modulus E for over 1507 metals, alloys and metal-matrix composites and metallic glasses. The contours show the yield strain σ_y/E and the resilience σ_y^2 / E [102].

The contours shown in Figure 2.15 give the material indices σ_y/E and σ_y^2 / E which are the yield strain and the resilience, a measure of the ability of a material to store elastic energy, respectively. As can be seen in Figure 2.15 easily, metallic glasses have larger yield strength and storing more elastic energy per unit volume than any of the other materials on the plot [102].

2.6.2 Magnetic Properties

Bulk metallic glasses are known for their good soft magnetic properties. The term "soft" indicates that the response of the magnetization to an applied field is large and this is a desirable property for such applications as transformers and inductors. It also implies that they have low coercivity, large saturation magnetization, and small magnetorestriction. Inoue [59] described the relationship of soft magnetic properties

of new Fe- and Co-based amorphous alloys with high thermal stability of supercooled liquid before crystallization and high GFA in melt-spun ribbons and cast bulk cylindrical forms. They found that the present Fe-based amorphous ribbons have good soft magnetic properties and Co-based amorphous alloys have also good soft magnetic properties and high stability of supercooled liquid against crystallization. Later, Majumdar et al. [66] studied the magnetic properties of $Fe_{56}Co_7Ni_7Zr_{10}B_{20}$ and found that the cast alloys exhibit good soft magnetic properties in the amorphous and amorphous plus crystalline phase regions. They observed a sharp increase in coercivity on transition to the fully crystalline state.

2.6.3 Chemical Properties

Although it is not expected since they are in a higher energy state, the corrosion resistance of metallic glasses is high. This is mainly attributed to the absence of defects and chemical homogeneity. The composition of the BMG is very important. Cr, Mo, and P can enhance corrosion resistance and also Nb- and Ta-containing amorphous alloys exhibit very good corrosion resistance in HCl and NaCl solutions [61].

The catalytic properties of BMGs are also worth mentioning. They have some unique properties which make them interesting materials in catalysis. Recently, they have been used as catalyst precursors and several efficient catalysts have been prepared by various pretreatments of the metallic glasses [104].

2.6.4 Applications

Bulk metallic glasses are adopted for application in various fields. One of the great advantages of BMGs is the ease of formation of complicated shapes. BMGs have already been used as die materials (Pd-Cu-Ni-P BMG), sporting equipment

(ZrTiCuNiBe and ZrTiNiCu BMG) and electrode materials (PdCuSiP BMG). The development of Fe-based BMGs has reached the final stage for application as soft magnetic materials for common choke coils [59].

The property-application relationship of BMGs is summarized below to give a general understanding of their application fields. The high hardness suggests the use of BMGs as *precision tooling*. The absence of grain structure allow a blade to be sharpened to an exceptional edge since there is no length scale above the atomic to limit it, and this is useful for the application in scalpels.

Their high elastic energy storage per unit volume and mass, the low damping, make the metallic glasses suitable for *springs*. Their successful use in golf-club heads and in tennis racket frames comes from this property.

The lack of grain structure together with the high hardness suggest that features of near-atomic scale could be moulded or etched into a metallic-glass surface to make masters for reproducing *high-density digital data*. Since they can take high polish and resist abrasion and corrosion, they are used as *fashion items* such as, rings, spectacle frames, watch cases, and mobile phone cases [102].

CHAPTER 3

EXPERIMENTAL PROCEDURE

3.1 ALLOY PREPARATION

3.1.1 Raw Materials

The materials used for the preparation of $Fe_{60}Co_8Mo_5Zr_{10}W_2B_{15}$ alloy differed from one sample to the other. For some samples the high purity elements Fe (99.97% purity), Co (99.9% purity), Zr (99.8% purity), Mo (99.95% purity), W (99.9% purity) and commercially available FeB master alloy were used. FeB alloy was used as a source of iron and boron and its composition was analyzed by an inductively coupled plasma optical emission spectrometer provided by Central Laboratory. The results of this analysis are given in Table 3.1. For the other samples, pure B (99.95% purity) were used together with the other high purity constituent elements. All the constituent elements were first cut into small pieces before mixing in desired proportions.

3.1.2 Alloy Preparation Methods

Two methods were utilized, namely the *induction heating* and *arc melting* methods. In the induction heating method, the constituent elements were mixed in the alumina crucible where they were melted using the induction heating of the centrifugal casting machine.

Table 3.1 Composition of the FeB alloy in weight percent

Element	Weight %
Fe	79.75 ± 0.43
B	17.88 ± 0.20
Al	0.053 ± 0.003
Si	0.259 ± 0.015
S	0.0043 ± 0.0003
P	0.07 ± 0.003

The induction melting procedure of an alloy generally takes place by the following steps:

- The constituent elements are cut into small pieces and weighed out. They are added until the desired alloy composition was obtained.
- The constituent elements are then cleaned by rinsing with ethyl alcohol.
- They are put into the alumina crucible which is placed inside of the induction coil.
- They are heated until the melting was achieved under the protective argon atmosphere.
- This melting process is repeated to homogenize the alloy.

Arc Melting method, however, allow for the preparation of more homogeneous master alloy ingots. In the arc melting method, the mixture of elemental components was placed on a copper-hearth inside an arc-melting chamber which was evacuated to 5×10^{-5} mbar and backfilled with argon gas three times. To ensure homogeneity, the samples were flipped and remelted several times by arc-melting. The sample was allowed to cool down, removed from the copper hearth and weighed to check for any weight losses. A rod-shaped master alloy ingot was obtained and then it was cut into slices in 1 mm thickness by wire-erosion machine.

Master alloy ingot prepared by arc melting or induction heating methods was then put into an alumina crucible. The composition of alumina used in making the

alumina crucibles is given in Table 3.2. The alumina powder was mixed with water and cast into steel dies when a mushy mixture was obtained. Then it was left at the ambient temperature for 24 hours for drying.

Table 3.2 Composition of alumina used in crucible production

Compounds	**Weight %**
Al_2O_3	~97.0
SiO_2	max. 0.2
Fe_2O_3	max. 0.1
CaO	max. 1.6

The alumina crucibles produced this way were observed to have many cracks and a lot of porosity which lead to unwanted break downs during melting and casting of the alloys. Therefore, the production process was improved by designing a new die made of polyamide. Internal surface of this new die was very smooth allowing the production of alumina crucibles with surfaces which were more smooth and free of cracks. The shape of this new die can be seen in Figure 3.1. Early observations during the melting showed that the alumina crucible reacted with the master alloy ingot. To solve this problem, the crucibles were coated with a boron nitride refractory paint.

Alumina crucibles were heat treated to ensure their thermal stability before they were used in casting experiments. The heat treatment procedure is shown in Figure 3.2.

(a) (b)

Figure 3.1 (a) Polyamide moulds used in alumina crucible production. (b) Two crucibles with the one on the left hand side was prepared by the polyamide mould free of surface cracks and the one on the right hand side produced by conventional technique containing cracks.

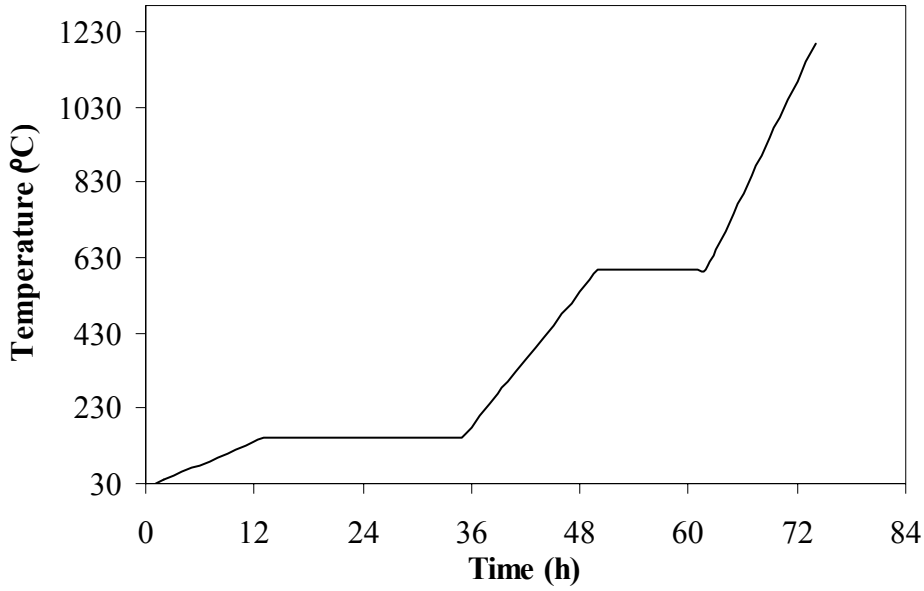

Figure 3.2 Heat treatment procedure applied to alumina crucibles.

3.2 BULK METALLIC GLASS FORMATION

Two methods were utilized to produce amorphous structure. First method was the previously used method involving the quenching form the liquid state. The other method was performed for the first time involving the quenching from the semi-solid state.

3.2.1 Quenching from the Liquid State

The rapid solidification of samples was carried out using copper mould casting method. A centrifugal casting machine under the protective atmosphere of argon gas was used for this purpose. The melting and casting chamber was airtight and casting was achieved by the injection of the molten alloy into the wedge-shaped copper mould mounted on a rotating arm through the action of centrifugal force. The sequence of events for copper mould casting of an alloy can be described as follows:

- The alumina crucible with a small opening approximately in one 5 mm diameter is placed inside the RF heating unit.
- The copper mould is placed at the opposite of the alumina crucible while its opening fits into opening of the copper mould.
- The master alloy ingot is put into the crucible
- The melting chamber is closed and evacuated by argon flashing at least two times.
- Melting is achieved using RF heating supplied by an induction coil.
- The temperature of the sample was monitored with an optical pyrometer to ensure that the heating is sufficient for casting.
- The sample is allowed to cool down after the casting and casting procedure is completed.
- Then the mould is removed from the apparatus and the sample is removed from the mould.

The wedge-shaped copper moulds with a maximum thickness of 4 mm and a cylindrical mould were used to observe the effect of different cooling rates along the specimen length. The technical drawings of copper moulds used throughout this study are given in Figure 3.3. Since the variable thickness causes the variance in cooling rate, the wedge shape specimens were cut into several pieces to observe the effect of different cooling rates along the specimens by using Buehler Micro-cutter. The cylindrical specimen, on the other hand, was cut into slices to evaluate its microstructure from outer to inner radial distance.

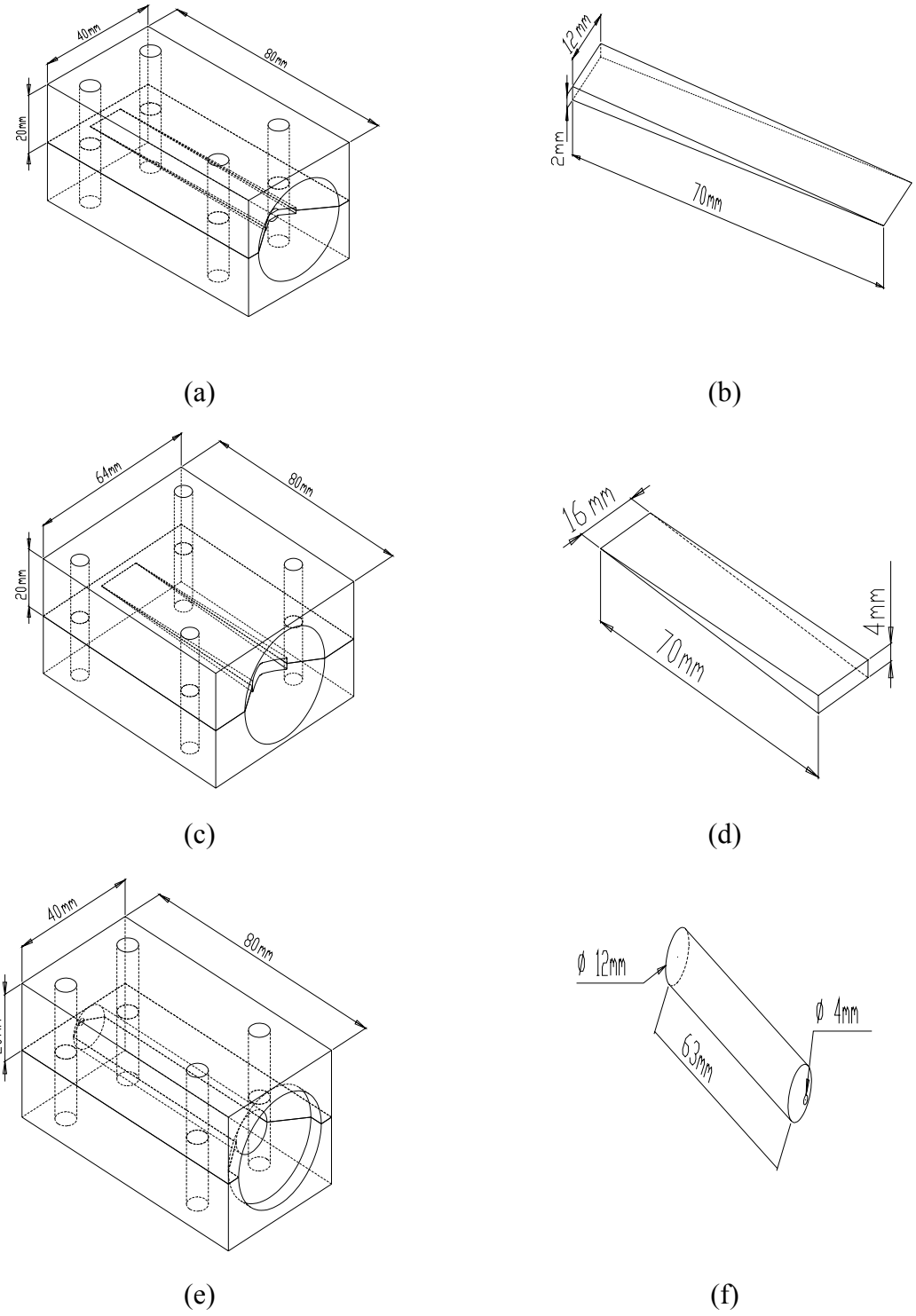

Figure 3.3 Technical drawings of the moulds. (a) Mould1, (b) inner wedge shape of mould1, (c) mould 2, (d) inner wedge shape of mould2, (e) mould 3, (f) inner cylindrical shape of mould 3.

3.2.2 Quenching from the Semi-Solid State

The aim of the quenching experiments was to see whether the amorphous phase was achievable when the alloy was rapidly cooled from the semi-solid state. Experimental setup designed for quenching the alloy specimens is shown in Figure 3.5. The induction heating of the centrifugal casting machine was used for heating the sample to the required temperatures. The temperatures between the eutectic and peritectic temperatures, like 1000 and 1050°C, were selected. The temperature of the specimen was read by a pyrometer. The accuracy of the pyrometer was checked by a separate melting experiment using a pure copper specimen with a melting temperature of 1084 °C. It was observed that the pyrometer read 35 °C lower than the actual temperature. The quenching experiment was conducted with the continuous flow of argon atmosphere to minimize the oxidation effect. After reaching the required temperature, the mushy specimen was dropped into a water bath which was at 0 °C.

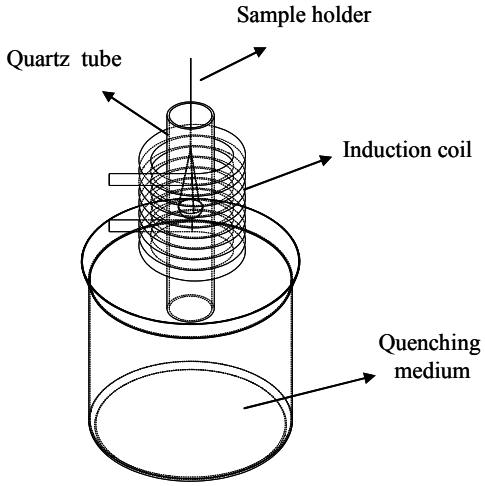

Figure 3.4 The experimental set-up used in quenching experiments.

3.3 EQUILIBRIUM SOLIDIFICATION OF THE MASTER ALLOY

Since the master alloy ingot prepared by arc melting method contain non-equilibrium structures due to the rapid solidification obtained in the water cooled copper hearth of the arc-melting device, the equilibrium cooling conditions were applied to the master alloy in the furnace. One representative master ingot sample were placed in a quartz tube and heated to 1000 °C by a rate of 20°C/min and held at that temperature for one hour and cooled to room temperature in the furnace under continuous argon flow. An electrical furnace with a controlled atmosphere was used for this purpose.

3.4 SAMPLE CHARACTERIZATION

The as-prepared master alloy ingots and as-cast amorphous samples were analyzed by using different techniques to get detailed information about the phases present and microstructural features.

X-ray Diffractometry

X-ray diffraction (XRD) was performed using a Rigaku diffractometer. CuK_{α} radiation was utilized in the diffraction angle (2θ) range of 20-90°. XRD patterns were analyzed using qualitative analysis software.

Scanning Electron Microscopy

Scanning electron microscopy (SEM) studies were performed using a JSM-6400 Electron Microscope (JEOL) equipped with NORAN System 6 X-ray Microanalysis System & Semafore Digitizer. Energy dispersive spectroscopic analyses (EDS) were used whenever possible. The back-scattered mode was utilized when the existence of phases of different composition were expected. Secondary electron mode, on the

other hand, was used more frequently to differentiate between different solidification microstructures.

SEM sample preparation

Alloy ingots for the SEM analysis were first embedded in Bakelite and then polished using 320, 400, 600, 800, and 1200 grit SiC emery papers on a rotating wheel. The rotation speed was chosen as 300 rpm. Final polishing was done using 3 μm diamond paste on a cloth-lapping wheel. When necessary, 1 μm diamond paste was also employed. To see the different structures present in alloy samples, they were etched. 2 volume % nital or 5 volume % nital was used as enchants. After each step in preparation, sample was rinsed with water and washed with alcohol and dried before proceeding to the next step to avoid impurities.

Wedge-shaped samples usually embedded in bakalite along their long sides to see the differences in microstructure as the cooling rate varies along. However, cylindrical slice was examined both in plane condition and along the true thickness. Also, the heat treated samples were studied in plane condition.

Differential Scanning Calorimetry

Thermal analyses were conducted using Setaram Setsys 16/18 DSC under flowing high purity argon gas and a cooling system attached to the DSC. Temperature calibration was done using Ag, Au, Al, Ni, and Zn reference samples before starting the experiments. The same scanning rate of 20 °C/min was applied to characterization of all samples. Isothermal and non-isothermal runs were performed with 20-30 mg of sample under flowing high-purity argon gas atmosphere. Samples for DSC analysis were carefully prepared. Tiny pieces were cut from the bulk samples and cleaned with ethyl alcohol before they were put into alumina crucibles. To prevent sticking to the crucible walls, alumina powder was dispersed inside the crucible.

The DSC was used to observe thermal behaviour as well as the material's response to different heating and cooling rates. Also, it was utilized to estimate the critical cooling rate of the alloy in concern. DSC instrument measures the rate of heat release or absorption by the sample as a function of temperature. If an event takes place with heat absorption, such as melting, it is reflected as an endothermic peak in the DSC curve. On the other hand, exothermic peaks are the results of reactions taking place by heat release such as crystallization. The enthalpies of reactions and corresponding onset and peak temperatures are also found by processing DSC curves. The area under a peak gives the enthalpy of the reaction associated with that peak. The glass transition temperature and the onset crystallization temperatures were found by the intersecting the two linear lines adjoining the transition elbow of the DSC curve.

DSC Heating and Cooling Cycles

A series of DSC experiments were performed by using different heating and cooling rates. The main aim in doing these experiments was to see the effect of heating rate on characteristic temperatures of the alloy. In addition, observations on the change of the reactions during the heating and cooling cycles were also made. The master ingot slice was heated from room temperature to 1400 ºC, which is above the melting temperature of the alloy, and held at that temperature for 5 minutes to homogenize the melt. Then, it was cooled to 400 ºC with the same rate. The second cycle was performed by re-heating the alloy from 400 ºC to 1400 ºC and then cooling it to room temperature. The heating and cooling rates were kept constant for each couple of cycles but changed when the next one began. Heating and cooling rates of 20, 40, 60, 80, and 99 C/min were applied and resulting DSC curves were recorded. The sequence of heating and cooling cycles used in these experiments was given in Figure 3.4.

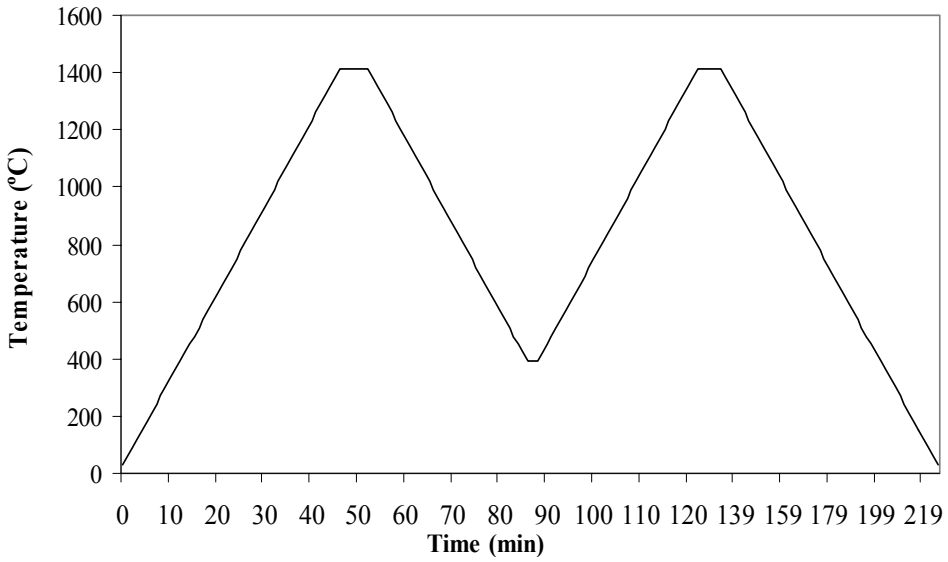

Figure 3.5 Heating and cooling sequence applied in some DSC experiments. For each couple of cycles, sample in the DSC crucible was changed**.**

3.4 CRYSTALLIZATION EXPERIMENTS

The crystallization experiments were done to observe the crystallization behaviour of the alloy. Two temperatures were chosen, one in the supercooled liquid region (650 °C), the other above the first crystallization temperature (750 °C). Two representative samples obtained by cutting small random pieces from amorphous cast 4 were put into the furnace and heated to temperatures in the supercooled liquid region and above the first crystallization temperature. The samples were put into a quartz tube and purged with the flow of high purity argon gas and then sealed with glass wool. High purity zirconium pieces also put into the quartz tube to minimize the oxidation during the heat treatment. The samples were heated to the desired temperatures and held at those temperatures for 5 hours. After this isothermal treatment, they were allowed to cool in the furnace to room temperatures. The

resultant microstructures were studied by using the SEM and XRD analyses were performed to observe if any phases were crystallized during this treatment.

The above experiment was repeated in DSC using the similar samples to investigate the possible crystallization peaks that could appear during the 5 hour period. A heating rate of 40 °C/min was used to heat the samples to the required temperatures. Each sample had been hold for 5 hours at these temperatures and the DSC curves showing heat flow versus time were recorded.

Also, non-isothermal DSC scans was performed on samples, which were confirmed to be amorphous by x-ray diffraction studies to estimate the glass transition and crystallization activation energies by the use of two analytical methods, namely the Kissinger and Ozawa methods. Heating rate was varied and resulting DSC scans were recorded. The heating rates of 5, 10, 20, 40, and 99 °C/min were employed. The mass of samples for each run was kept constant around 20 mg. The glass transition and exothermic peak temperatures were recorded against the heating rate.

CHAPTER 4

RESULTS AND DISCUSSIONS

The study aims in producing bulk amorphous $Fe_{60}Co_8Mo_5Zr_{10}W_2B_{15}$ alloy system, which was previously observed to have a high glass forming ability [6] and investigating its solidification and crystallization behaviours. First, the solidification behaviour of the master alloy ingot is presented Section 4.1. Then, the formation of amorphous $Fe_{60}Co_8Mo_5Zr_{10}W_2B_{15}$ alloy is discussed in the next section. The estimation of the critical cooling rate is presented in Section 4.3 before going into the details of crystallization kinetics. The results of the experiments on the crystallization behaviour of the alloy are presented and discussed in Section 4.4. For the sake of convenience, the binary phase diagrams among some of the constituent elements are given in the appendices.

4.1 THE SOLIDIFICATION BEHAVIOR OF $Fe_{60}Co_8Mo_5Zr_{10}W_2B_{15}$ ALLOY

The solidification behaviour of the alloy was studied in near-equilibrium and non-equilibrium cooling conditions. The near-equilibrium cooling conditions were provided by furnace cooling. The alloy was heated to 1000 ºC, held at that temperature for 1 hour and then allowed to cool to room temperature in the furnace. The resulting microstructure is presented in Figure 4.1. The eutectic structure was observed as in between the α-Fe crystallites, which appear as the dark contrasted phase in Figure 4.1 (a) and (b). The white contrasted phase surrounding the α-Fe crystallites, on the other hand, was indicative of a peritectic reaction. In general it can be said that the dark contrasted phase was the α-Fe crystallites, gray contrasted phase was a compound rich in Zr and the bright contrasted phase was a complex intermetallic phase.

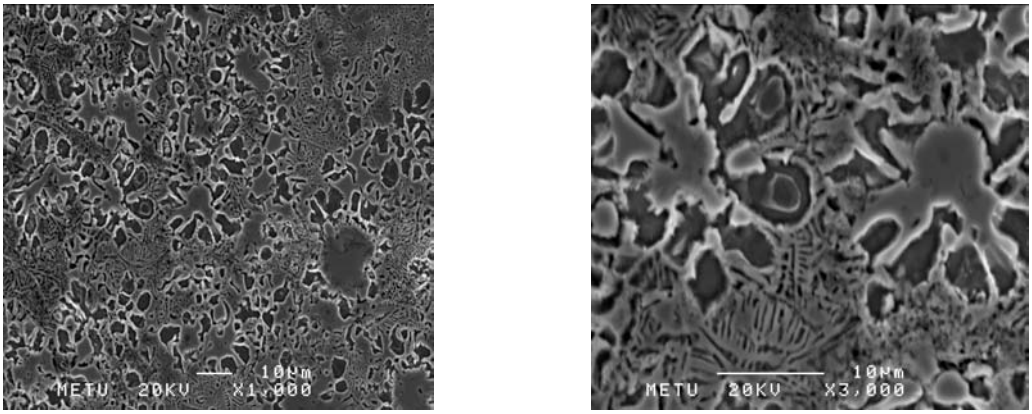

(a) (b)

Figure 4.1 The secondary electron (SE) images of the alloy annealed at 1000 ºC for 1 hour in the furnace magnified (a) 1000 times and (b) 3000 times to its actual size.

The non-equilibrium solidification conditions, on the other hand, were obtained by the arc-melting method. As-prepared master ingot rod was cut into the slices. A schematic drawing of a slice is given in Figure 4.2. The slice was contacted the water-cooled copper hearth of the arc-melting device on plane AA' as indicated in the figure. The other surfaces are free surfaces and cooled more slowly than the basal plane AA'. Therefore different microstructural features were expected for different regions along the true thickness of the specimen. These regions are indicated in Figure 4.2 by numbered circles and investigated by using the SEM.

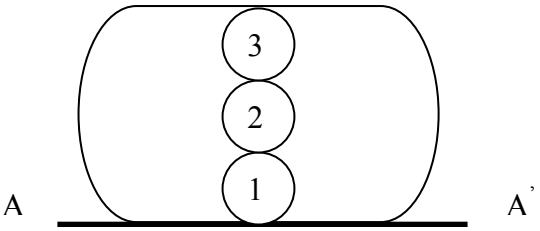

Figure 4.2 The schematic drawing of the master ingot slice showing examined regions indicated by numbers.

The microstructure of the bottom part of the sample, which is indicated by region (1) in Figure 4.2, is shown in Figure 4.3 (a). The eutectic structure could not be observed in this part. However, moving to the more slowly cooled regions, middle and upper regions, where the cooling rate was smaller, the eutectic structure started to be observed as given in Figure 4.3 (b) and (c). This immediately implied that the eutectic reaction was suppressed as the cooling rate was increased. EDS analysis results have shown that the dark contrasted phase in both regions given in Figure 4.3 (a), (b) and (c) is mainly α-Fe with a small amount of W dissolved in it. All of the elemental constituents of the alloy were found to exist in the gray contrasted phase indicating that it could be a complex intermetallic phase. The bright phase surrounded the α-Fe could not be resolved to obtain an accurate compositional analysis. By careful examination on the appearance of this phase, it was concluded that it could be a result of the solidification of a liquid phase, which could trapped in between the α-Fe crystallites. This feature supports the existence of a peritectic reaction.

The upper region of the slice, numbered as 3 in Figure 4.2, had different microstructural features since it is the most slowly cooled part of the specimen. As it can be seen in Figure 4.3 (c), dark contrasted dendritic α-Fe still existed as well as the unidentified gray contrasted phase. Eutectic structure became more discernable in this region since the achieved cooling rate is much slower. Also the α-Fe crystallites become larger in size. A dark gray contrasted phase having a needle like morphology was observed in this part as can be seen in Figure 4.3 (c). According to EDS analysis, it was mainly composed of Zr. It was predicted to be ZrB_2 phase which also appears in the XRD pattern of the sample given in Figure 4.4. It is a highly stable crystal phase as can be interpreted from the Zr-B binary phase diagram given in Figure A.1. Formation of the high melting ZrB_2 and α-Fe was expected since the studies found in literature on the solidification of similar master alloy ingot reported the formation of the same phases [105]. The presence of Fe_3Zr phase was somewhat unexpected since more stable $FeZr_2$ phase should have been formed as deduced from the binary Fe-Zr phase diagram given in Figure A.2. Also, in a study

on the phase equilibria of the Fe-Zr system [106], it was stated that the frequently reported Fe_3Zr phase was found not to be an equilibrium phase of the binary system. This implies that the arc-melting device provides a cooling rate higher than the cooling rate by which the alloy can solidify into its equilibrium phases

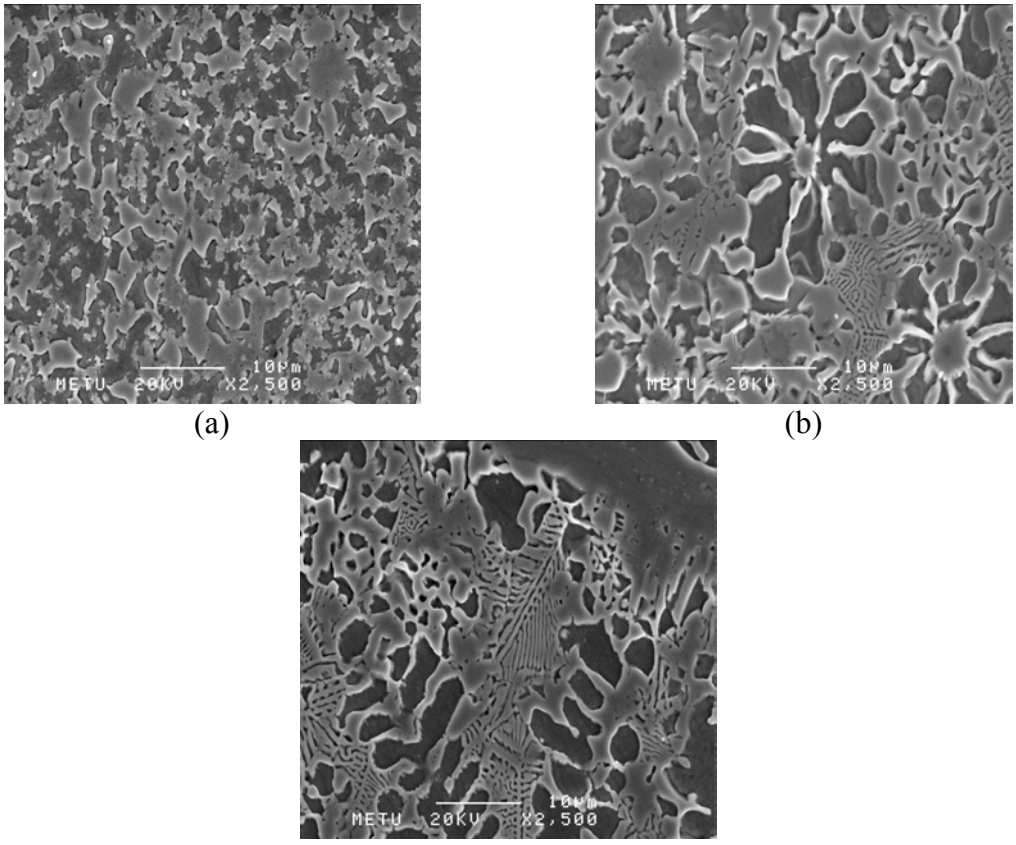

Figure 4.3 Secondary electron images of (a) bottom edge (region1), (b) the middle section (region 2), and (c) top section (region3) of the master alloy ingot. The eutectic structure starts to appear as the cooling rate is decreased.

Further investigation on the solidification of the samples was performed by using XRD and DSC. The results of these analyses are given in comparison for both of the samples cooled in near-equilibrium (annealed) and non-equilibrium (as-prepared) conditions. The main crystalline phases appearing in the XRD pattern of the as-

prepared sample were identified as α-Fe, ZrB2 and Fe_3Zr. Therefore, it can be confirmed that the dark gray phase appearing in Figure 4.3 (c) was the ZrB_2. The study of Xiong et al. [107] showed that the ZrB_2 phase was formed when the equilibrium Fe_2Zr and residual amorphous phase reacted and decomposition of the amorphous phase into was decomposed into α-Fe and Fe_3Zr when the ternay Fe-Zr-B system was crystallized. As the similar phases observed in this study, it was considered that the formation of these phases could be attributed to the reactions taking place among the main constituent elements.

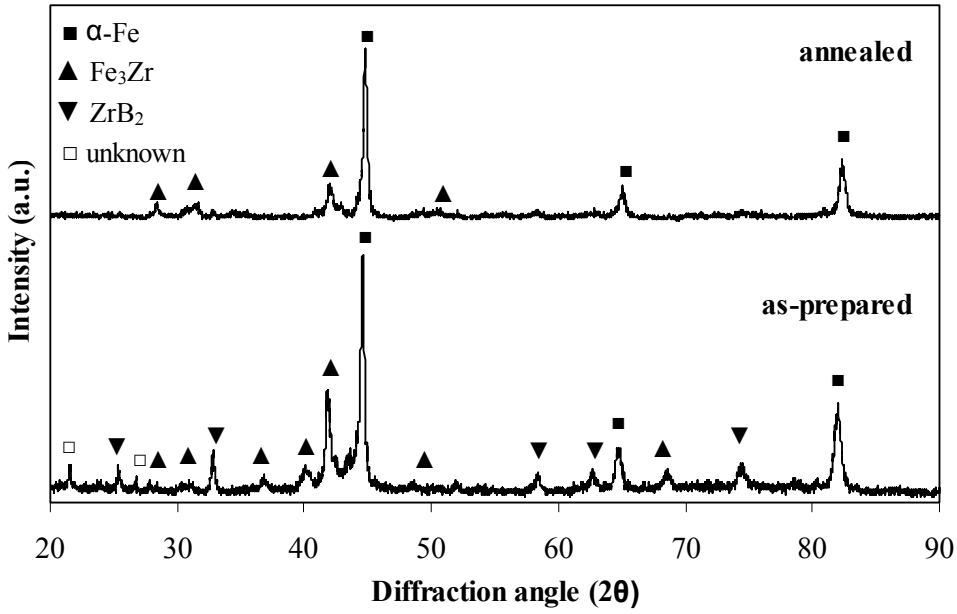

Figure 4.4 The XRD patterns of the master alloy ingot at annealed and as-prepared states.The spectra are shifted for clarity.

The XRD pattern of the annealed sample, on the other hand, contains the same crystalline phases. However, when it is compared to the XRD pattern of the as-prepared master ingot slice, it can be deduced that some peaks belonging to Fe_3Zr had disappeared. This may be due to the uneven distribution of crystalline phases in

the matrix. On the other hand, all of the peaks ZrB_2 phases had disappeared as well as it could not be observed in the microstructure of the annealed sample. This may imply that this phase was a metastable phase formed only in non-equilibrium cooling conditions.

The DSC curves of the samples are shown on the same figure below. Figure 4.5 indicating that both samples melt through two consecutive reactions. Together with the microstructural evidences, these reactions are interpreted as eutectic and peritectic reactions as also observed in the previous study of Akdeniz et al.[6] and Pehlivanoğlu [7]. The data obtained from the DSC plots are presented given in Table 4.1 showing the enthalpy differences and the onset temperatures of the corresponding reactions.

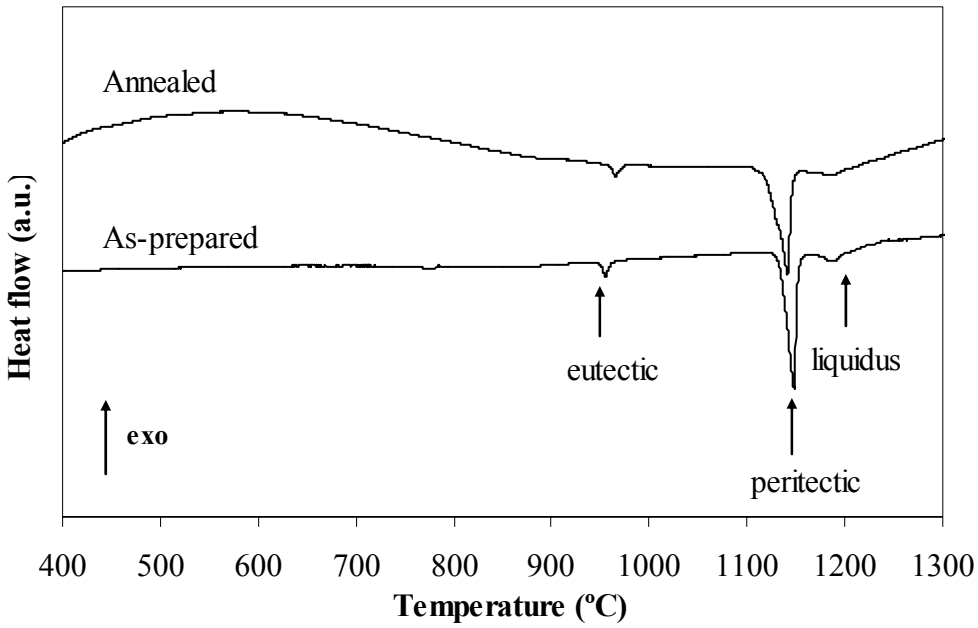

Figure 4.5 DSC heating curve for the master alloy ingot in the as-prepared and annealed states obtained at a scan rate of 20 ºC/min.

Table 4.1 DSC data of the as-prepared and annealed samples

	T_e (ºC)	T_p (ºC)	T_l (ºC)	ΔH_e (J/g)	ΔH_p (J/g)	ΔH_l (J/g)
As-prepared	954.77	1147.94	1216.89	7.42	95.40	12.59
Annealed	965.28	1141.20	1217.04	6.11	72.06	6.82

All of the above results indicated that the non-equilibrium cooling conditions were achieved only in the basal plane of the master alloy ingot slice cooled in the arc-melting device. To further investigate the non-equilibrium structure, a new copper mould was designed in a cylindrical shape whose dimensions are indicated in Figure 3.3 (f). By using this mould, the contact area of the sample which could be cooled more rapidly was increased allowing the study of non-equilibrium microstructure in a larger scale. The cylindrical sample was produced by using pure iron and boron instead of using FeB master alloy. It was then cut into thin slices and a slice taken near the tip of the cylinder was analyzed. A schematic drawing of the slice and its analyzed cross section was shown in Figure 4.6.

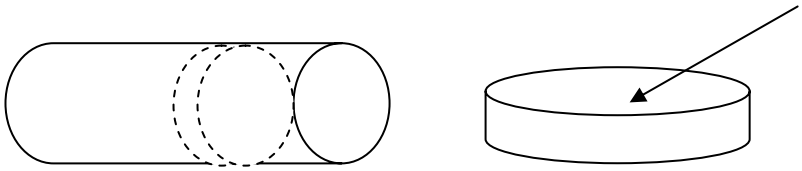

Figure 4.6 Schematic drawing of the cylindrical sample and its analyzed cross section

By the SEM analysis of this sample, an essentially amorphous matrix with small crystalline phases embedded was observed in its microstructure. As can be deduced from the micrographs presented in Figure 4.7, the eutectic reaction had been bypassed but grains of α-Fe can be clearly seen. Figure 4.7 (a) shows the microstructure of the outer surface, which was the more rapidly cooled region since

the specimen was touching the surface of the cylindrical mould at this region. On the other hand, the microstructure of the more slowly cooled inner region still showed no evidence of the eutectic structure but the α-Fe grains were larger as presented in Figure 4.7 (b).

The XRD pattern of the slice cut from the cylindrical sample is given in Figure 4.8. The intensities of the peaks were very small as compared to those of as-prepared master alloy. The weaker intensities may confirm the existence of the amorphous matrix with small crystallites present embedded in it.

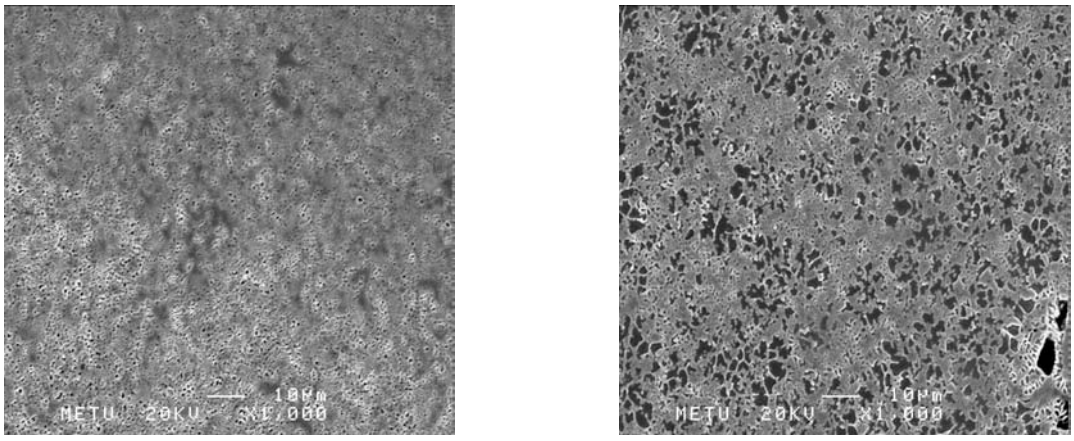

(a) (b)

Figure 4.7 The SE images of the (a) outer and (b) inner regions of the cylindrical sample magnified 1000 times to the actual sizes.

The solidification behaviour of the cylindrical sample was seemed to be similar with those of the master alloy ingot cooled in non-equilibrium cooling conditions since both sample involved the suppression of the eutectic reaction. However, the appearance and sizes of the α-Fe crystallites was different. The grains became finer and amorphous phase fraction increased indicating that a higher cooling rate was

achieved when the alloy was cast into the cylindrical mould. In addition, since the pure iron and boron were used, impurities coming from the FeB master alloy, of which composition is given in Table 3.1, were avoided. If these impurities are regarded as the potential nucleation sites, then finer microstructures can be expected in the case of using pure constituents.

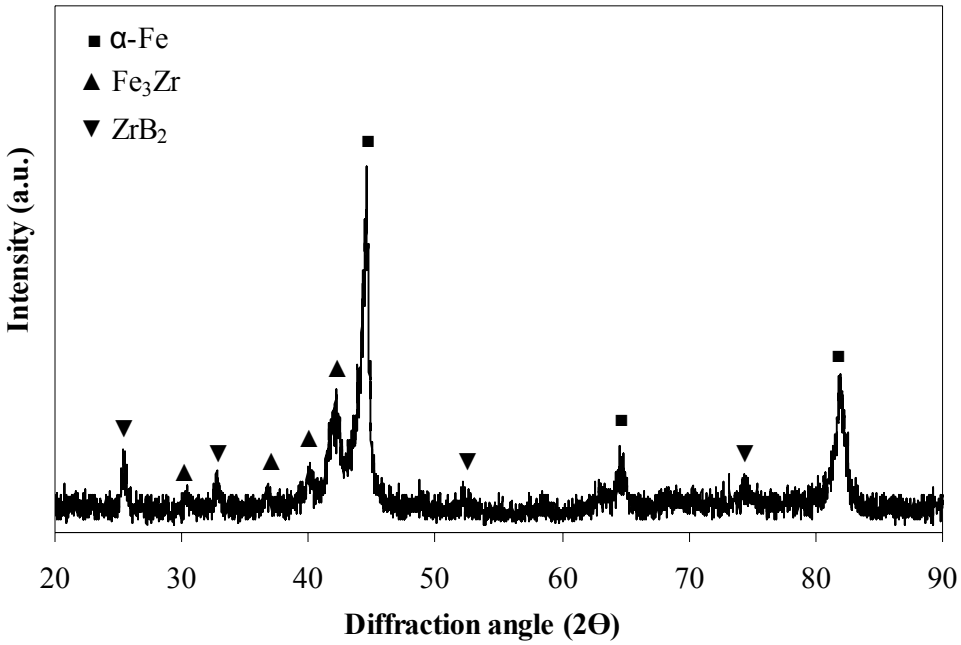

Figure 4.8 The SE images of the (a) outer and (b) inner regions of the cylindrical sample magnified 1000 times to the actual sizes.

The thermal analysis of the cylindrical sample provided a further insight to the reactions taking place in the solidification sequence of the alloy. Figure 4.9 shows the DSC trace of the sample. The glass transition could not be detected but small exothermic peaks observed at some temperatures Therefore, it can be stated that the structure is essentially amorphous but it contains crystalline phases embedded in it causing the unresolved glass transition in the DSC curve. The thermal analysis results are tabulated in Table 4.2.

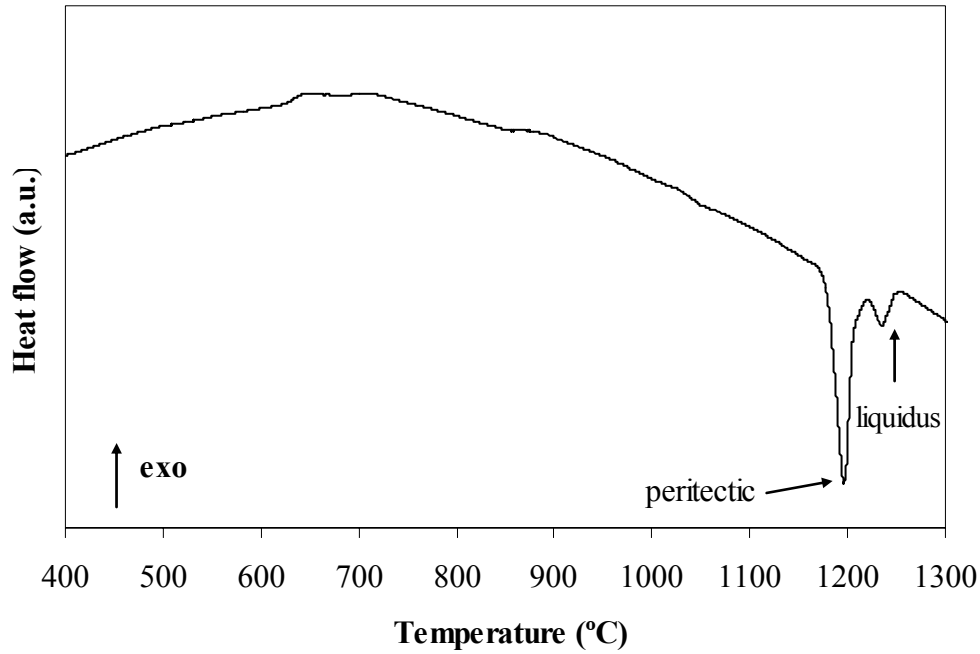

Figure 4.9 The DSC trace of cylindrical sample scanned at a rate of 20 ºC/min.

Table 4.2 DSC data of the cylindrical sample.

	T_e (ºC)	T_p (ºC)	T_l (ºC)	ΔH_e (J/g)	ΔH_p (J/g)	ΔH_l (J/g)
Cylindrical sample	Not available	1195.92	1257.85	Not available	65.87	8.42

4.2 BULK METALLIC GLASS FORMATION

After having examined the solidification behaviour of master alloy ingot in near-equilibrium and non-equilibrium conditions, the rapid solidification

$Fe_{60}Co_8Mo_5Zr_{10}W_2B_{15}$ alloy was performed in order to get a precise knowledge about the rapid solidification microstructures of the alloy. Two methods were applied to obtain bulk amorphous alloy, one involved quenching from the liquid state and the other from the semisolid state.

4.2.1 Quenching from the Liquid State

Bulk metallic glass formation was achieved by quenching the melted alloy into the different copper moulds having different cavities shown in Figure 3.3 (a)-(e). First sample was prepared by using commercially available FeB alloy and induction heating method described in Section 3.1.2. It was cast into the copper mould which is shown in Figure 3.3 (a) with an inner cavity presented in (b). Since the cooling rates were varied along the thickness of the wedge shaped geometry, the solidification behaviour of the sample differed from tip to the end of the wedge. The thinner part of the specimen was cooled rapidly than the base of the wedge. The XRD pattern of this part is given in Figure 4.10 showing a diffuse halo peak and no diffraction peaks indicating the presence of an amorphous phase without any crystalline phases. The SEM micrograph of this part can be seen in Figure 4.11 (a) showing a featureless matrix, which is evident of the achievement amorphous structure.

Figure 4.11 (b) displays the existence of small crystallites in the thick part of the wedge shaped sample. If the XRD pattern of this part given in Figure 4.10 is evaluated by considering the compositional analyses of the dark, gray and bright contrasted phases and the SEM images, it can be concluded that the bright contrasted phase in BSE image is the α-Fe and the gray contrasted phase an unknown compound. Although there was no evidence of a ternary compound in the XRD pattern, the compositional analysis and BSE image could be interpreted that the dark contrasted phase could be a ternary FeZrB compound.

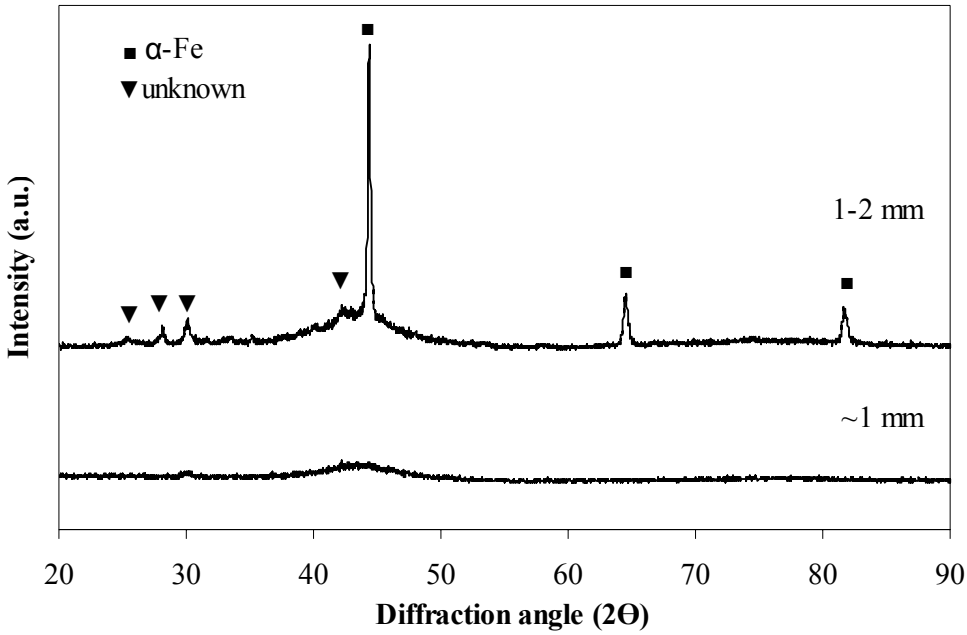

Figure 4.10 XRD patterns of the thin part having a diffuse halo peak and thick part exhibiting some crystalline peaks.

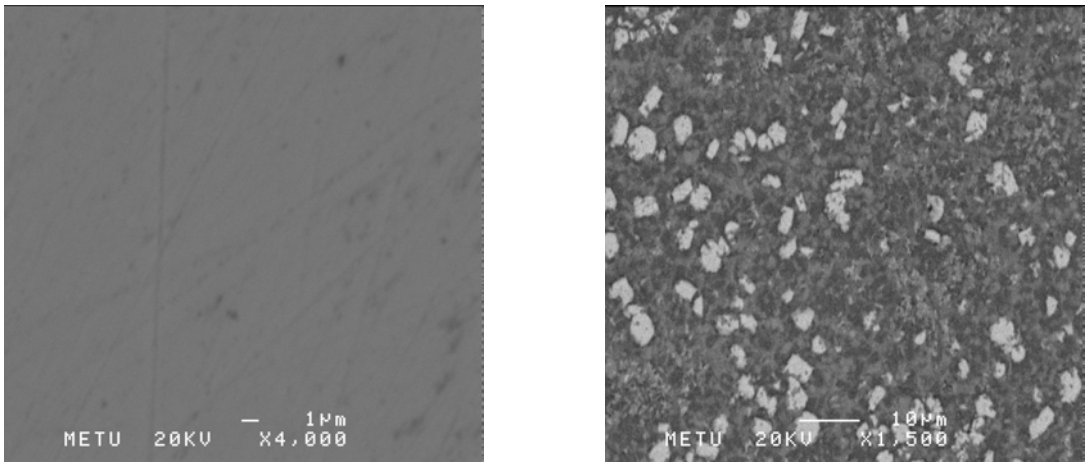

(a) (b)

Figure 4.11 (a) Secondary electron image of thin part showing a featureless matrix, (b) back scattered electron image of thick part of the sample produced b using FeB master alloy and induction heating method.

The amorphous nature of the sample was further confirmed by thermal analysis. DSC trace of the sample given in Figure 4.12 exhibits a typical glass transition and crystallization events. The glass transition temperature was found to be 602.84 ºC and that of the first crystallization to be 648.90 ºC implying that the alloy has a wide supercooled liquid region. Another feature observed in DSC curve is that there are three exothermic peaks. If they are interpreted as crystallization peaks, which will be discussed in the next sections, then the alloy is said to be crystallized in multiple stages and as stated by Inoue et al. [98] this can induce the formation of nanocrystalline phases embedded in the amorphous matrix. The sequence of melting events seen in Figure 4.12 was interpreted as eutectic and peritectic reactions based on the previous observations [6, 7].

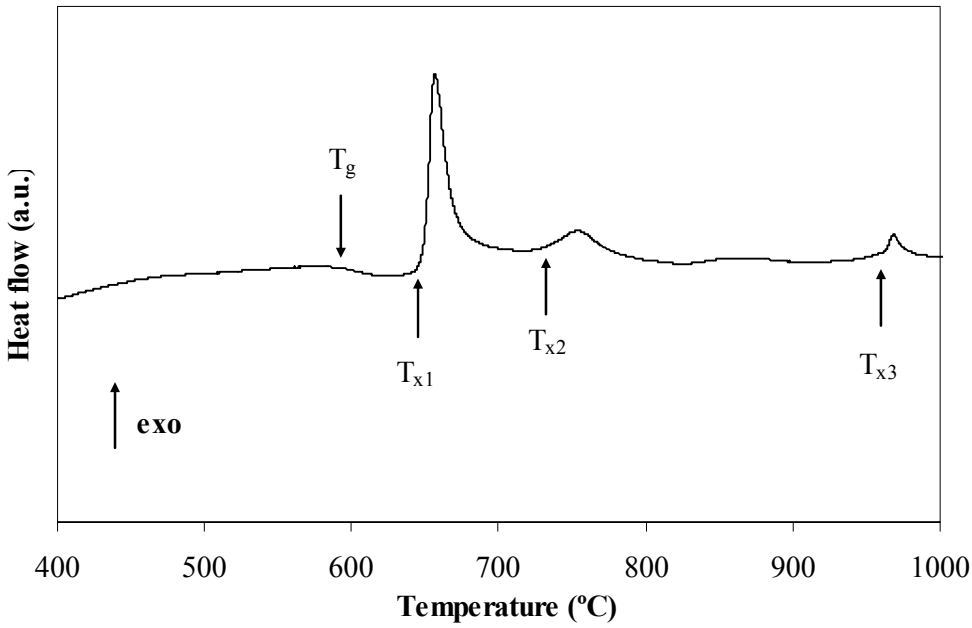

Figure 4.12 DSC trace of the sample prepared by using FeB master alloy and induction heating method scanned at a rate of 20 ºC/min showing glass transition, crystallization and invariant reactions on heating

The next sample was prepared by using FeB master alloy, but different from the previous one, arc melting method was applied. The copper mould with a wedge shape cavity presented in Figure 3.3 (b) and (c) was utilized. The as-cast sample was sectioned perpendicular to the centre line using a diamond saw. Three parts were obtained with different thicknesses as schematically shown in Figure 4.13. The section near the tip was labelled as (a), near the base as (c) and in between as (b). The thickness of the section (a) varies between 0.5-1.2 mm, (b) 1.2-2.4 mm, and (c) 2.4-3.05 mm.

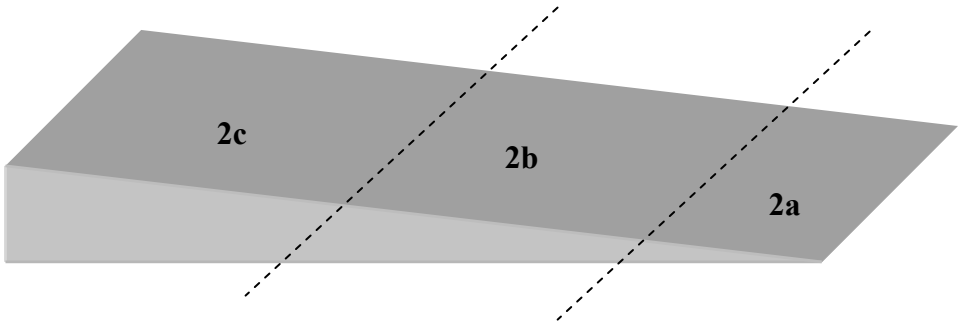

Figure 4.13 Schematic drawing of the wedge shaped sample. Dashed lines show the axes used in sectioning.

The diffraction patterns obtained at various thicknesses are given in Figure 4.14. Near the tip of the wedge, where the cooling rate was highest, the sample is completely amorphous as determined from the x-ray diffraction and SEM analysis. The representative SEM images of the three sections are given in Figure 4.15. The featureless image presented in Figure 4.15 (a) confirms the XRD pattern of the section (a). However, some crystalline peaks started appear as the section thickness increased which is evident also from Figure 4.15. It can be seen that the α-Fe crystallites appearing in Figure 4.15 (b) becomes larger in the form of dendrites embedded in the amorphous matrix presented in Figure 4.15 (c).

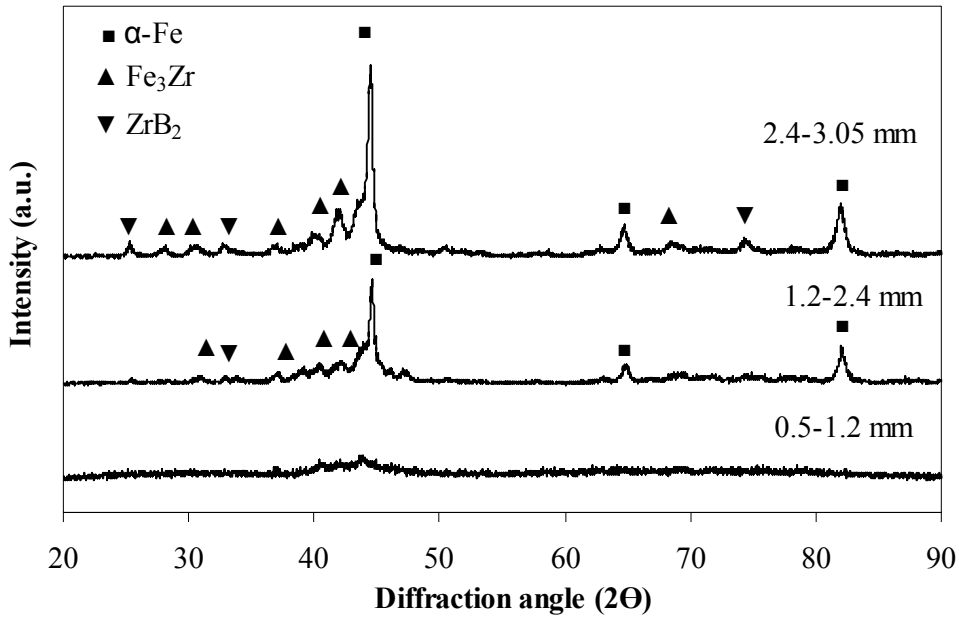

Figure 4.14 XRD patterns of wedge shaped sections a, b, and c indicated by the corresponding thicknesses.

No evidence of eutectic structure could be observed any of the sections indicating that the amorphous phase was obtained even in thick portions of the sample. As compared to the previous sample, it was noted that the microstructure become finer. In addition, intensities of the crystalline peaks were observed to be much weaker than those of the previous sample. Therefore, a conclusion arises such that the arc melting method promotes the formation of the amorphous phase since it provides more homogenous alloy preparation conditions.

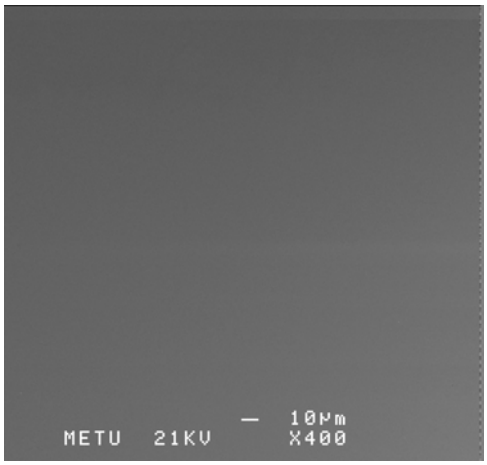

(a)

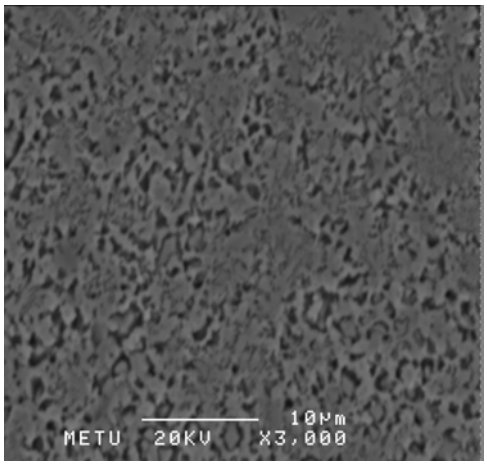

(b)

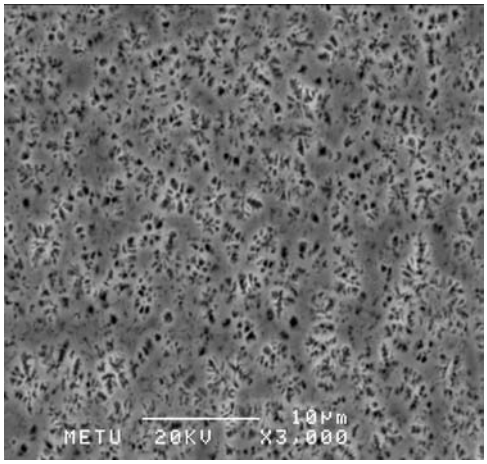

(c)

Figure 4.15 Secondary electron images of (a) sections (a) showing a featureless image, (b) section (b) with α-Fe trying to grow in the amorphous matrix, and (c) section (c). Dendritic features of α-Fe were observed to increase in size.

Although the SEM micrographs did not reveal the existence of any other phases, EDS analysis showed that the Zr content of section (c) was greater than that of the section (a). This may be attributed to the existence of Fe_3Zr compound identified by X-ray diffraction analysis. In addition, Zr content can be said to increase the crystalline fraction and therefore decrease the glass forming ability of the alloy.

The DSC pattern taken from the tip of the wedge cast specimen confirmed its amorphous nature as can be seen in Figure 4.16 .The characteristic DSC trace exhibiting glass transition and crystallization was observed and had little discrepancies from the trace of the previously formed sample, which is presented in Figure 4.12. The second exothermic peak might have been disappeared or the first and the second crystallization peaks overlapped in Figure 4.16. The disappearance of the peak may imply that formation of one of the crystalline phases was avoided. This point can also support the previous statement that the alloy preparation conditions was improved by applying the arc melting method since the impurities, which may act as heterogeneous nucleation sites during the crystallization of the sample, were avoided when the samples were prepared by the arc melting method

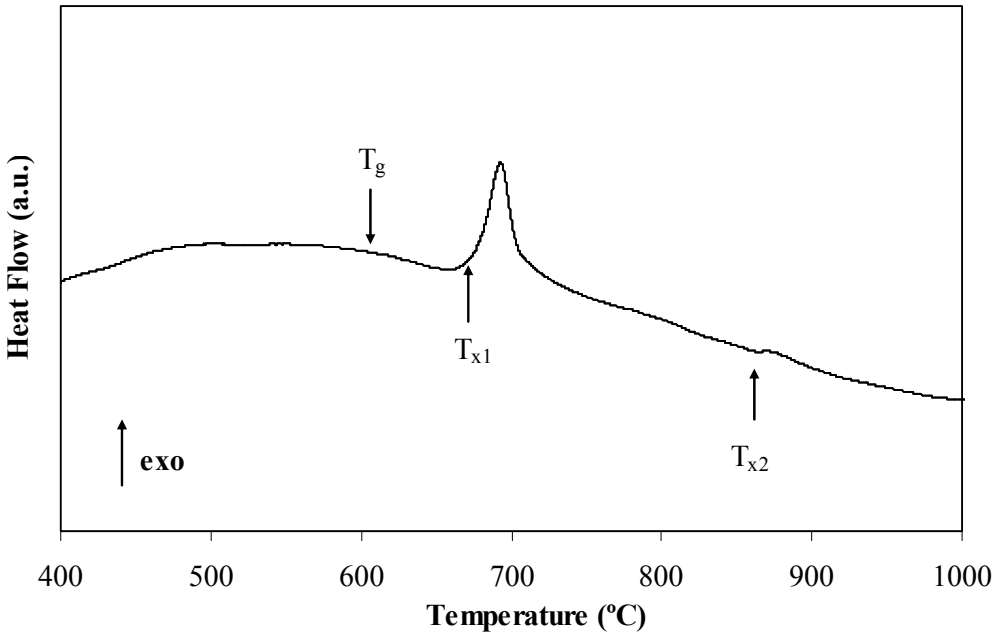

Figure 4.16 DSC pattern of amorphous section of the sample prepared by using FeB master alloy and arc melting method. Glass transition and crystallization reactions can be observed. Scanning rate was 20 ºC/min.

The aim of producing one more sample was to see the effect of using pure iron and boron as the starting material instead of using the FeB master alloy. The alloy was cast into the copper mould presented in Figure 3.3 (a) with an inner wedge-shaped cavity shown in Figure 3.3 (b). The thickness of the amorphous phase was increased by a considerable amount. The amorphous phase was observed at almost all regions as observed in the SEM micrographs. The peaks appearing in the XRD pattern of this sample were very weak as compared to the previously produced sample which is shown in Figure 4.17. This feature implies that there may exist nanoscale phases which could not be resolved by the SEM.

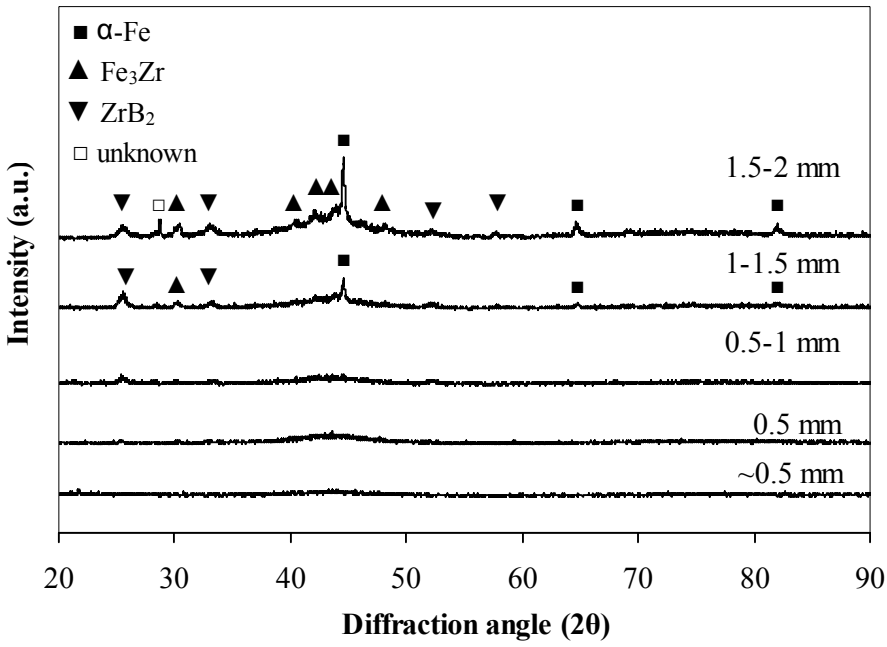

Figure 4.17 XRD patterns of the different section of the sample prepared by using pure constituents and arc melting method.

The diffraction pattern was identified as a characteristic of the amorphous structure up to a thickness of 1 mm. The weak crystalline peaks with a diffuse background were observed, on the other hand, up to a thickness of 2 mm indicating that the

amorphous structure with very small crystalline phases existed in the microstructure. Further confirmation of the presence of the amorphous phase was made by thermal analysis. The DSC curve of the sample is given in Figure 4.18.

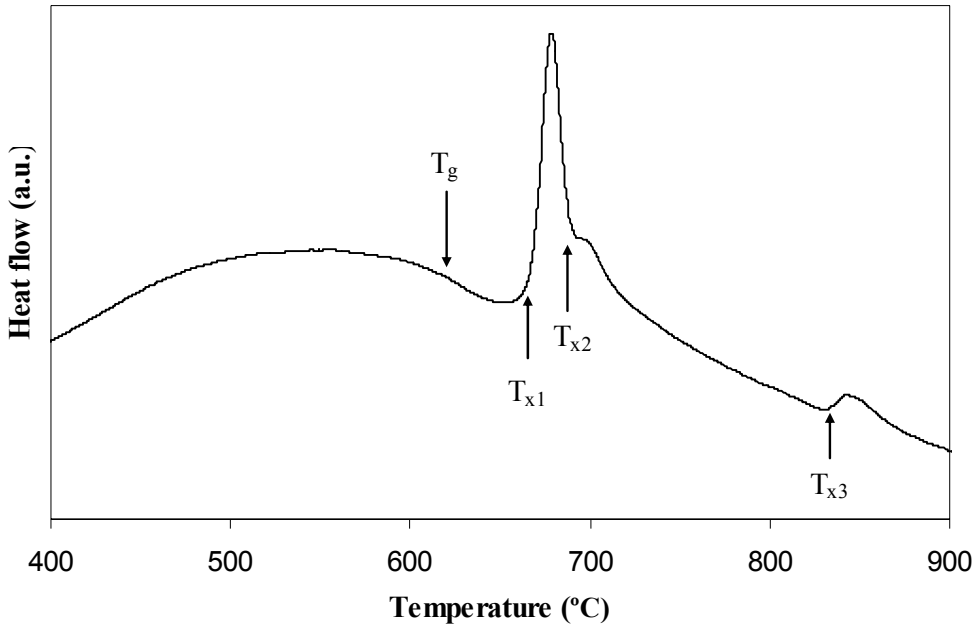

Figure 4.18 DSC pattern of amorphous section of the sample prepared by using pure constituents and arc melting method. Glass transition and crystallization reactions can be observed. Scanning rate was 20 ºC/min.

The DSC data of the three bulk amorphous samples is presented in Table 4.3 to be able to make a comparison in terms of their characteristic temperatures and reaction enthalpies. It was evident from Table 4.3 that the first crystallization temperature shifted to higher temperatures.

Some glass forming ability criteria was calculated and shown also in Table 4.3. The high glass forming ability of the alloy was previously indicated by the results of the other studies [6,7]. The parameters related to the characteristic temperatures were

chosen since a lot of information was made available by performing several DSC experiments. The reduced glass transition temperature (T_{rg}), the width of the supercooled liquid region (ΔT_x), and the γ parameter were selected for further analysis.

If the reduced glass transition temperature is considered in general, the alloy do not exhibit a good glass forming ability since the alloys with T_{rg} greater than 0.67 are considered to be good glass formers. The width of the supercooled liquid region, on the other hand, does not follow this trend. The ΔT_x values of the sample prepared by using pure constituents and arc melting was expected to be larger than that of prepared by using FeB and arc melting , which was indeed expected to be greater than that of prepared by using FeB and induction heating method. Therefore, it is obvious that the T_{rg} and ΔT_x is not very suitable in comparing the relative glass forming abilities obtained in this study. γ parameter obtained for various good glass formers were observed to be larger than 0.362 as mentioned in Section 2.4.2. The γ values presented in Table 4.3 showed that the alloy has a good GFA. The correlation of GFA values for various samples with γ parameter was also observed to reflect the expected tendency.

Table 4.3 DSC data of the bulk amorphous samples together with the caculated T_{rg}, ΔT_x and γ parameters.

Samples	T_g (°C)	T_{x1} (°C)	T_{x2} (°C)	T_{x3} (°C)	ΔH_{x1} (J/g)	ΔH_{x2} (J/g)	ΔH_{x3} (J/g)	T_{rg}	ΔT_x	γ
Sample prepared by using FeB and induction heating	602.84	648.90	728.27	960.92	-65.65	-16.63	-8.24	0.579	46.06	0.386
Sample prepared by using FeB and arc melting	633.24	676.70	-	863.76	-53.82	-	-1.49	0.603	43.46	0.394
Sample prepared by using pure constituents and arc melting	630.08	688.60	693.76	832.72	-37.63	-1.10	-6.09	0.555	38.80	0.394

4.2.2 Quenching from the Semi-solid State

When all the above observations are considered, it is interesting to note that the amorphous phase formation was associated with suppression of eutectic reaction. A hypothetical phase diagram for the alloy in consideration was constructed by Akdeniz et al. [6] which is given in Figure 4.19.

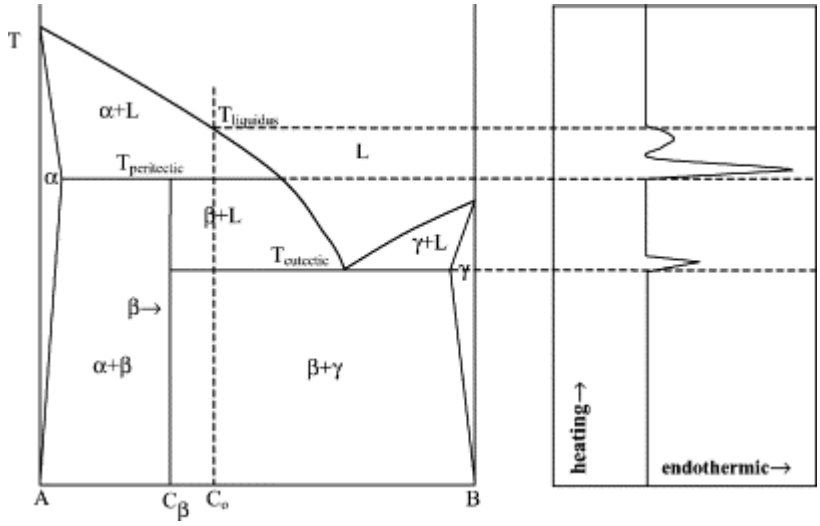

Figure 4.19 Phase diagram and schematic melting DSC curve of a hypothetical binary alloy which melts through a sequence of eutectic and peritectic reactions [6].

They studied the phase transformations taking place during rapid and equilibrium solidifications of $Fe_{60}Co_8Zr_{10}Mo_5W_2B_{15}$ and $Zr_{65}Al_{10}Ni_{10}Cu_{15}$ alloys by establishing a relationship between bulk glass forming ability and type/nature of invariant reactions. They identified that the solidifications of these alloy systems occurs through two consecutive invariant reactions; a high temperature peritectic followed by a eutectic reaction and presented a phase diagram of hypothetical binary alloy system going through same kind of reactions as shown in Figure 4.19. Under near-equilibrium conditions these alloys first enter the two-phase, $l+\alpha$, region leading to the formation of non-faceted primary dendrites. Then, both systems go through a

peritectic reaction where facet forming complex intermetallic phase tends to form on the existing primary dendrite trunk owing to relatively high enthalpy of phase transitions. They further pointed out that the formation of the amorphous structure in these alloys systems can be attributed to the suppression of eutectic transformation and growth competition between stable and metastable eutectic by comparing the rapid and equilibrium solidification microstructures.

As a new attempt in this study, the achievement of amorphous state was attempted by quenching from the semi-solid state. The existence of the semi-solid region, $\beta+l$, between the eutectic and peritectic temperatures in $Fe_{60}Co_8Zr_{10}Mo_5W_2B_{15}$ as established by Akdeniz et al. [6] was considered to be utilized for obtaining amorphous phase without complete melting of the alloy.

A temperature between the eutectic and peritectic temperatures, 1000 ºC, was chosen. The alloy was known to be in semi-solid state at that temperature. The amorphous nature of the samples was confirmed by thermal analysis. DSC curve presented in Figure 4.20 exhibits a typical glass transition and crystallization reactions.

As stated by Majumdar et al. [66] the amount of amorphous phase present in a specimen can be determined by estimating the area under the exothermic peak, which is proportional to the enthalpy of crystallization. If the crystallization enthalpy of the fully amorphous sample corresponds to 100% transformation of the amorphous phase, the fraction of amorphous phase, f, can be calculated from the ratio

$$f = \frac{\Delta H_c}{\Delta H_a} \qquad (4.1)$$

where ΔH_c represents the enthalpy of crystallization for the specimen at a particular condition and ΔH_a is the enthalpy for the fully amorphous alloy. The DSC data and the fractions of amorphous phase and related enthalpies are given in Table 4.4. The

amorphous phase fraction was calculated using the Equation (4.1.). The crystallization enthalpy of the sample prepared by using FeB master alloy and arc melting methods was used since it has two crystallization exotherms similar to the sample quenched from the semi-solid state.

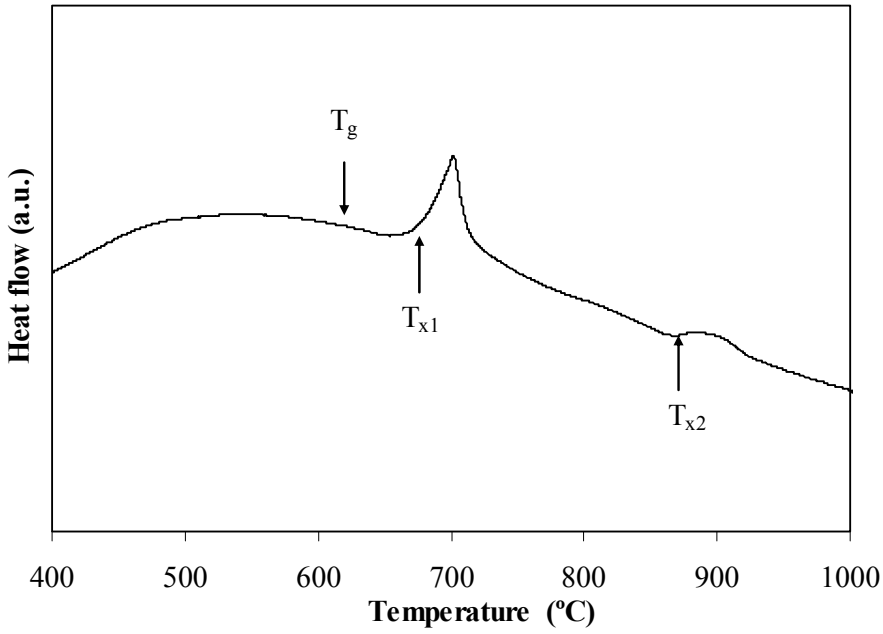

Figure 4.20 DSC trace of the sample quenched from the semi-solid state.

Table 4.4 DSC data of the sample quenched from the semi-solid state and the estimated fraction of amorphous phase

Sample	**T_g (°C)**	**T_x (°C)**	**ΔT_x (°C)**	**Enthalpy (J/g)**	**Fraction of the amorphous phase (%)**
Sample quenched from the semi-solid state	634.99	677.49	39.50	-36.89	68.54
Fully amorphous sample	633.23	676.70	43.44	-53.82	100

The SEM images of the quenched sample are given in Figure 4.21. The dark contrasted phase is α-Fe with a small amount of W revealed by EDS analysis. The gray contrasted phase is predicted to be complex phase containing all the elements constituting the alloy, but it could not be identified by any of the characterization techniques. It was noted that the eutectic reaction was suppressed during the quenching process since micrographs revealed no evidence of eutectic microstructure. The liquid phase presented in the semi-solid state was seemed to be converted to the amorphous phase. This supports the idea of suppressing the eutectic reaction renders the formation of the amorphous phase in this alloy. In addition, amorphous structure without complete melting of the alloy was achieved and this is very important for future applications of the alloy in the sense that the alloy can be kept in its original shape during the amorphous phase formation.

Above results pointed out that the cooling rate applied in the solidification process is very important in the achievement of the amorphous phase since there is a critical cooling rate at which the formation of the eutectic phase is avoided. Therefore, further investigation was needed on the critical cooling rate of the alloy.

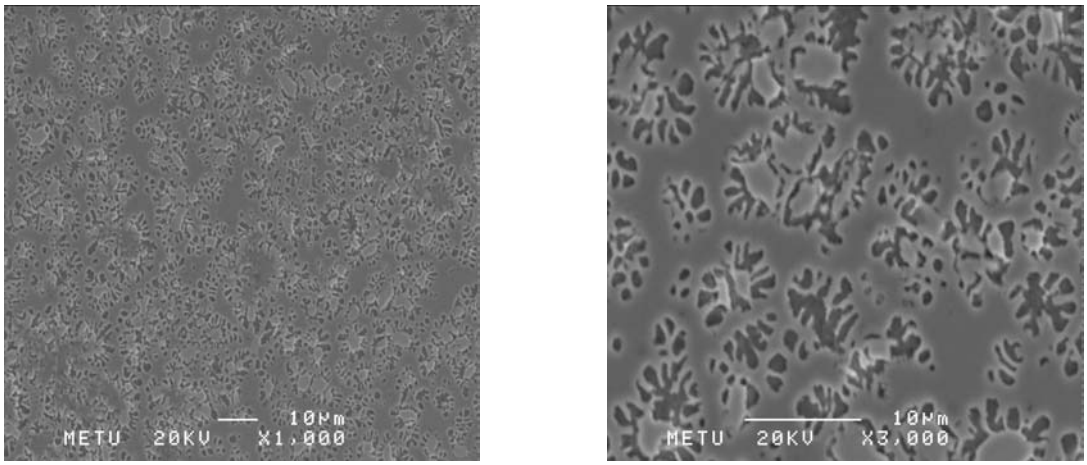

(a) (b)

Figure 4.21. SE images of the quenched sample magnified (a) 1000 times, (b) 3000 times to its actual size.

4.3 EXPERIMENTAL ESTIMATION OF CRITICAL COOLING RATE

The so-called Barandiaran-Colmenero [89] expression (Equation 2.29) was used to estimate the critical cooling rate experimentally. The series of DSC curves at the cooling rates of 40, 50, and 99 ºC/min are presented in Figure 4.22. The plot of lnR versus $(T_l\text{-}T_{xc})^2$, obtained using the data produced as a result of DSC measurements, is shown in Figure 4.23. The critical cooling rate was calculated from the slope of the linear plot as 5.35 K/s with a high regression coefficient. This value is comparable to that of the commercially called Vitreloy 1 alloy having a critical cooling rate of 1.4 K/s, which is one of the best glass formers in metallic systems [108].

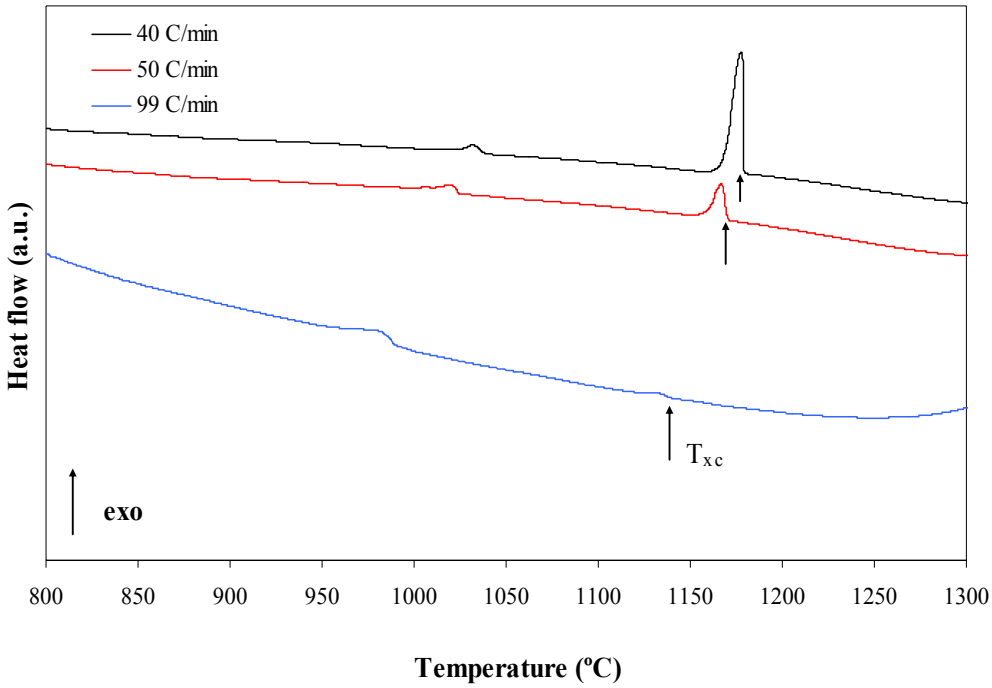

Figure 4.22 DSC cooling curves of $Fe_{60}Co_8Zr_{10}Mo_5W_2B_{15}$ amorphous alloy at various cooling rates.

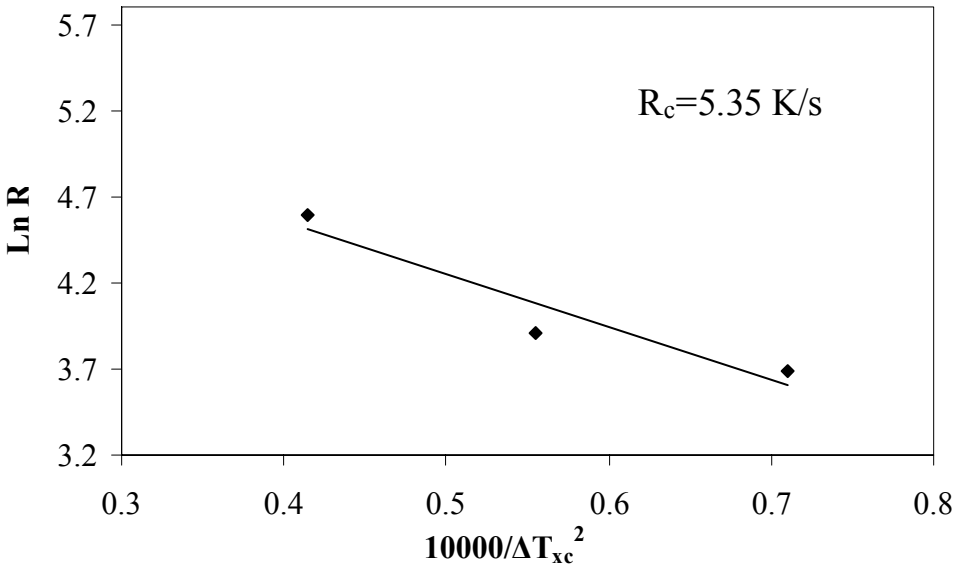

Figure 4.23 The critical cooling rate plot of *ln R* versus $10000/\Delta T_{xc}^{2}$.

The critical cooling rate for the eutectic reaction was calculated using the same procedure and it was determined to be 0.14 K/s as can be seen in Figure 4.24. This low value indicates that the alloy could be made amorphous in large scales easily since the low critical cooling rates are required for bulk production of the metallic glasses.

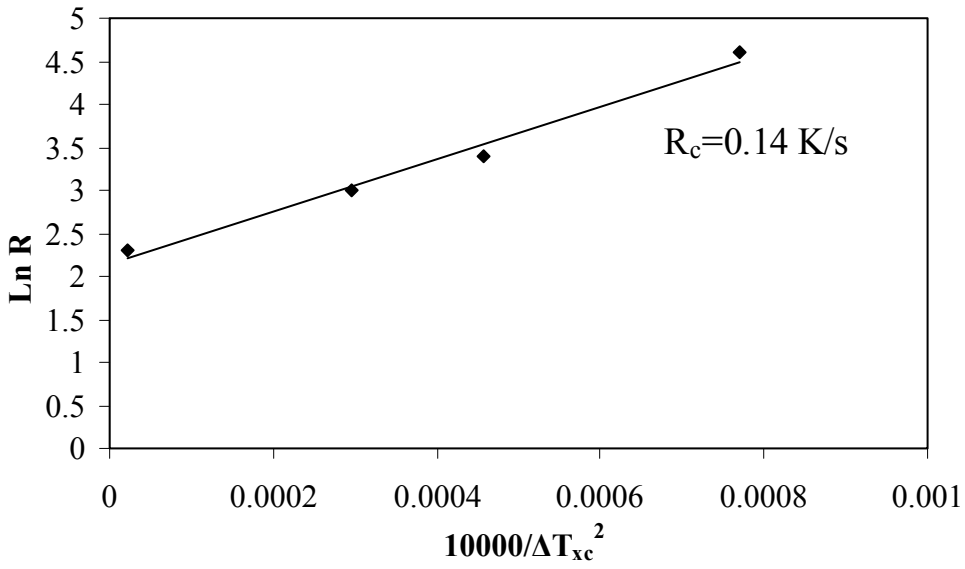

Figure 4.24 The critical cooling rate plot of *ln R* versus $10000/\Delta T_{xc}^2$ for the eutectic reaction.

DSC experiments performed by applying different heating and cooling rates showed valuable information about the solidification and crystallization of $Fe_{60}Co_8Zr_{10}Mo_5W_2B_{15}$ alloy. The first observation made on the DSC scans of master alloy ingot, first and second amorphous samples showed that the enthalpy of the eutectic reaction became more prominent and the peritectic reaction separated itself from the melting event upon re-heating the sample. An example of such behaviour is given in Figure 4.25. Therefore, a series of DSC heating and cooling cycles were performed at different scanning rates in order to study this phenomenon further.

The samples heated from room temperature to a temperature above the melting point were subsequently cooled and reheated. The reheated samples were cooled again in order to analyze reproducibility of the reactions taking place on heating. The heating scans of each heating and cooling cycle are compared. A point that can be easily grabbed from the curves is that the second heating scan contains deeper peaks especially for the eutectic reaction. Also, peritectic reaction became separated from the melting event in the second scan. An explanation to this behaviour of DSC curves can be made as follows: During the first heating scan, the metastable phases which may exist in the as-cast sample might have acted as barriers for nucleation and growth of the eutectic. When the sample was completely melted and held at 1400 ºC for a period of time to ensure homogenization, the next heating scan, therefore, the completion of the eutectic reaction could be achieved.

The overlapping of two DSC peaks, on the other hand, is commonly seen and some peak separation softwares were used to differentiate these peaks. The cyclic experiments have shown that the overlapping peaks became separated as the scanning rate was increased contradictory to the case observed in a study of Smith et al. [109]. They observed that the for low scan rates the crystallization peak was resolved into two components. Table 4.5 shows the data obtained from first and second heating DSC scans. Comparing the enthalpies of eutectic reaction in the first and second heating scans, it can be said that the eutectic reaction, which could not go to completion during the first scan, could proceeded further.

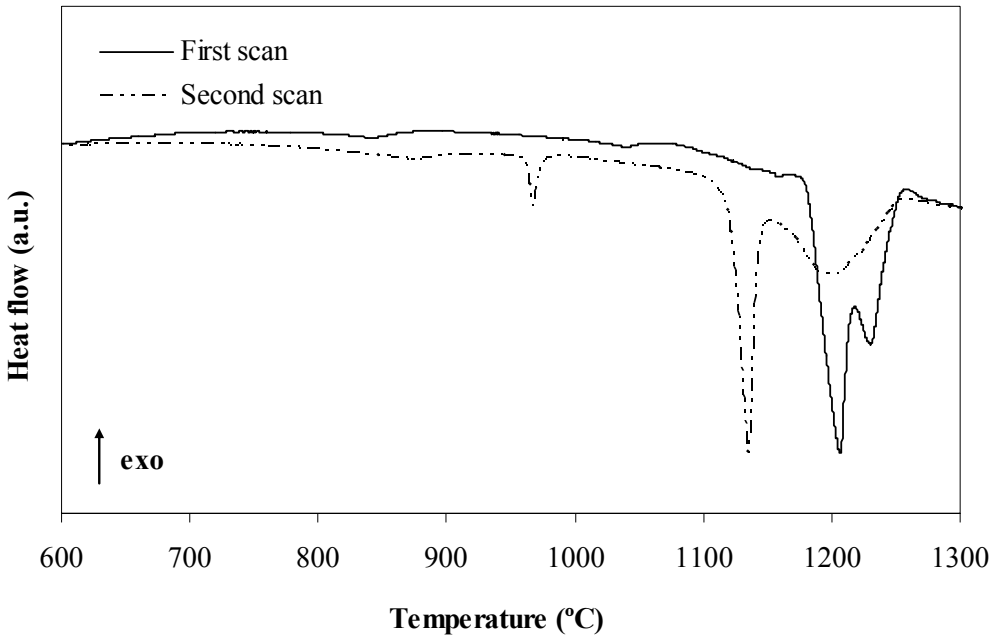

Figure 4.25 First and second heating scans at a rate of 20 ºC/min. The spectra have been shifted for clarity.

Table 4.5 Comparison of reaction enthalpies estimated during the first and second heating scans

Heating rate (ºC/min)	Reaction Enthalpy (J/g)	First scan	Second scan
20	Eutectic	2.35	7.42
	Peritectic	56.97	63.91
	Melting	19.32	64.10
40	Eutectic	1.17	8.47
	Peritectic	0	4.11
	Melting	174.34	176.59
60	Eutectic	3.40	8.93
	Peritectic	0.72	11.45
	Melting	199.96	163.74
80	Eutectic	6.44	9.98
	Peritectic	0.82	1.53
	Melting	207.18	223.70
99	Eutectic	3.28	5.34
	Peritectic	0	7.40
	Melting	158.03	97.22

4.4 CRYSTALLIZATION KINETICS

As the opposite events occur simultaneously in nature, glass formation and crystallization are two processes that take place competitively. So far from the beginning of the study the glass formation was investigated and from this point, the transformations taking place under the thermal treatment of the alloy and the nature of crystalline phases appearing in the resultant microstructures will be discussed. In order to clarify the crystallization behaviour of amorphous $Fe_{60}Co_8Zr_{10}Mo_5W_2B_{15}$ alloy, various experimental and analytical methods were used

In order to investigate the crystallized phases of the amorphous alloy and obtain an interpretation of the observed peaks in DSC scans of the amorphous samples, the isothermal annealing experiments were performed.

Two representative wedge-shaped amorphous samples were annealed in the furnace at two temperatures, 650 ºC and 750 ºC, chosen in the supercooled liquid region and above the first crystallization temperature respectively. The annealing time was selected as 5 hours according to the studies on the crystallization of similar alloys [110,111].

The DSC traces of the samples were given in Figure 4.26. The sample annealed at 650 ºC exhibits the glass transition and crystallization events characteristic of the amorphous phase. This immediately implies that the amorphous phase is stable even after the long time anneals in the supercooled liquid state. Similarly, the sample annealed at a temperature above the supercooled liquid region, 750 ºC, was subjected to characterization in order to see the differences. (b)

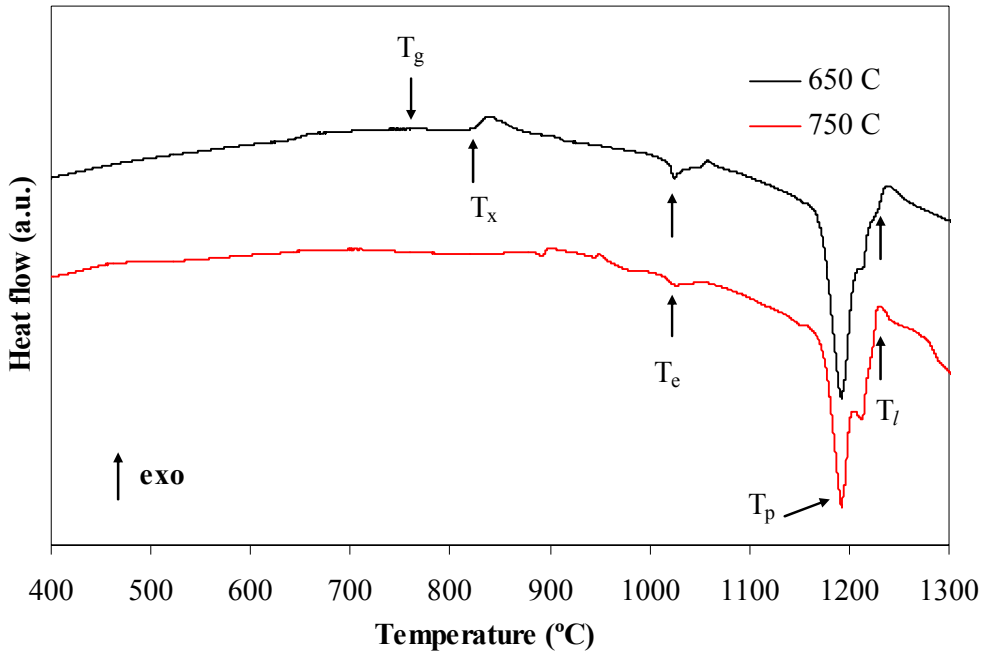

Figure 4.26 The DSC trace of the amorphous sample isothermally heated at 650 and 750 ºC for 5 hours in the furnace. Scanning rate was 20 ºC/min.

The resultant microstructures were investigated by using the SEM to observe whether any crystalline phases had precipitated. The micrograph of the sample annealed at 650 ºC is given in Figure 4.27 showing almost featureless matrix even when magnified 10000 times to its actual size.

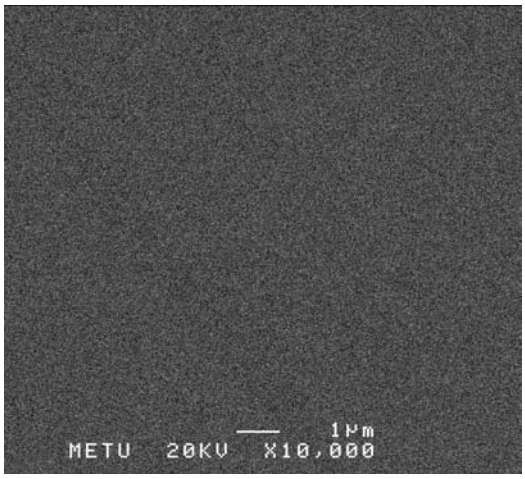

Figure 4.27 The SEM micrograph of the amorphous sample annealed at 650 ºC for 5 hours in the furnace.

Then the XRD pattern given in Figure 4.28 was analyzed to see if any phases present which could not be resolved by using the SEM. It is evident from Figure 4.28 that only weak α-Fe peaks are present in the diffractogramme. Applying the Scherer's formula to the α-Fe peak, the size of the iron crystallites were estimated to be approximately 0.05 nm which could not be observed by using the SEM.

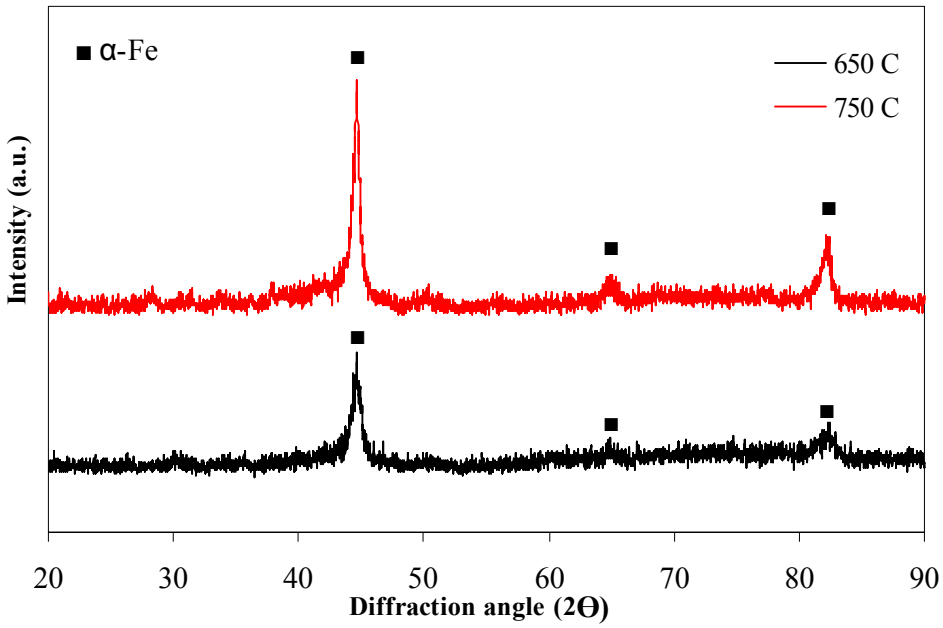

Figure 4.28 XRD patterns of amorphous samples annealed at 650 and 750 ºC for 5 hours in the furnace showing a diffuse background with weak α-Fe peaks.

The sample annealed at 750 ºC, on the other hand, showed some microstructural features in its SEM images given in Figure 4.29. However, XRD analysis revealed no phases other than the α-Fe peaks having stronger intensities than the peaks appeared in the diffractogramme of the sample annealed at 650 ºC. Application of the Scherer's formula to the peaks, this time resulted in the estimation of larger particle sizes of approximately 130.28 nm. Therefore, the exact identification of the crystallization products could not be achieved, but careful examination of EDS analysis results indicated that the redistribution of Zr atoms between the amorphous matrix and the crystallized phases occurred during the heat treatment procedure. The Zr content increased in the spherical grains observed in Figure 4.29 indicating that it might have caused the nucleation of these grains in the amorphous matrix. However, to make precise comments on the crystallized phases is not very possible at this stage. The further studies by using high resolution transmission electron microscopy may reveal the exact nature of the crystallized phases.

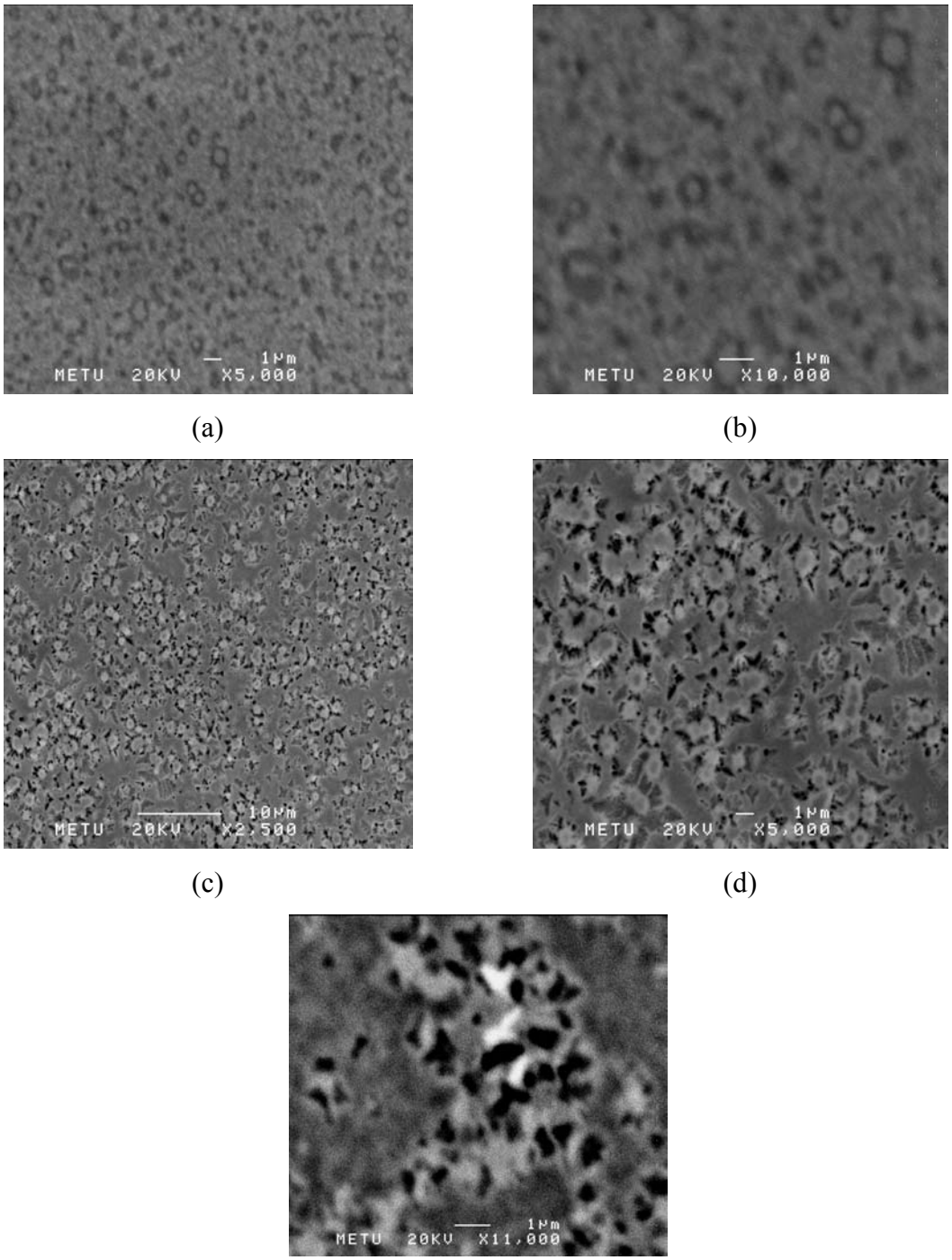

(a) (b)

(c) (d)

(e)

Figure 4.29 The SEM micrographs of the amorphous sample isothermally heated at 750 ºC. (a) SE image of the thinnest part of the specimen, (b) magnified 10000 times, (c) SE image of the thick part, (d) closer view of (c), and (e) BSE image of a small region in (b) magnified 11000 times**.**

The heat treatment procedure applied in isothermal annealing experiments was applied in the DSC to see any crystallization event would take place during the 5 hour annealing time. The annealing temperatures were also the same. First isothermal scan at 650 ºC revealed a small peak after 1000 seconds past from the start of the experiment as shown in Figure 4.30. This was thought to be due to two possibilities: either an early crystallization reaction or just the enthalpy relaxation could have occurred. Therefore, it was decided to repeat the 5 hour period to the same sample. The same trace obtained and the first possibility of observing crystallization was eliminated.

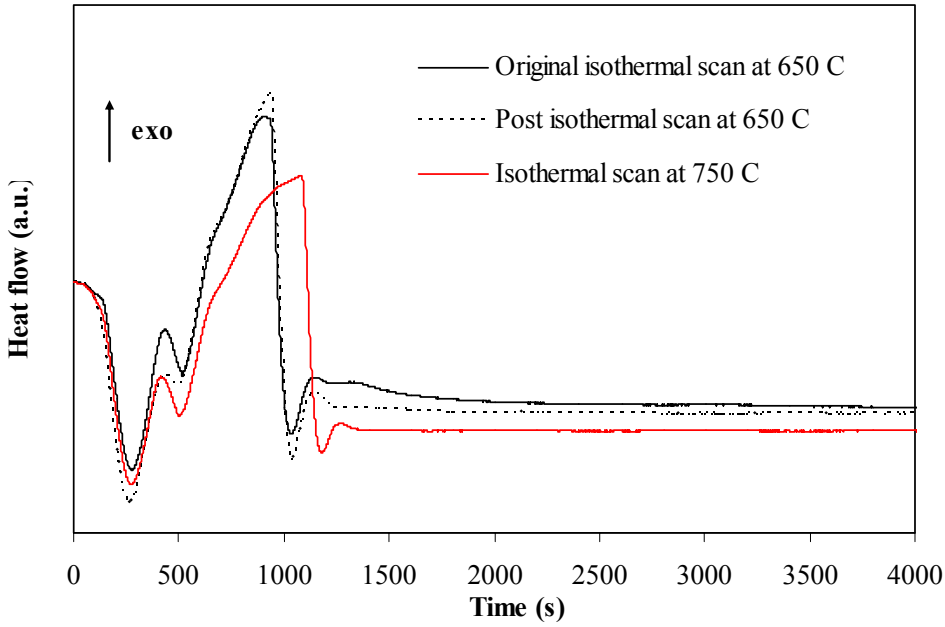

Figure 4.30 Isothermal DSC scans of the amorphous samples at 650 and 750 ºC for 5 hours. The dashed line shows the second scan performed for the identification of the peak appearing at around 1100 seconds.

The isothermal annealing of master ingot piece was performed to see whether the same enthalpic recovery. Since the master alloy ingot was not amorphous, no

exothermic peaks were expected. The resultant DSC trace is given in Figure 4.31. showing the same peak observed at around 500 seconds in Figure 4.30. This may support the existence of relaxation of the amorphous phase before crystallization occurred in above DSC trace. The relaxation signal could have occurred but to make an exact identification, a more detailed DSC procedures including several DSC scans with pre-annealing treatments should be applied which is the beyond the time limits of this study. The further works would clarify this behaviour.

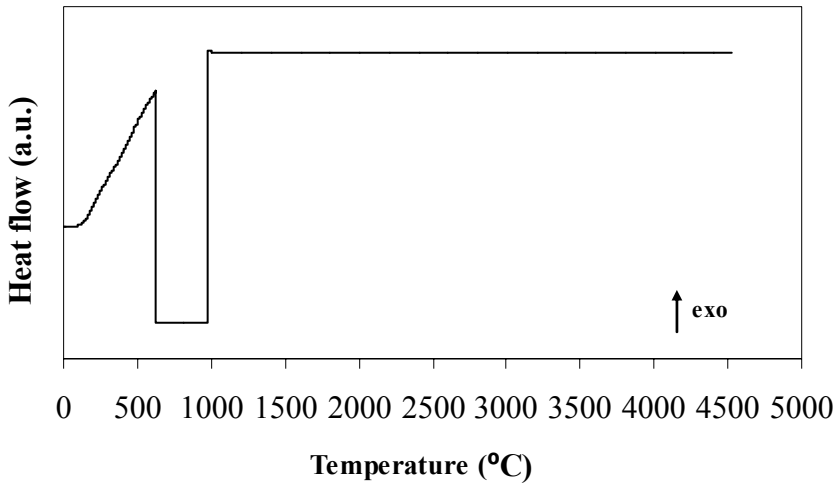

Figure 4.31 Isothermal DSC scan of the master alloy ingot piece at 650 for 5 hours.

Therefore, the JMAK analysis could not be performed on any of the chosen temperatures since the crystallization peaks could not be detected in the 5 hour period of time. In the study of Hu et al. [111] on the crystallization kinetics of the similar alloy, they used much shorter times and observed the crystallization peaks. This may be attributed to the high stability of the alloy under investigation against crystallization than the one produced by Hu et al [111].

Further investigation on the crystallization kinetics of the alloy was made by using analytical methods to calculate the activation energies. A series of non-isothermal DSC scans were performed at different heating rates. The resultant DSC scans are presented in Figures 4.32.

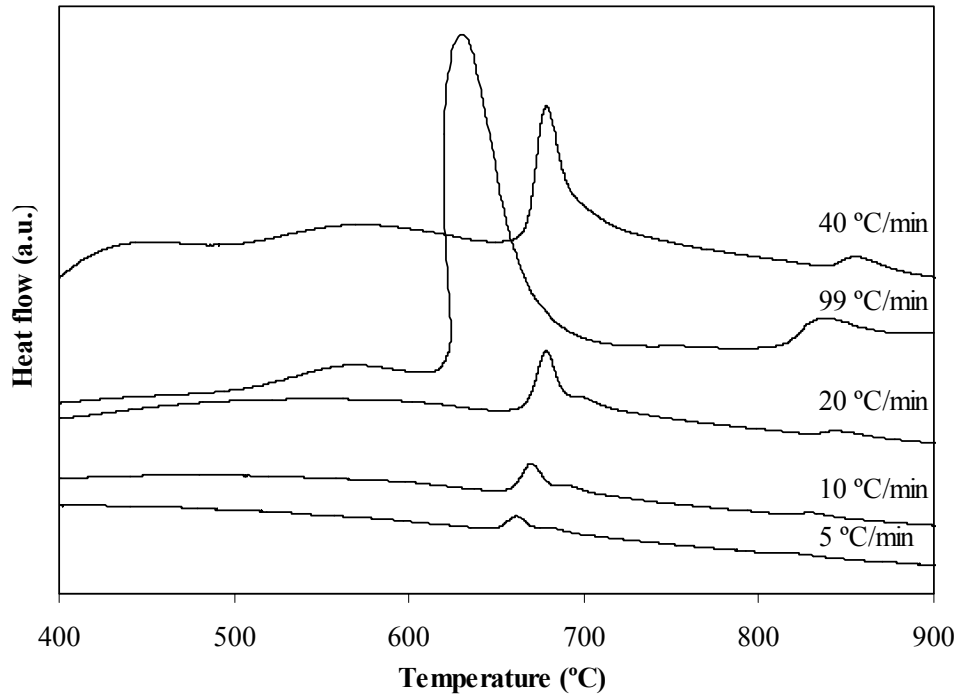

Figure 4.32 The continuous heating curves at scanning rates of 5 to 99 ºC/min.

The glass transition, T_g, and three exothermic peaks were observed at the lowest scanning rate. As the scanning rate was increased, the number of exothermic peaks decreased to two, which may indicate that the reaction taking place at the second exotherm was sensitive to high heating rates. When the material was heated more rapidly, the atoms could not have enough time to rearrange for this second reaction. Another possibility is that the second exotherm could not have been resolved due to the instrumental ineffectiveness at high scanning rates. On the other hand, it can be

deduced that the heat release time is longer in low scanning rates which causes the exothermic peak intensity to decrease. This was the case for the alloy in consideration as can be observed from the above figures. At the low scanning rates, the intensity of the main crystallization peak decreased. The first exotherm, which is seen at all scanning rates, was considered to be due to the crystallization of the amorphous phase. In a study of Pawlik et al. [112] on a similar $Fe_{61}Co_7Zr_{10}Mo_5W_2B_{15}$ alloy; the first, second and third exothermic transitions were identified as first, second and third crystallization reactions. On the other hand, Liu et al. [110] studied the same $Fe_{60}Co_8Zr_{10}Mo_5W_2B_{15}$ alloy system and observed only one exothermic peak in the DSC curve, which they attributed to the crystallization of the amorphous phase.

In addition to above observations on the exothermic peaks, the trend in temperatures corresponding to these peaks was also observed. The shift in peak temperatures to higher values with the increasing scanning rate can be seen from the figures. However, this trend was not followed at high rates such as 40 and 99 °C/min. The transition temperatures were plotted against the scanning rate as shown in Figure 4.33. The glass transition temperature and the three exothermic peak temperatures were observed to increase with the increasing scanning rate if the temperature for the highest scanning rate was ignored.

The analytical Kissenger and Ozawa methods utilize the shift in peak temperatures. These methods were applied to relate the transition temperatures to the heating rate and find the activation energies for each of the transitions corresponding to each peak temperatures.

The Kissinger method [75] is based on the Equation (2.20). The plot of $\ln(\beta/T_p^2)$ versus $1/T_p$ is a straight line with a slope giving the activation energy. The transition temperatures for all scanning rates were used at the beginning. The initial plots did not follow the expected trend.

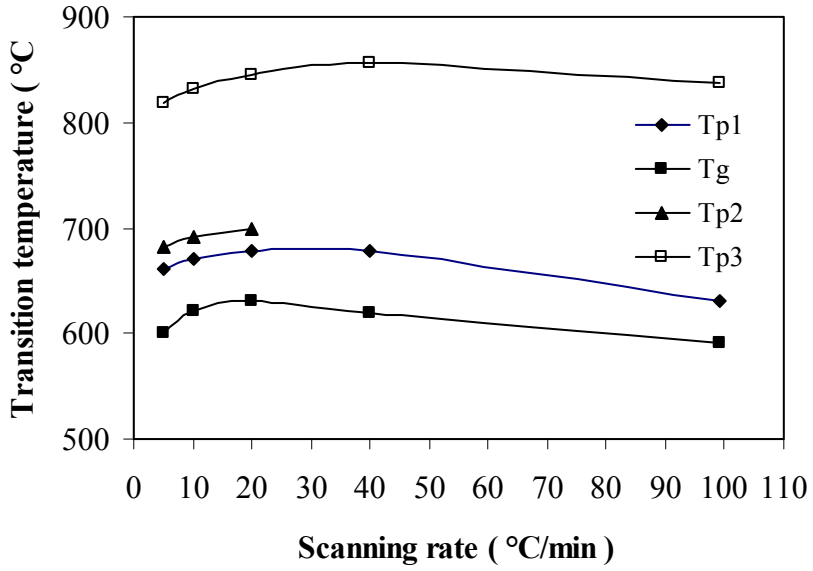

Figure 4.33 Dependence of transition temperatures on the scanning rate determined from the DSC experiment.

It was observed that at high scanning rates some low temperature peaks deviated from the Kissinger behaviour due to insensitivity of the DSC thermocouple in recording at temperatures. Therefore these peaks were omitted and the Kissinger analysis re-applied to find more results. However, when the data obtained from both 40 and 99 °C/min was omitted, all the transition temperatures correlated better with the scanning rates as shown in Figure 4.34. E_g, E_{c1}, E_{c2}, and E_{c3} represents the activation energies for glass transition; first, second and third exothermic reactions respectively. Then the activation energies were estimated from the slope of the straight lines obtained from the plots and listed in Table 4.6. The activation energy for the first crystallization reaction was comparable with that found in a study of Liu et al [110] reporting the activation energy as 559.9 kJ/mol.

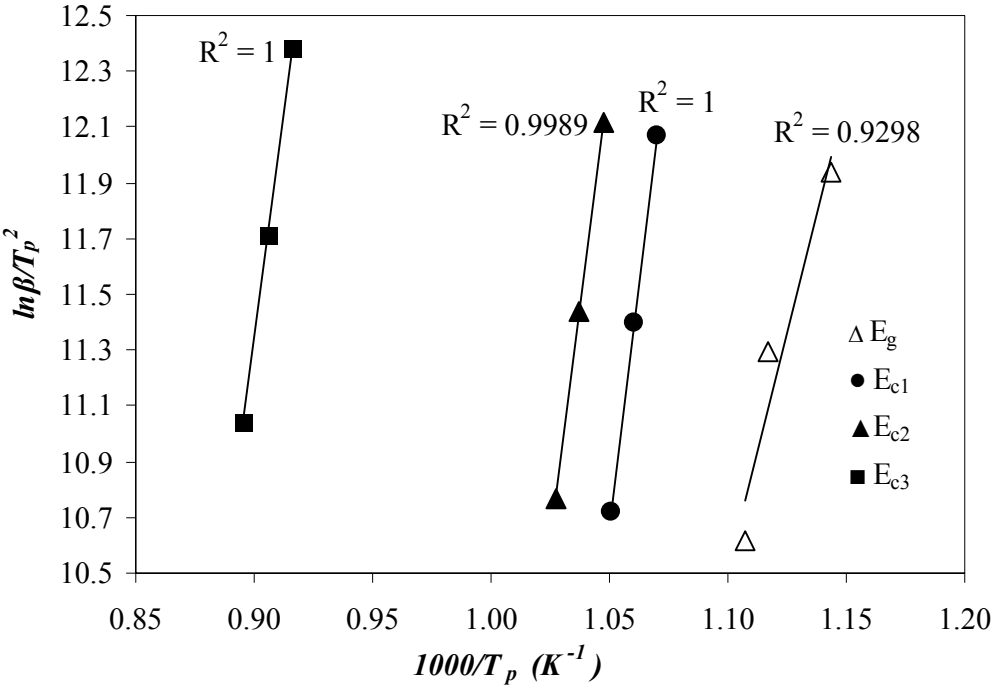

Figure 4.34 Kissinger plots for the glass transition and three exothermic reactions by using DSC data of 5, 10, and 20 °C/min.

Table 4.6 Activation energies estimated by using Kissinger method

Transition	**Activation Energy (kJ/mol)**
Glass transition	282.17
First exothermic transition	588.76
Second exothermic transition	571.49
Third exothermic transition	530.75

When the activation energies of exothermic transitions are compared, it can be seen that the activation energy of the first is higher than the others which is the one that most matters the stability of the amorphous alloy. The decrease in the activation energy as the crystallization proceeds may indicate that the crystallization of second and third phases is easier than the first one.

As a further attempt to study the non-isothermal crystallization kinetics and confirm the results of the Kissinger method, the Ozawa method [76] used to estimate the activation energies Equation (2.21). This time $ln\beta$ versus $1/T_p$ yields a straight line with a slope of with a slope of $-1.0516E_c/R$. The deviation from the straight line was seen at high scanning rates similar to the case for the Kissinger plots. The correlation coefficients were observed to be very low except for the fit for the second peak temperature which had a high correlation since it could not be observed at high heating rates. Therefore, high scanning rate data, DSC data of 40 and 99 °C/min, was excluded further and Figure 4.35 was obtained finally showing the highest correlation coefficient.

The activation energies calculated using the Ozawa method can be seen in Table 4.10. When the two tables, Table 4.6 and 4.7 are compared, it can be seen that the activation energies estimated by two methods were very close to each other especially the glass transition activation energy, which is almost the same. The activation energy of second crystallization reaction, however, was higher than it was estimated by the Kissinger method. The first crystallization activation energy was found to be reasonable for both methods as compared to the value of 559.9 kJ/mol found in the literature for a similar alloy [110].

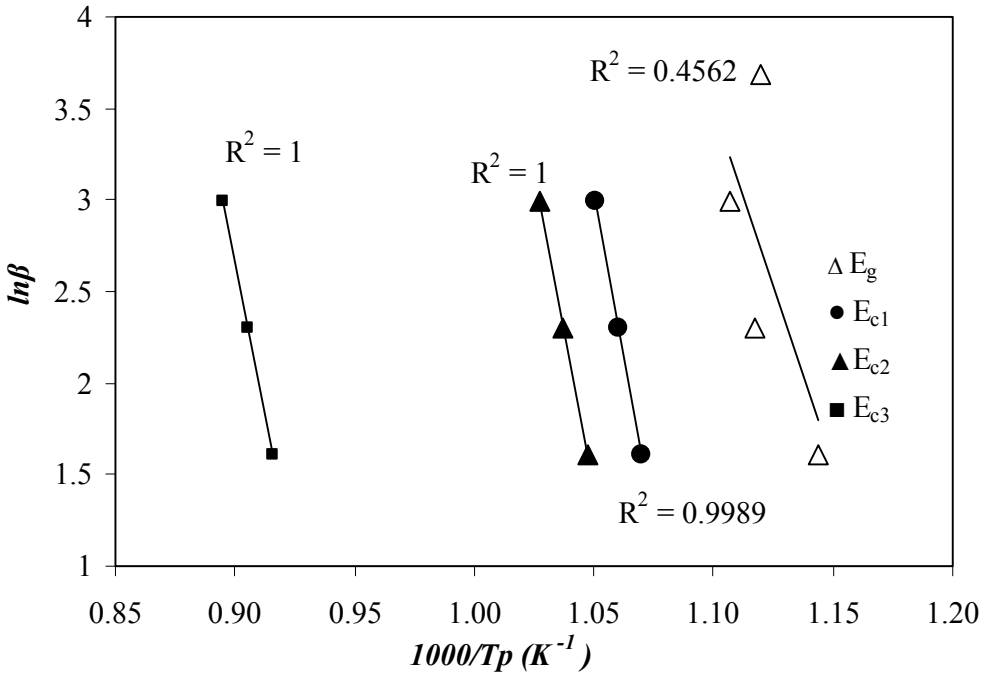

Figure 4.35 Ozawa plots of *ln β* as a function of *1000/T* for glass transition and exothermic transitions excluding the DSC data of 40 and 99 °C/min.

Table 4.7 Activation energies estimated by using Ozawa method

Transition	**Activation Energy (kJ/mol)**
Glass transition	282.90
First exothermic transition	580.50
Second exothermic transition	559.25
Third exothermic transition	522.80

4.8 MAGNETIC PROPERTIES OF THE ALLOY

The magnetic properties of the alloy were investigated using the vibrating samples magnetometer (VSM). The results of the VSM analysis are presented in Figure 4.36 showing the hysteresis loops of the master alloy ingot, amorphous sample and the sample annealed at 750 ºC. The saturation magnetization (M_s) of the annealed

sample was observed to be greater than those of the master alloy and amorphous sample. The magnetic energy loss of the annealed sample was also higher than the other samples but all samples can be said to have soft magnetic properties.

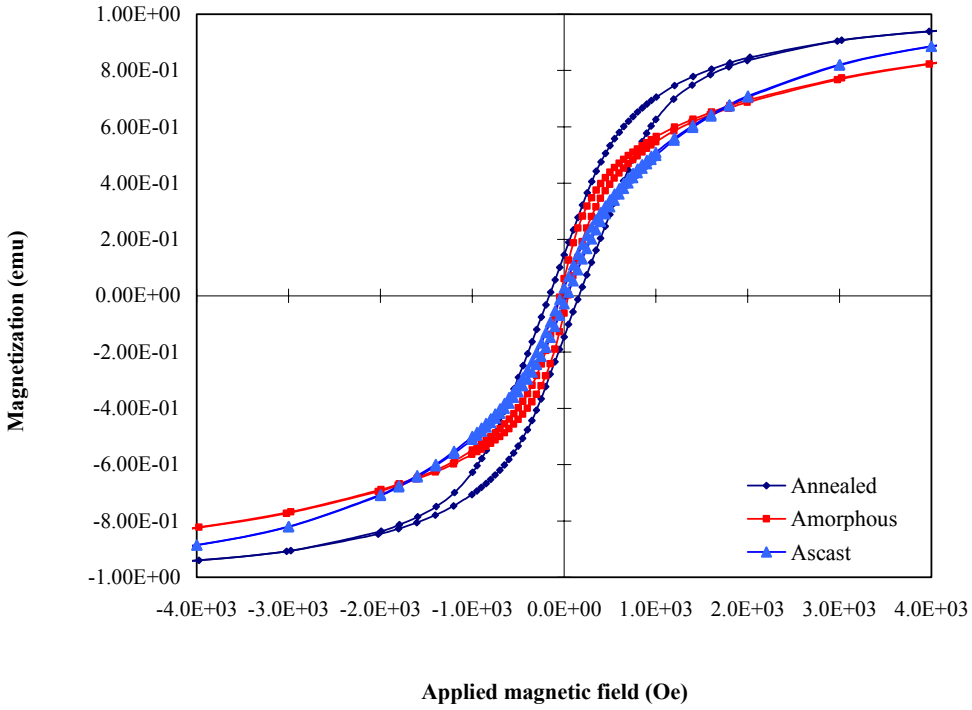

Figure 4.36 Hysteresis loops of the as-cast, annealed and amorphous samples

CHAPTER 5

CONCLUSIONS

In this study the solidification and crystallization behaviour of bulk glass forming $Fe_{60}Co_8Mo_5Zr_{10}W_2B_{15}$ alloy was studied. Equilibrium and non-equilibrium cooling conditions were applied to study the solidification behaviour. The solidification of the alloy was found to occur in a sequence of eutectic and peritectic reactions. As the partially or essentially amorphous samples did not contain any trace of eutectic structure, it was confirmed that the suppression of the eutectic reaction stimulated the formation of the amorphous phase. The eutectic reaction was found to show an interesting behaviour in DSC heating and cooling experiments. The first heating scans revealed almost indiscernible eutectic peaks, whereas the eutectic reaction became more prominent in all second heating scans. In addition, the peritectic reaction following the eutectic, was found to be overlapped with the peak of the melting event. The two peaks were observed to separate from each other in the second heating scans. Such behaviour was considered to be developed because of the reactions that could not go to completion in the first heating scans due to the formation of some metastable phases.

Two methods were used for the formation of the bulk metallic glass: quenching the alloy from the liquid state and from the semi-solid state. The amorphous phase formation by applying rapid cooling from the liquid state was investigated by using different starting materials and preparation methods. The amorphous sample prepared by using pure constituents and arc melting method was found to have better glass forming ability than the ones produced by using FeB master alloy and the

induction heating method. The glass forming ability parameters, such as T_{rg}, ΔT_x, and γ were estimated for the amorphous samples. All of them except for the T_{rg} showed that the alloy is a good bulk glass former, however each parameter revealed different trends for the bulk glass forming abilities of the samples having different thermal histories.

Quenching of the alloy from the semi-solid state was applied as a new technique for the production of amorphous phase. The semi-solid state was found exist in between the eutectic and peritectic reactions. The alloy was quenched from 1000 ºC, which is in the semi-solid region. It was observed to contain partially amorphous structure having an amorphous phase fraction of % 68.54 embedded with certain crystalline phases was obtained by this method.

The critical cooling rate of the alloy was estimated to be 5.35 K/s, which was considered to be a reasonable value in terms of the glass forming ability of the alloy, which was indeed related to the critical cooling rate. The critical cooling rate for eutectic solidification, on the other hand, was calculated as 0.14 K/s, indicating that the alloy melts could be solidified into the amorphous phase by applying low cooling rates. The estimation procedure was found to be effective as the results were in good agreement with the results of previous studies.

The crystallization kinetics of the alloy was studied isothermally at temperatures chosen in the supercooled liquid state and above the first crystallization temperature. The sample, which was heated isothermally in the furnace at a temperature in the supercooled liquid state, showed almost no evidence of the crystalline phase. The α-Fe crystallites with a size of 0.05 nm was distinguished in the XRD pattern. However, the sample heated to a temperature above the first crystallization temperature revealed the presence of larger α-Fe crystallites with a size of 130.28 nm, which were observable by using the SEM: The isothermal experiments were repeated in DSC applying exactly the same heating procedure. There were no crystallization signals detected in the isothermal section of the DSC scans during 5

hour period of time. The heat flow change during the first 1000 seconds of the isothermal scans was attributed to an enthalpic relaxation that might have occurred upon heating. The activation energies of glass transition and crystallization events were estimated by the Kissinger and Ozawa methods. Both methods lead to similar results. The activation energy of the first crystallization peak was found to be larger than the others and this result is in good agreement with the results reported in the literature.

The magnetic properties of the master alloy ingot, amorphous sample and the sample annealed at 750 ºC were compared by using the VSM results. It was observed that the annealed sample had the highest saturation magnetization and the magnetic energy loss in comparison with the other two specimens

REFERENCES

1. Z.-Z. Yuan, X.-D. Chen, B.-X. Wang and Y.-J. Wang, *Kinetics study on non-isothermal crystallization of the metallic $Co_{43}Fe_{20}Ta_{5.5}B_{31.5}$ glass*, Journal of Alloys and Compounds, 407 (2006), pp. 163-169.
2. M. X. Xia, C. L. Ma, H. X. Zheng and J. G. Li, *Preparation and crystallization of $Ti_{53}Cu_{27}Ni_{12}Zr_3Al_7Si_3B_1$ bulk metallic glass with wide supercooled liquid region*, Materials Science and Engineering A 390 (2005), pp. 372-375.
3. F.E. Luborsky 1983. Amorphous Metallic Alloys. Pages 1-7 in F.E. Luborsky, ed., *Amorphous Metallic Alloys*, Butterworths, London, 1983.
4. T. Egami, K. Maeda, and V. Vitek, *Structural defects in amorphous solids a computer simulation study,* Philosophical Magazine A, 41 (1981), pp. 883-891.
5. H. S. Chen, K. T. Aust and Y. Waseda, *Structural investigation of amorphous Fe-Zr, Co-Zr and Ni-Zr alloys with low zirconium concentration*, Journal of Non-Crystalline Solids, 46 (1981), pp. 307-319.
6. M. V. Akdeniz, A. O. Mekhrabov and M. K. Pehlivanoğlu, *Solidification behaviour of bulk glass-forming alloy systems*, Journal of Alloys and Compounds, 386 (2005), pp.185-191.
7. Pehlivanoğlu, M. K. 2003. Production and Development of Bulk Metallic Glasses, Ankara , Ph.D. Thesis, Middle East Technical University, 175 p.
8. J. Kramer, *Der amorphe Zustand der Metalle,* Zeitschrift fur Physik 106 (1937), pp.675-691.
9. A. Brenner, D. E. Couch, and E. K. Williams, *Electrodeposition of alloys of phosphorus with nickel or cobalt,* Journal of Research of the National Bureau of Standards, 44 (1950), pp.109-122.
10. W. Klement, R. H. Willens and P. Duwez, *Non-crystalline Structure in Solidified Gold-Silicon Alloys*, Nature, 187 (1960), pp. 869-870.

11. T.R. Anantharaman 1984. Metallic Glasses: An Overview. Pages 1-29 in T. Anantharaman, ed., *Metallic Glasses: Production, properties and applications*, Trans Tech Publications, Switzerland, 1984.
12. W. H. Wang, C. Dong and C. H. Shek, *Bulk metallic glasses*, Material Science and Engineering R, 44 (2004), pp. 45-89.
13. D. Turnbull, *The Liquid State and the Liquid-Solid Transition*, The Institute of Metals Division Lecture, Transactions of the Metallurgical Society of AIME. 221 (1961), pp. 422-439.
14. H.S. Chen, D. Turnbull, *Evidence of a Glass-Liquid Transition in a Gold-Germanium-Silicon Alloy*, Journal of Chemical Physics 48 (1968), pp. 2560-2571.
15. H.S. Chen, D. Turnbull, *Formation, Stability and Structure of Palladium-Silicon Based Alloy Glasses*, Acta Metallurgica 17 (1969), pp.1021-1031.
16. D. Turnbull, J.C. Fisher, *Rate of Nucleation in Condensed Systems*, Journal of Chemical Physics, 17 (1949), pp.7 1-73.
17. W.L. Johnson, *Bulk glass-forming metallic alloys: Science and technology,* Materials Research Society Bulletin 24 (1999), pp. 42-56.
18. H. S. Chen, *Thermodynamic considerations on the formation and stability of metallic glasses*, Acta Metallurgica, 22 (1974), pp. 1505-1511.
19. H. W. Kui, A. L. Greer and D. Turnbull, *Formation of Bulk Metallic Glass by Fluxing*, Applied Physics Letters, 45 (1984), pp.615-616.
20. A. Inoue, T. Zhang, T. Masumoto, *Al–La–Ni amorphous alloys with a wide supercooled liquid region*, Materials Transactions, JIM 30 (1989), pp.965–972.
21. A. Inoue, A. Kato, T. Zhang, S.G. Kim, T. Masumoto, *Mg–Cu–Y amorphous alloys with high mechanical strengths produced by a metallic mould casting method*, Materials Transactions JIM 32 (1991), pp.609–616.
22. T. Zhang, A. Inoue, T. Masumoto, *Amorphous Zr–Al–Tm (Tm=Co, Ni, Cu) alloys with significant supercooled liquid region of over 100 K*, Materials Transactions JIM 32 (1991), pp.1005–1010.
23. J. F Löffler, *Bulk metallic glasses*, Intermetallics 11 (2003), pp.529-540.

24. A. Peker, W. L. Johnson, *A highly processable metallic glass–* $Zr_{41.2}Ti_{13.8}Cu_{12.5}Ni_{10.0}Be_{22.5}$, Applied Physics Letters 63 (1993), pp.2342–2244.
25. A. Inoue and A. Takeuchi, *Recent progress in bulk glassy, nanoquasicrystalline and nanocrystalline alloys*, Materials Science and Engineering A, 375-377 (2004), pp. 16-30.
26. A. Inoue, N. Nishiyama, H. Kimura, *Preparation and thermal stability of bulk amorphous* $Pd_{40}Cu_{30}Ni_{10}P_{20}$ *alloy cylinder of 72 mm in diameter,* Materials Transactions JIM 38 (1997), pp.179–183.
27. M.L. Hair, A.M. Filbert in Encyclopedia of Material Science and Engineering Ed. By M. B. Bever, Vol.3, Pergamon Press, Oxford, UK, 1988.
28. J. C. Dyre, *Colloquium: The glass transition and elastic models of glass forming liquids*, Reviews of Modern Physics, 78 (2006), pp. 953-972.
29. D. V. Louzguine-Luzgin and A. Inoue, *A glance on the glass-transition phenomenon from the viewpoint of devitrification*, Journal of Alloys and Compounds, 434-435 (2007), pp. 121-125.
30. D. Turnbull, *Under What Conditions Can a Glass be Formed?*, Contemporary Physics 10 (1969), pp.473-488.
31. H.W. Kui, D. Turnbull, *The Melting of* $Ni_{40}Pd_{40}P_{20}$ *Glass,* Applied Physics Letters 47 (1985), pp.796-797.
32. A.L. Greer, *Metallic Glasses*, Science 267 (1995), pp.1947-1953.
33. T. Egami, *Glass transition and viscosity in metallic glasses and liquids*, Journal of Alloys and Compounds, 434-435 (2007), pp. 110-114.
34. W. H. Wang, C. Dong and C. H. Shek, *Bulk metallic glasses*, Material Science and Engineering R, 44 (2004), pp. 45-89.
35. A. Inoue, *High strength bulk amorphous alloys with low critical cooling rates (overview)*, Materials Transactions, JIM, 36 (1995), pp. 866-875.
36. A. Inoue, *Bulk Amorphous Alloys : Preparation and Fundamental characteristics*, Trans. Tech. Public. Ltd., Switzerland, 1998.
37. H. J. Fecht, W. L. Johnson, *Thermodynamics and metastability of bulk metallic glasses*, Material Science and Engineering A 2-8 (2004), pp.375-377.

38. W. Kauzmann, *The nature of the glassy state and the behavior of liquids at low temperatures*, Chemical Reviews, 43 (1948), pp.219-256.
39. C. A. Angell, *Formation of glasses from liquids and biopolymers*, Science, 267 (1995), pp.1924-1935.
40. J. F. Löffler, *Bulk metallic glasses*, Intermetallics, 11 (2003), pp. 529-540.
41. M. L. F. Nascimento, L. A. Souza, E. B. Ferreira and E. D. Zanotto, *Can glass stability parameters infer glass forming ability?*, Journal of Non-Crystalline Solids, 351 (2005), pp. 3296-3308.
42. Z. P. Lu, H. Bei and C. T. Liu, *Recent progress in quantifying glass-forming ability of bulk metallic glasses*, Intermetallics, 15 (2007), pp. 618-624.
43. T. Egami and Y. Waseda, *Atomic size effect on the formability of metallic glasses*, Journal of Non-Crystalline Solids, 64 (1984), pp. 113-134.
44. T. Egami, *The atomic structure of aluminum based metallic glasses and universal criterion for glass formation*, Journal of Non-Crystalline Solids, Ninth International Conference on Liquid and Amorphous Metals, 205-207 (1996), pp. 575-582.
45. T. Egami, *Universal criterion for metallic glass formation*, Materials Science and Engineering A, Ninth International Conference on Rapidly Quenched and Metastable Materials, 226-228 (1997), pp. 261-267.
46. O. N. Senkov and D. B. Miracle, *Effect of the atomic size distribution on glass forming ability of amorphous metallic alloys*, Materials Research Bulletin, 36 (2001), pp. 2183-2198.
47. O. N. Senkov and D. B. Miracle, *A topological model for metallic glass formation*, Journal of Non-Crystalline Solids, 317 (2003), pp. 34-39.
48. G. Shao, *Thermodynamic and kinetic aspects of intermetallic amorphous alloys*, Intermetallics, 11 (2003), pp. 313-324.
49. A. Inoue, T. Zhang and T. Masumoto, *Glass-forming ability of alloys*, Journal of Non-Crystalline Solids, 156-158 (1993), pp. 473-480.
50. G. J. Fan, H. Choo and P. K. Liaw, *A new criterion for the glass-forming ability of liquids*, Journal of Non-Crystalline Solids, 353 (2007), pp. 102-107.

51. I. W. Donald and H. A. Davies, *Prediction of glass-forming ability for metallic systems*, Journal of Non-Crystalline Solids, 30 (1978), pp. 77-85.
52. A. Hruby, *Evaluation of glass-forming tendency by means of DTA*, Czechoslovak Journal of Physics, 22 (1972), pp. 1187-1193.
53. M. Saad, M. Poulain, Glass Formation Ability Criterion, Material Science Forum, 19-20 (1987), pp.11-18.
54. Z. P. Lu and C. T. Liu, *A new glass-forming ability criterion for bulk metallic glasses*, Acta Materialia, 50 (2002), pp. 3501-3512.
55. Z. P. Lu and C. T. Liu, *A new approach to understanding and measuring glass formation in bulk amorphous materials*, Intermetallics 12 (2004), pp. 1035-1043.
56. Q. Chen, J. Shen, D. Zhang, H. Fan, J. Sun and D. G. McCartney, *A new criterion for evaluating the glass-forming ability of bulk metallic glasses*, Materials Science and Engineering: A, 433 (2006), pp. 155-160.
57. K. Mondal and B. S. Murty, *On the parameters to assess the glass forming ability of liquids*, Journal of Non-Crystalline Solids, 351 (2005), pp. 1366-1371.
58. R. J. Highmore and A. L. Greer, *Eutectics and the formation of amorphous alloys*, Nature, 339 (1989), pp. 363-365.
59. D. Ma, H. Cao and Y. A. Chang, *Identifying bulk metallic glass-formers from multi-component eutectics*, Intermetallics, 15 (2007), pp. 1122-1126.
60. A. Inoue, *Stabilization of metallic supercooled liquid and bulk amorphous alloys*, Acta Materialia, 48 (2000), pp. 279-306.
61. J. Basu and S. Ranganathan, *Bulk metallic glasses:A new class of engineering materials*, Sadhana, 28 (2003), pp. 783-798.
62. A. Inoue, T. Zhang, N. Nishiyama, K. Ohba and T. Masumoto, *Preparation of 16 mm diameter rod of amorphous $Zr_{65}Al_{7.5}Ni_{10}Cu_{17.5}$ alloy*, Materials Transactions, JIM, 34 (1993), pp. 1234-1237.
63. A. Inoue, T. Nakamura, N. Nishiyama and T. Masumoto, *Mg-Cu-Y bulk amorphous alloys with high tensile strength produced by a high-pressure die casting method*, Materials Transactions, JIM, 33 (1992), pp. 937-945.
64. A. Inoue, T. Nakamura, T. Sugita, T. Zhang and T. Masumoto, *Bulky La-Al-TM (TM = transition metal) amorphous alloys with high tensile strength produced*

by a high-pressure die casting method, Materials Transactions, JIM, 34 (1993), pp. 351-358.

65. K. Ikarashi, T. Mizushima, A. Makino and A. Inoue, *Preparation of the bulk Fe-Al-Ga-P-C-B-Si glassy alloys in a ringed form by copper mold casting*, Materials Science and Engineering A, 304-306 (2001), pp. 763-766.
66. B. Majumdar and D. Akhtar, *Synthesis and crystallisation of Fe-Co-Ni-Zr(Nb)-B bulk glasses.*, Materials Science and Technology, 21 (2005), pp. 1139-1144.
67. S. Kavesh 1986. Principles of Fabrication. Pages 36-71 in ASM Materials Science Seminar and American Society for Metals., *Metallic glasses.* American Society for Metals, Metals Park, Ohio, 1978.
68. M. G. Scott 1983. Crystallization. Pages 144-168 in F. E. Luborsky, ed., *Amorphous Metallic Alloys*, Butterworths, London, 1983.
69. I. Gallino, M. B. Shah and R. Busch, *Enthalpy relaxation and its relation to the thermodynamics and crystallization of the Zr58.5Cu15.6Ni12.8Al10.3Nb2.8 bulk metallic glass-forming alloy*, Acta Materialia, 55 (2007), pp. 1367-1376.
70. D.R. Uhlmann and R. W.Hopper 1986. Relaxation in Glasses. Pages 128-160 in ASM Materials Science Seminar and American Society for Metals., *Metallic glasses : papers presented at a seminar of the Materials Science Division of the American Society for Metals, September 18 and 19, 1976.*, American Society for Metals, Metals Park, Ohio, 1978.
71. R. Surana, A. Pyne, M. Rani and R. Suryanarayana, *Measurement of enthalpic relaxation by differential scanning calorimetry--effect of experimental conditions*, Thermochimica Acta, 433 (2005), pp. 173-182.
72. A.N. Kolmogorov, *A statistical theory for the recrystallization of metals,* Izvestia Akademia Nauk Serie Mathematica SSSR,1 (1937), pp. 355-359.W.A. Johnson and R.F. Mehl, *Reaction kinetics in processes of nucleation and growth,* Transactions of American Institute of Mining, Metallurgical and Petroleum Engineers, 135 (1939), pp.416-458.
74. M. Avrami*, Kinetics of Phase Change I*, Journal of Chemical Physics. 7 (1939), pp. 1103-1112

75. H.E. Kissinger, *Reaction Kinetics in Differential Thermal Analysis*, Analytical Chemistry , 29 (1957) , pp.1702-1706.
76. T. Ozawa, *A new method of analyzing thermogravimetric data,* Bulletin Chemical Society of Japan, 38 (1965),pp.1881-1886.
77. M. Castro, F. Dominguez-Adame, A. Sanchez and T. Rodriguez, *Model for crystallization kinetics: Deviations from Kolmogorov--Johnson--Mehl--Avrami kinetics*, Applied Physics Letters, 75 (1999), pp. 2205-2207.
78. Y. S. Ji, S. J. Chung, M.-R. Ok, K. T. Hong, J.-Y. Suh, J. W. Byeon, J.-K. Yoon, K. H. Lee and K. S. Lee, *Analysis on the phase transition behavior of Cu base bulk metallic glass by electrical resistivity measurement*, Materials Science and Engineering: A, 449-451 (2007), pp. 521-525.
79. S. J. Chung, K. T. Hong, M.-R. Ok, J.-K. Yoon, G.-H. Kim, Y. S. Ji, B. S. Seong and K. S. Lee, *Analysis of the crystallization of $Zr_{41}Ti_{14}Cu_{12.5}Ni_{10}Be_{22.5}$ bulk metallic glass using electrical resistivity measurement*, Scripta Materialia, 53 (2005), pp. 223-228.
80. B. Gun, K. J. Laws and M. Ferry, *Static and dynamic crystallization in Mg-Cu-Y bulk metallic glass*, Journal of Non-Crystalline Solids, 352 (2006), pp. 3887-3895.
81. L. Gao, J. Shen, J.F. Sun, G. Wang, D.W. Xing, H.Z. Xian and B.D. Zhou, *Crystallization behavior of ZrAlNiCu bulk metallic glass with wide supercooled liquid region*, Materials Letters, 57 (2003), pp. 1894-1898.
82. Y. J. Yang, D. W. Xing, J. Shen, J. F. Sun, S. D. Wei, H. J. He and D. G. McCartney, *Crystallization kinetics of a bulk amorphous Cu-Ti-Zr-Ni alloy investigated by differential scanning calorimetry*, Journal of Alloys and Compounds, 415 (2006), pp. 106-110.
83. K. Biswas, S. Ram, L. Schultz and J. Eckert, *Crystallization kinetics of amorphous $Fe_{67}Co_{9.5}Nd_3Dy_{0.5}B_{20,}$* Journal of Alloys and Compounds, 397 (2005), pp. 104-109.
84. L. Liu, Z. F. Wu and J. Zhang, *Crystallization kinetics of $Zr_{55}Cu_{30}Al_{10}Ni_5$ bulk amorphous alloy*, Journal of Alloys and Compounds, 339 (2002), pp. 90-95.

85. X.-d. Wang, H. Lee and S. Yi, *Crystallization behavior of preannealed bulk amorphous alloy $Zr_{62}Al_8Ni_{13}Cu_{17}$*, Materials Letters, 60 (2006), pp. 935-938.
86. A. Takeuchi and A. Inoue, *Quantitative evaluation of critical cooling rate for metallic glasses*, Materials Science and Engineering A, 304-306 (2001), pp. 446-451.
87. C. S. Ray, S. T. Reis, R. K. Brow, W. Holand and V. Rheinberger, *A new DTA method for measuring critical cooling rate for glass formation*, Journal of Non-Crystalline Solids, 351 (2005), pp. 1350-1358.
88. D. R. Uhlmann, *A kinetic treatment of glass formation*, Journal of Non-Crystalline Solids, 7 (1972), pp. 337-348.
89. J. M. Barandiaran and J. Colmenero, *Continuous cooling approximation for the formation of a glass*, Journal of Non-Crystalline Solids, 46 (1981), pp. 277-287.
90. M. L. F. Nascimento, L. A. Souza, E. B. Ferreira and E. D. Zanotto, *Can glass stability parameters infer glass forming ability?*, Journal of Non-Crystalline Solids, 351 (2005), pp. 3296-3308.
91. C. Suryanarayana and C. C. Koch, *Nanocrystalline materials: Current research and future directions*, Hyperfine Interactions, 130 (2000), pp. 5-44.
92. K.Lu, *Nanocrystalline metals crystallized from amorphous solids: nanocrystallization, structure, and properties*, Materials Science and Engineering: R: Reports, 16 (1996), pp. 161-221.
93. J. Eckert in C. C. Koch (eds), *Nanostructured Materials Processing, Properties and Applications*, Noyes Publications William Andrew Publishing, New York, U.S.A., 2002, p.423.
94. B. Cantor, *Nanocrystalline materials manufactured by advanced solidification processing methods*, Materials Science Forum, 307 (1999), pp. 143-152.
95. A. L. Greer, *Nanostructured materials -From fundamentals to applications*, Materials Science Forum, 269-272 (1998), pp. 3-10.
96. T. Kulik, *Nanocrystallization of metallic glasses*, Journal of Non-Crystalline Solids, 287 (2001), pp. 145-161.

97. K. F. Kelton, T. K. Croat, A. K. Gangopadhyay, L.-Q. Xing, A. L. Greer, M. Weyland, X. Li and K. Rajan, *Mechanisms for nanocrystal formation in metallic glasses*, Journal of Non-Crystalline Solids, 317 (2003), pp. 71-77.

98. A. Inoue, *Preparation and novel properties of nanocrystalline and nanoquasicrystalline alloys*, Nanostructured Materials, 6 (1995), pp. 53-64.

99. K. Lu, W. D. Wei and J. T. Wang, *Microhardness and fracture properties of nanocrystalline Ni-P alloy*, Scripta Metallurgica et Materialia, 24 (1990), pp. 2319-2323.

100. M. L. Sui, L. Y. Xiong, W. Deng, K. Lu, S. Patu and Y. Z. He, *Investigation of the interfacial defects in a nanocrystalline Ni-P alloy by positron annihilation spectroscopy*, Journal of Applied Physics, 69 (1991), pp. 4451-4453.

101. J. Eckert 2002. Structure Formation and Mechanical Behavior of Two-Phase Nanostructured Materials. Pages 423-525 in C.C. *Koch ed. Nanostructured Materials Processing, Properties and Potential Applications*, Noyes Pub., Norwich, NY, 2007.

102. M. F. Ashby and A. L. Greer, *Metallic glasses as structural materials*, Scripta Materialia 54 (2006), pp. 321-326.

103. A. Inoue, *Bulk amorphous and nanocrystalline alloys with high functional properties*, Materials Science and Engineering A, 304-306 (2001), pp. 1-10.

104. A. Baiker, *Metallic glasses in heterogeneous catalysis*, Faraday Discussions of the Chemical Society, 87 (1989), pp.239-251.

105. A. Castellero, M. Motyka, A. L. Greer, and M. Baricco, *Synthesis and crystallisation of $Fe_{61}Co_7Zr_{10}Mo_5W_2B_{15}$ bulk metallic glasses.* Materials Science and Engineering A, 375-377 **(**2004) pp. 250-254.

106. F.Stein, G. Sauthoff, and M. Palm, *Experimental Determination of Intermetallic Phases, Phase Equilibria, and Invariant Reaction Temperatures in the Fe-Zr System,* Journal of Phase Equilibria and Diffusion, 23 (2002), pp. 480-494.

107. X.Y. Xiong, T. R. Finlayson, and B.C. Muddle, *The effect of boron content on the crystallization behaviour and microstructure for nanocrystalline $Fe_{93-x}Zr_7B_x$ Alloy*s, Materials Physics and Mechanics, 4 (2001), pp.34-38.

108. T. A. Waniuk , J. Schroers, and W L: Johnson, *Critical cooling rate and thermal stability of Zr-Ti-Cu-Ni-Be alloys vs. composition*, Applied Physics Letters, 78 (2001), pp. 1213-1215

109. G. W. Smith, F. E. Pinkerton and J. J. Moleski, *Determination of phase stability in a bulk amorphous alloy by differential scanning calorimetry*, Thermochimica Acta, 342 (1999), pp. 31-39.

110. D.Y. Liu, W.S. Sun, A.M. Wang, H.F Zhang, and Z.Q. Hu, P*reparation, thermal stability, and magnetic properties of Fe-Co-Zr-Mo-W-B bulk metallic glass,* Journal of Alloys and Compounds, 370 (2004), pp. 249-253.

111. Y. Hu, L. Liu, K.C. Chan, M. Pan, and W. Wang, *The effect of crystallization on the microstructure and magnetic properties of* $Fe_{61}Co_7Zr_{9.5}W_2B_{15}$ *bulk metallic glass*, Materials Letters, 60 (2006), pp.1080-1084.

112. P. Pawlik and H.A. Davies, *The bulk glass forming abilities and mechanical and magnetic properties of Fe-Co-Zr-Mo-W-B alloys*, Journal of Non-Crystalline Solids, 329 (2003), pp. 17-21.

APPENDIX A

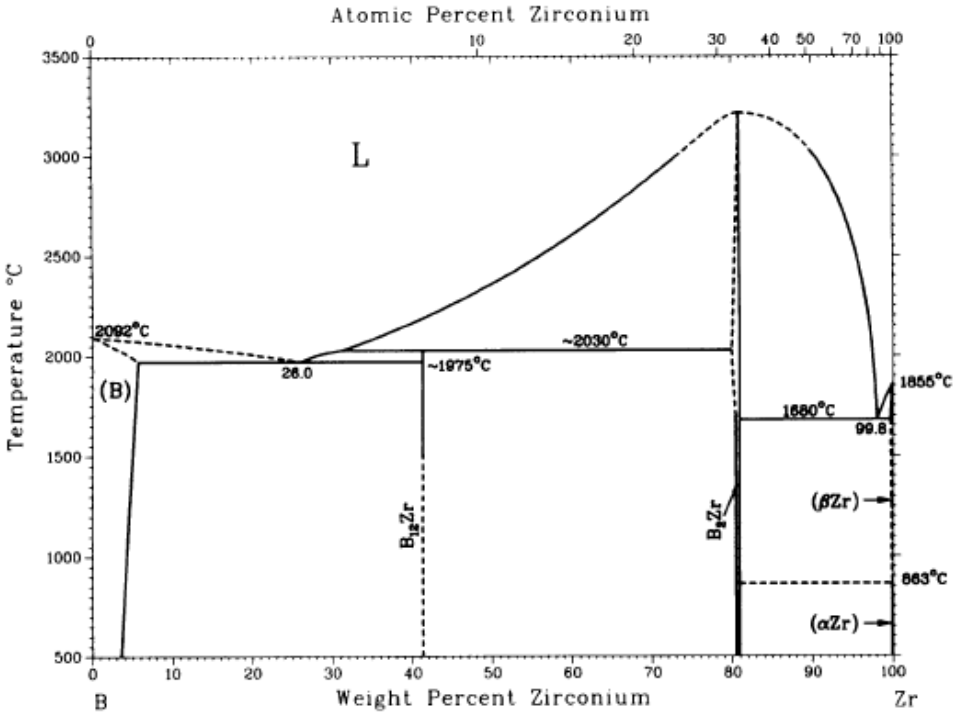

Figure A.1 Binary phase diagram of B-Zr.

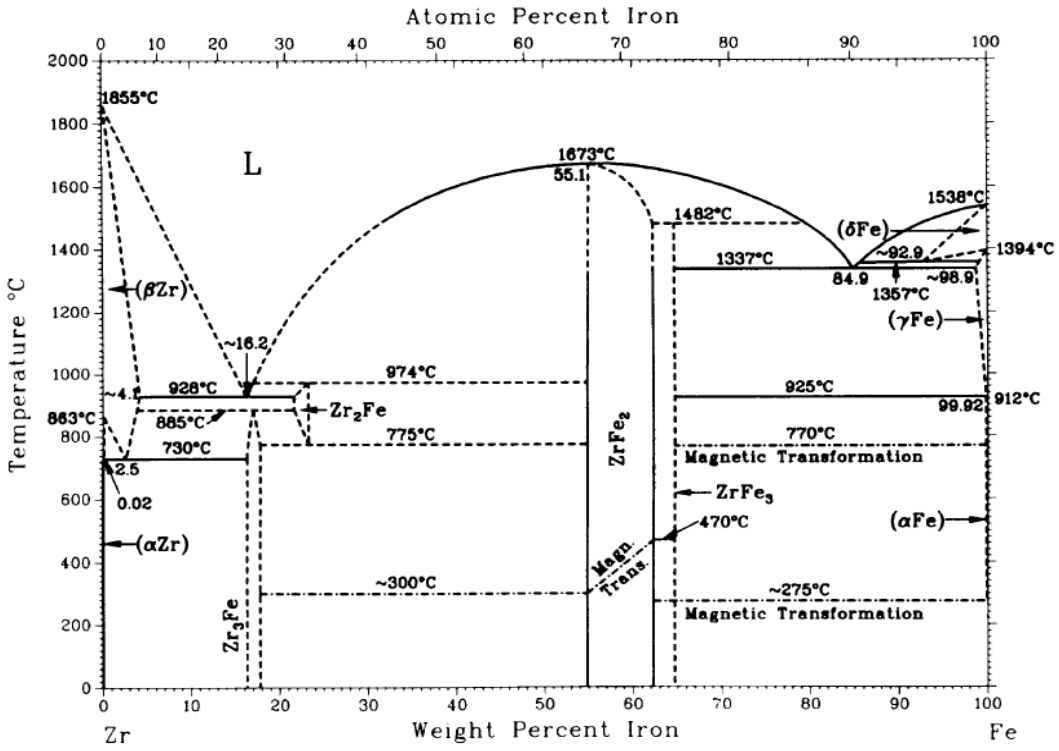

Figure A.2 Binary phase diagram of Fe-Zr.